ALMA MATER STUDIORUM · UNIVERSITÀ DI BOLOGNA

Scuola di Scienze
Dipartimento di Fisica e Astronomia
Corso di Laurea Magistrale in Fisica

Applications of advanced and dual energy computed tomography in proton therapy

Relatore:
Prof.ssa Maria Pia Morigi

Correlatori:
Dott.ssa Marta Peroni
Dott.ssa Alessandra Bolsi

Presentata da:
Silvia Belloni

Anno Accademico 2015/2016

To my family and Luca,
for being there, always.

Abstract

This thesis focuses on advanced reconstruction methods and Dual Energy (DE) Computed Tomography (CT) applications for proton therapy, aiming at improving patient positioning and investigating approaches to deal with metal artifacts.

To tackle the first goal, an algorithm for post-processing input DE images has been developed. The outputs are tumor- and bone-canceled images, which help in recognising structures in patient body. We proved that positioning error is substantially reduced using contrast enhanced images, thus suggesting the potential of such application.

If positioning plays a key role in the delivery, even more important is the quality of planning CT. For that, modern CT scanners offer possibility to tackle challenging cases, like treatment of tumors close to metal implants. Possible approaches for dealing with artifacts introduced by such rods have been investigated experimentally at Paul Scherrer Institut (Switzerland), simulating several treatment plans on an anthropomorphic phantom. In particular, we examined the cases in which none, manual or Iterative Metal Artifact Reduction (iMAR) algorithm were used to correct the artifacts, using both Filtered Back Projection and Sinogram Affirmed Iterative Reconstruction as image reconstruction techniques. Moreover, direct stopping power calculation from DE images with iMAR has also been considered as alternative approach. Delivered dose measured with Gafchromic EBT3 films was compared with the one calculated in Treatment Planning System. Residual positioning errors, daily machine dependent uncertainties and film quenching have been taken into account in the analyses. Although plans with multiple fields seemed more robust than single field, results showed in general better agreement between prescribed and delivered dose when using iMAR, especially if combined with DE approach. Thus, we proved the potential of these advanced algorithms in improving dosimetry for plans in presence of metal implants.

Keywords: Dual Energy Computed Tomography, patient positioning, metal artifacts, proton therapy, dose distribution, phantom

Sommario

Questo progetto di tesi, svolto presso il Paul Scherrer Institut (Svizzera), è focalizzato su applicazioni di metodi avanzati di ricostruzione e Dual Energy (DE) Computed Tomography (CT) in terapia protonica. I due scopi principali sono il miglioramento del posizionamento del paziente e l'analisi di moderni approcci atti ad affrontare difficoltà introdotte in presenza di artefatti metallici nelle immagini tomografiche.

Per il conseguimento del primo obiettivo, è stato sviluppato un algoritmo di post-processing di immagini DE. In uscita sono prodotte due immagini a contrasto enfatizzato, ove tumore e tessuto osseo sono rispettivamente rimossi, facilitando quindi il riconoscimento di varie strutture interne al corpo del paziente. É stato dimostrato che sfruttando tali immagini, anziché quelle mono-energetiche correntemente usate, l'errore commesso nel posizionamento è sostanzialmente ridotto, confermando così le potenzialità di tale strumento.

Se il posizionamento gioca un ruolo chiave ai fini del rilascio della corretta dose al paziente, ancor più importante é la qualità della CT di pianificazione del trattamento. Moderni CT scanner sono stati sviluppati in tale direzione, così da poter trattare casi complessi, come ad esempio tumori in prossimità di impianti metallici. Il secondo scopo di questa tesi mira proprio all'analisi di possibili approcci per fronteggiare gli artefatti introdotti da tali innesti. Lo studio sperimentale è stato condotto simulando diversi piani di trattamento su un fantoccio antropomorfo. In particolare, sono stati considerati la non correzione dell'artefatto, la correzione manuale e l'algoritmo Iterative Metal Artifact Reduction (iMAR), usando come tecniche di ricostruzione dell'immagine sia Filtered Back Projection che Sinogram Affirmed Iterative Reconstruction. Come ulteriore metodo è stato valutato l'approccio basato su DECT, in combinazione ad iMAR, per il calcolo diretto del *proton stopping power*. La dose rilasciata è stata misurata con pellicole radiocromiche (Gafchromic film EBT3), quindi successivamente confrontata con quella calcolata usando il Treatment Planning System. Errori residui di posizionamento, incertezze legate alla macchina durante il rilascio della dose ed effetto di quenching dei film sono stati inseriti nel processo di analisi. Sebbene piani a fasci multipli si siano rivelati più robusti rispetto al fascio singolo, i risultati hanno mostrato che in genere iMAR, in particolare se combinato con DE, comporta un miglior accordo tra dose prescritta e dose effettivamente rilasciata. É quindi stata dimostrata la potenzialità di questi algoritmi avanzati di correzione dell'immagine per il miglioramento dosimetrico di piani di trattamento in presenza di impianti metallici.

Contents

Acronyms

AP	Anterior-Posterior
CPT	Center for Proton Therapy
CT	Computed Tomography
CTDI	Computed Tomography Dose Index
CTV	Clinical Target Volume
DE	Dual Energy
DICOM	Digital Imaging and COmmunications in Medicine
DoF	Degrees of Freedom
EAN	Effective Atomic Number
EDRW	Electron Density Relative to Water
FBP	Filtered Back Projection
FOV	Field Of View
GTV	Gross Tumor Volume
HE	High Energy
HU	Hounsfield Unit
iMAR	Iterative Metal Artifact Reduction
IMPT	Intensity Modulated Proton Therapy
IR	Iterative Reconstruction
ITV	Internal Target Volume
IV	Irradiated Volume
KSB	KantonSspital Baden
LAT	LATeral
LE	Low Energy
LET	Linear Energy Transfer
MFO	Multi-Field Optimization
MRI	Magnetic Resonance Imaging
OAR	Organ At Risk
PBS	Pencil Beam Scanning
PET	Positron Emission Tomography
PPV	Patient Position Verification
PRV	Planning organ-at-Risk Volume

PSI	Paul Scherrer Institut
PTV	Planning Target Volume
RBE	Relative Biological Effectiveness
ROI	Region Of Interest
RPSP	Relative Proton Stopping Power
RVR	Remaining Volume at Risk
SAFIRE	Sinogram AFfirmed Iterative REconstruction
SE	Single Energy
SFUD	Single Field Uniform Dose
SNR	Signal-to-Noise Ratio
SOBP	Spread-Out Bragg Peak
SPECT	Single Photon Emission Computed Tomography
TCS	Therapy Control System
TDS	Therapy Delivery System
TPS	Treatment Planning System
TVS	Therapy Verification System
TV	Treated Volume
VOI	Volume Of Interest

Introduction

Thanks to the physical properties and the achievable steep gradients in Spread-Out Bragg Peak, heavy particles (protons and carbon ions) are emerging as therapy of choice over conventional photon radiotherapy to deliver dose to the tumor, while sparing healthy tissues. In order to fully exploit such advantages, it is important to be able to perform an accurate dose calculation and to reduce the involved uncertainties. Therefore, imaging plays an important role along the entire particle therapy treatment course, to delineate tumor and Organs At Risk, position the patient and predict the delivered dose. A very promising technique is Dual Energy Computed Tomography (DECT), which consists in the acquisition of two images at different energies. In oncology, focus has been on supporting diagnosis, tumor detection and characterization [Simons et al, 2014], as well as on radiotherapy support [van Elmpt et al, 2016]. In this work, that has been carried out for a duration of 8 months in the Center for Proton Therapy (CPT) at Paul Scherrer Institut (PSI, Villigen, Switzerland), we focused on two common radiotherapy issues, patient positioning and treatment of patients with metal implants.

In order to achieve high precision in irradiating the target while preventing damage to surrounding organs, it is of high importance to verify on a daily basis the position of the tumor with respect to the beam, in particular for proton therapy. In most of the cases, patient position is checked by comparing either a 2D or 3D image, acquired at planning, with another daily 2D or 3D set. The match is usually performed on bony anatomy, but in some cases, it is difficult to find corresponding structures, in particular when bones and tumor soft tissue are overlapping [Kortmann et al, 1994]. However, it has been shown that it is possible to obtain images which only contain soft tissue or bone by making use of additional spectral information related to Dual Energy X-ray imaging [Brody et al, 1981]. Based on this concept, we developed an algorithm to extract tumor- and bone-canceled images, using dual energy topograms as input. This tool allows to obtain two contrast-enhanced images, useful for recognizing different structures in the body. Therefore, using them inside the Patient Position Verification software, it is possible to insert easily reference landmarks, thus used for the evaluation of couch corrections needed for the correct patient positioning.

The second part of this thesis aims at comparing different imaging approaches, to deal with metal implants in the cervical spine, by means of experimental investigation on anthropomorphic head phantom. In fact, a substantial number of patients presenting paraspinal tumors often have metal stabilizing rods as a result of surgical intervention. These implants can be challenging for proton therapy. First of all, related metal artifacts introduce uncertainties in stopping power evaluation, between 1 and 10 mm [Verburg and Seco, 2013], making extremely difficult clinical volumes delineation. Secondly, the extremely sharp interfaces between metal and surrounding tissues degrade the accuracy of the dose calculation by Treatment Planning System [Lomax, 2008]. Different options have been analyzed. No correction of the artifacts and manual approach developed at Paul Scherrer Institut, already investigated in terms of impact on dosimetry by [Dietlicher et al, 2014], were compared with new tools recently introduced in CT, such as Siemens Iterative Metal Artifact Reduction (iMAR) [Morsbach et al, 2013a], [Morsbach et al, 2013b] and Sinogram Affirmed Iterative Reconstruction (SAFIRE) [Yang et al, 2013]. Finally, DECT in combination with iMAR was additionally investigated. The core of DE approach is the possibility of estimating tissue stopping power directly using the double information of the two acquired images, in order to find effective atomic number and electron density relative to water, instead of stoichiometric calibration curve, which relates CT number to Relative Proton Stopping Power (RPSP) [Schneider et al, 1996]. Several authors recently investigated this DE application for ion-therapy, especially for what concerns CT calibration [Bourque et al, 2014] and stopping power, from both simulation [Hansen et al, 2015], [Hudobivnik et al, 2016] and experimental [Hünemohr et al, 2013], [Hünemohr et al, 2014a], [Farace, 2014] perspectives. However, to our knowledge, no experimental measurement of clinically relevant plans has been performed yet. Therefore, this is the first experimental verification of DECT-based stopping power evaluation on anthropomorphic phantom.

In Chapter 1, basic concepts of proton therapy are reviewed, in particular the characteristic depth-dose curve of protons and the possible modalities for treatment delivery and better adapting the beam to the target's shape. Moreover, the PSI facilities are described. Chapter 2 provides an overview of CT as imaging modality, with the underlying physical principle, its traditional and recent applications in proton therapy, such as Dual Energy (DE), as well as technical aspects regarding the different types of scanners. In Chapter 3, contrast enhancement algorithm using DE images for improved patient positioning is discussed. Finally, Chapter 4 presents the second part of this thesis, regarding an experimental study of different approaches coming from imaging to help dealing with metal artifacts.

Part I

Background

Chapter 1

Proton Therapy

"Research is creating new knowledge."
- Neil Armstrong -

1 Advent of protons in cancer therapy

The first medical application of ionizing radiation, using X-rays, occurred in 1895 [Roentgen, 1896]. In the following decades, radiation therapy became one of the main treatment options in oncology. Many improvements have been made with respect the reduction of the dose to healthy tissue while maintaining prescribed doses to the target. Moreover, in the 1920s and 1930s fractionated radiation therapy has been introduced, as well as the exploitation of dose deposition characteristics offered by different types of particles.

The use of protons for tumor treatment was suggested in 1946 by R. R. Wilson, and the first real attempts to use proton radiation to treat patients began in the Fifties in nuclear physics research facilities. However, as the accelerators used were not specifically designed for treating patients, their energies were not high enough to treat deeply seated tumors. In the Seventies many advancements in the fields of imaging, software, accelerators and treatment systems occurred, giving proton therapy the opportunity to became more viable for routine medical applications of cancer treatment. Nevertheless, only in recent years proton beam facilities have been developed also in conjunction with established hospitals. The world's first hospital-based proton therapy center was the Massachusetts General Hospital (MGH) opened in the late Seventies, followed by Paul Scherrer Institut (PSI) in 1984. Subsequently, a low energy cyclotron centre for ocular tumors at the Clatterbridge Centre for Oncology in the UK, opened in 1989, followed in 1990 by Loma

Linda University Medical Center in California. Thanks to the property of protons to deliver dose mainly at the Bragg peak and basically zero beyond it, proton radiation has continued to be used as an effective treatment for cancer. The traditional indications for proton therapy have been treatments of head and neck, brain, and prostate cancer, but growing results from its application for other cancer types are proving to be positive. Today, over 100,000 people worldwide have received proton therapy, a number that is anticipated to grow larger and faster as new proton therapy centers continue to open within the next several years.

2 Principles of proton therapy

The main benefit of proton therapy over photon beam radiotherapy is the absence of exit dose, which offers the opportunity for highly conformal dose distributions, while simultaneously irradiating less normal tissue. This technology therefore reduces irradiation to normal tissue, while permitting dose escalation to levels hardly achievable with standard techniques [Lomax, 1999], [Levin et al, 2005].

2.1 Interaction of protons with matter

A proton is a subatomic particle with a positive electric charge equal to that one elementary and mass 938.272 MeV/c^2, slightly less than that of a neutron (939.565 MeV/c^2). Together with neutrons, protons are collectively referred to nucleons, since basic components of the nucleus of atoms.

The interactions between protons and matter can be classified in three main classes: stopping, scattering and nuclear interactions [Paganetti, 2011].

Stopping

The theory of stopping, developed in 1933, regards the slowdown caused by the myriad of electromagnetic interactions between protons and atomic electrons. This process is the underlying cause to the key feature of protons: they do stop in matter and beyond the stopping point the dose can be considered negligible.

The range, defined as the mean path length of protons with initial energy E_0 in matter, is formulated in the continuous slowing down approximation by [ICRU, 2005]:

$$R = -\int_{E_0}^{0} \frac{dE}{dE/dx} \; . \tag{1.1}$$

Although the mean rest kinetic energy is zero for the range definition, the stochastic nature of the energy loss causes “range straggling”. This means that if the proton beam is mono-energetic, all protons stop at nearly the same depth, with a slight spread in stopping point. This effect is enhanced if the incident beam itself has an energy spread. Usually, straggling of about 1.2% of range occurs for light materials and only slightly more for the heavier ones [Janni, 1982]. Taking into account the straggling, the definition of range can be specified as the amount of material that would stop half the incident protons that undergo only electromagnetic interactions.

Another characteristic signature is that the rate at which the proton loses energy, namely the “stopping power”, increases as the proton slows down. This is due to the fact that more momentum is transferred to the electron, the longer the proton stays in its vicinity [Paganetti, 2011].

Scattering

The theory of scattering, dating from 1947, concerns the deflection caused by the electromagnetic interaction between protons and atomic nuclei. However, this effect is extremely small if only one atomic nucleus is taken into account, thus the global result is the statistical outcome of countless tiny deflections. Hence, scattering is usually properly known as “multiple Coulomb scattering”. This interaction spreads the proton beam out laterally, with a spatial distributions very similar to a Gaussian, because sum of many small random deflections (Central Limit Theorem). Actually, the real distribution has a Gaussian core with an additional single scatter foil, due to the fact that the theorem cannot be really applied because large single scatters in the target are not rare enough [Kittel, 1967]. Typical values of the related half-width are around few degrees, with 16° in the worst case scenario [Paganetti, 2011].

In general, materials with higher atomic number are associated to a stronger scattering then the lighter ones.

Nuclear interactions

Nuclear interactions comprise head-on collisions of protons with nuclei setting secondary particles in motion. This type of interactions is not explained by a unified theory, but by a patchwork of models. In fact, they are far harder to model than stopping and scattering. However, their biological effect turn out to be small and approximations are sufficient for the design of radiotherapy systems.

The most interesting nuclear interactions are the nonelastic ones, where the proton enter the nucleus, producing secondary particles, such as protons,

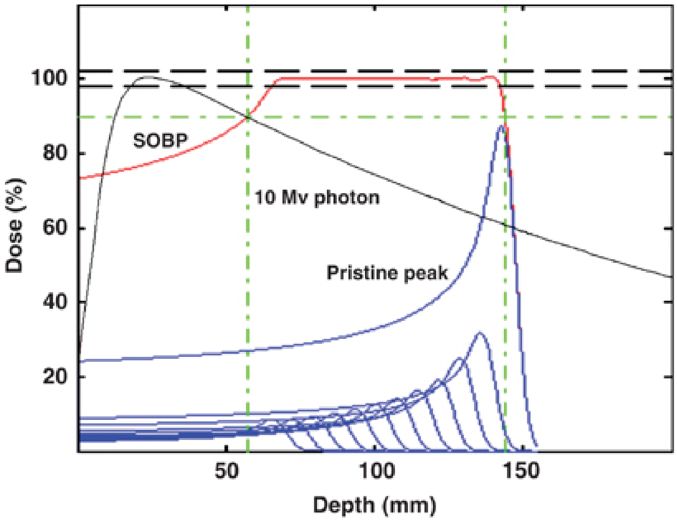

Figure 1.1: Depth–dose distributions for a SOBP (red), its constituent pristine Bragg peaks (blue) and a 10 MV photon beam (black). The dashed lines (black) indicate the clinical acceptable variation in the plateau dose of ±2%. The dot–dashed lines (green) indicate the 90% dose and the modulation width of the SOBP [Levin et al, 2005].

neutrons, γ-rays and heavy fragments (mainly alphas and recoiling residual nucleus), while depositing in the reaction site a blob of dose. These secondaries have much lower energies and much larger angles than primary protons.

For example, the percentage of 160 MeV protons suffering nuclear reactions before stopping is around 20% [Paganetti, 2011].

2.2 Depth-dose distribution

The depth-dose profile for protons is determined by the combination of the three interactions that can occur. After an initial plateau, the deposited dose rises up close to the end of the particle range, generating the so-called Bragg peak, beyond which it rapidly falls to zero. Instead, for photons, the depth-dose distribution is characterized by a rapid built-up to a maximum close to the entrance point, followed by a slow exponent fall-off (Figure 1.1). Consequently, due to the associated lower entrance dose, photons can reduce skin dose, although their exit dose cannot be neglected, especially if compared to the profile of protons.

To obtain a homogeneous depth-dose distribution over the target volume, a superposition of pristine Bragg peaks with proper intensities (number of protons per unit of time) and locations (energies) is created. Since these peaks spread out in depth, the obtained shape is called Spread-Out Bragg Peak (SOBP), shown in Figure 1.1. This type of dose distribution has several features. First of all, once matched the plateau region of the SOBP with the extension of the tumor, it delivers a uniform dose in depth across the target volume. Moreover, it preserves the sharp distal fall of the peak, thus also the ability to spare normal tissues located behind the target volume. Finally, its total entrance dose has increased from about 30% due to the deepest Bragg peak, to nearly 80% thanks to all the other shallower ones. The modulation width of the SOBP dose distribution is measured as the distance between the proximal and distal 90% of plateau dose values. This width can be controlled by varying the number and intensity of pristine Bragg peaks that are added, relative to the most distal pristine peak, to form the SOBP [Levin et al, 2005]. From the depth-dose distribution, the range of a proton beam can be best defined as the depth of penetration from the front surface of the stopping medium to the distal 80% point on the Bragg peak, relative to 100% on the top of it [Goiten, 2008].

The upward sweep of the Bragg peak is due to the fact that the rate at which a single proton loses kinetic energy increases as the proton slow down. Indeed, the stopping power is proportional to the inverse square of the velocity of the considered particles. Consequently, the local energy deposition rises sharply as proton slow down and, at the end of range, protons come to a stop and therefore the dose drops to zero. Specifically, the stopping power S of a medium is formulated in the Bethe theory by the Bethe-Bloch equation [Bethe, 1930], [Bloch, 1933]:

$$S \equiv \left\langle \frac{dE}{dx} \right\rangle = -k\rho_e \Big(\frac{z}{\beta}\Big)^2 \cdot \left(ln\Big(\frac{2m_e c^2 \beta^2}{I(1-\beta^2)} - \beta^2 - \frac{C}{Z} - \frac{\delta}{2}\Big)\right) \tag{1.2}$$

where $k = 51$ MeV fm^2, β is the ratio between the velocity of the projectile and the speed of light, z and Z are the atomic numbers of the projectile and of the medium respectively, I is the mean excitation energy of the medium and ρ_e the electron density per volume of the medium. The shell correction C/Z becomes important at projectile velocities comparable or smaller than the orbital electron velocities. Completely stripped ions then start to capture atomic electrons from the medium, so reducing the medium's charge and therewith the stopping power (up to 6% for 1-100 MeV protons) [Ziegler et al, 2008]. The density correction term $\delta/2$ accounts for the dielectric polarization of the medium due to the ions' electromagnetic field. This effect reduces the stopping power particularly for large projectile energies that are usually not employed for particle therapy (1% for 500 MeV protons) [ICRU, 1993]. The electron density per unit volume of a compound is defined by:

$$\rho_e = \rho N_A \sum_i w_i \frac{Z_i}{A_i} \tag{1.3}$$

where ρ is the mass density of the medium, N_A the Avogadro's number, while Z_i, A_i and w_i are atomic number, mass number and mass weight of the i-th element belonging to the compound. The mean excitation energy I is instead defined as the mean energy $\langle E_i - E_0 \rangle$ required to excite an atomic electron from its initial ground state E_0 to any excited state E_i [Sakurai and Tuan, 1993]. However, the determination of the mean excitation energy is the principal non-trivial task in the evaluation of the Bethe-Bloch formula, due to the complexity of the electronic configuration in atoms of more than one electron or even molecules.

Actually, the quantity considered for the analytical dose planning algorithm in particle therapy is the stopping power ratio $\hat{S}$ of a medium relative to water, also called Relative Proton Stopping Power (RPSP) ratio. It can be approximated without shell and density correction by the following ratio [Schneider et al, 1996]:

$$\hat{S} \equiv \frac{S}{S_w} \approx \frac{\rho_e}{\rho_{e,w}} \cdot \frac{ln\left(\frac{2m_e c^2 \beta^2}{I(1-\beta^2)} - \beta^2\right)}{ln\left(\frac{2m_e c^2 \beta^2}{I_w(1-\beta^2)} - \beta^2\right)} = \hat{\rho_e} \cdot f(\beta, I, I_w) \ . \tag{1.4}$$

The RPSP is then linear in the electron density of the medium relative to water $\hat{\rho_e}$:

$$\hat{\rho_e} \equiv \frac{\rho_e}{\rho_{e,w}} = \frac{\rho \cdot \sum_i w_i \frac{Z_i}{A_i}}{1 \ g/cm^3 \cdot (11.11 \cdot \frac{Z_H}{A_H} + 88.89 \cdot \frac{Z_O}{A_O})} \tag{1.5}$$

where the subscripts H and O refer to hydrogen and oxygen, components of water. The RPSP is considered largely energy independent above energies of about 15 MeV/nucleon (energy dependence below 0.4%) [Yang et al, 2012] and therefore is ignored by most analytical dose planning system. For this reason, considering mean particle energy of 200 MeV/nucleon and setting the mean excitation value of water to 75 eV, Equation 1.4 can be approximated to:

$$\hat{S} \approx \hat{\rho_e} \cdot \frac{12.77 - ln(I)}{8.45} \ . \tag{1.6}$$

2.3 Biological effects

Radiotherapy uses ionizing radiation in order to damage the cell's DNA, causing a cell to lose its ability to reproduce. The higher the dose, the greater the probability of sterilizing cells and killing a tumor. Such damage is experienced by both the malignant cells and the ones belonging to healthy tissues.

An important parameter related to biological effects is the Linear Energy Transfer (LET). It is defined as the energy transferred to the absorbing medium per unit track length of the particle [Paganetti, 2011]:

$$LET_{\Delta} = \left(\frac{dE}{dl}\right)_{\Delta} \tag{1.7}$$

where the subscript Δ indicates the maximum amount of transferred energy considered for the calculation. Photons have a low LET, as do electrons, while protons have a low LET when they enter the phantom, but an high density of ionization, i.e. high LET, around the Bragg peak region. For low-LET radiation the damage to DNA is relatively rare and the damage sites are well separated, consequently there is a good chance to be repaired correctly. On the other hand, with an increasing LET the ionization density increases and the DNA damage is likely to be pronounced in sites of close proximity. However, LET is a macroscopic rather than microscopic parameter, since deals with the energy loss per unit path length rather than energy loss in sub-cellular volumes.

Moreover, protons are more biologically effective than photons. That is to say that the fraction of cells surviving a particular dose of photons is larger than the fraction of cells surviving the same dose of charged particles, such as protons. In order to take that into account, another parameter is introduced, the Relative Biological Effectiveness (RBE). It is defined as the ratio between the dose of a reference radiation of a standard X-ray D_X and the dose of the considered radiation D_{rad} that causes the same biological effect (i.e. same surviving fraction of cells) [ICRU, 1979]:

$$RBE = \frac{D_x}{D_{rad}} \; . \tag{1.8}$$

RBE increases with increasing LET up to a certain maximum. If the LET is further increased, far fewer tracks are required to deposit the same dose, leading to saturation of the effect and eventually to a decrease of RBE with increasing LET [Goodhead, 1990].

Since prescribed doses to the target, dose constraints to critical structures and fractionation schemes are largely based on clinical experience gained with photon therapy, prescription doses for proton therapy are also defined as photon doses. Therefore, the RBE adjusted dose has been introduced, defined as the product of the physical dose and the respective RBE. Before 2008 proton doses were given in Cobalt Gray Equivalent (CGE), and then it was changed to reporting D_{RBE} as Gy(RBE) [ICRU, 2007]. Most proton therapy treatment facilities have adopted a generic RBE of 1.1. This value is mainly based on animal experiments performed in the early days of proton therapy [Dalrymple et al, 1966], [Tepper et al, 1977], [Urano et al, 1980]. However, differences in biological effect occur not only between X-rays and protons, but also between protons at different energies, as well as depth of penetration, biological endpoint, dose per fraction, position in the SOBP and particular tissue [DeLaney and Kooy, 2008]. Nevertheless, there are no clinical data indicating that the use of a generic RBE of 1.1 is unreasonable.

3 Proton dose delivery

Proton therapy provides a tool for delivering highly conformal dose distributions, since they show the attractive physical characteristic of having a well-defined range, beyond which no energy is deposited. However, the resulting proton dose distribution is strictly related to the technique used for the delivery, as well as the type of treatment plan defined on the patient.

3.1 Beam delivery systems

After the protons are accelerated, either by cyclotron or synchrotron, they are transported into the treatment room through the beam line. The output proton beam is mono-energetic, with a lateral spread of only few millimeters. Clinical use of the proton beam requires both spreading the particles to a useful uniform area in the lateral direction, as well as creating a uniform dose distribution in the depth direction. The main function of the treatment head, also called “nozzle’, is shaping the proton beam into a clinically useful 3D dose distribution [Paganetti, 2011]. Two modalities of beam spreading are used: passive scattering [Koehler et al, 1975], [Koehler et al, 1977] and active scanning [Kanai et al, 1980], [Pedroni et al, 1995] (Figure 1.2). With the last approach, the full potential of protons can be exploited as the Bragg peaks can be deposited anywhere in three dimensions within the tumor volume.

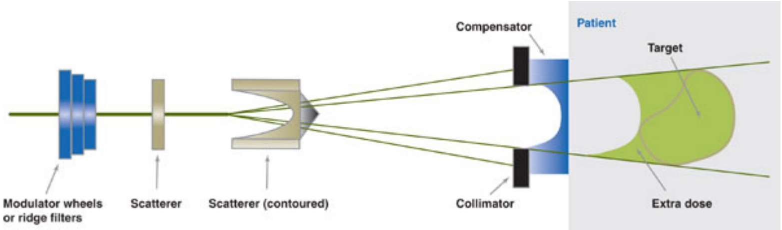

(a)

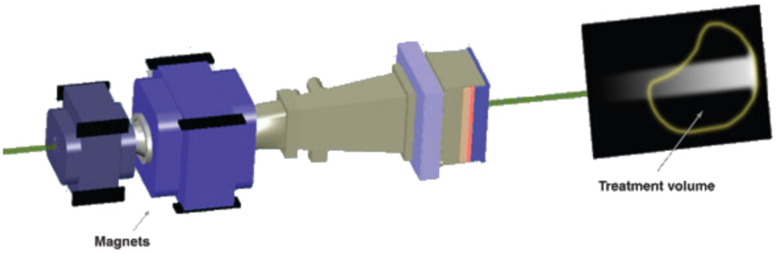

(b)

Figure 1.2: Schematic diagrams of passive scattering (a) and active scanning techniques (b) [http://medicalphysicsweb.org/cws/article/opinion/42793].

Passive scattering

Passive scattering is a delivery technique in which range shifting and scattering materials spread the proton beam (Figure 1.2/a).

In order to have a uniform dose region along the depth direction, Bragg peaks are shifted in depth and given an appropriate weight, so that the SOBP is created by combining these proton beams of decreasing energy. This method of adding pristine peaks is called "range modulation". Depending on the size of the target to be covered, the extent can be adjusted by changing the number of peaks. There are three principal range modulation techniques:

- Energy stacking. It is the easiest method because no dedicated nozzle elements are required since the energy of the protons is changed at the accelerator level. This can be achieved either by changing the extracted synchrotron energy or the energy-selection system setting at the exit of the cyclotron.
- Range modulator wheels. This method has been proposed by Wilson in his original article about proton therapy [Wilson, 1946] and continues nowadays to be the most common approach in clinical proton-scattering systems. A range modulator wheel has steps of varying thickness and a certain angular frequency. Each step corresponds to a certain Bragg peak, that is irradiated sequentially during the rotation. The thickness

of a step determines the range shift of the related pristine peak, while its angular width affect the number of protons hitting the step, thus the weight of the peak.

- Ridge filters. It is a stationary device composed of tens of bars, where each bar has the same ridge shape. The range of protons in a spot is modulated according to the position they pass through, resulting in the broadening of the Bragg-peaks. The principle is the same as the modulator wheel: thickness and width of the steps determine respectively the range and the weight of the peaks.

The uniformity of the dose along the lateral dimensions is instead achieved thanks to designed specifically scatterers. The simplest scattering system is a single, flat scatterer that spreads a small proton beam into a Gaussian-like profile. Typically the scatterers are high-Z materials, e.g. lead and tantalum, providing the largest amount of scattering for the lowest energy loss. Due to its low efficiency, defined as the portion of protons inside a useful radius, this approach is limited to small fields with a diameter lower than 7 cm [Paganetti, 2011]. To overcome this limitation, a double scattering system can be used to scatter more of the central protons to the outside and create a flat profile. Usually a flat scatterer spreads the beam onto a contoured one, so that the profile is flattened at some distance. Since this contoured scatterer is thick in the center and thin on the outside, protons hitting the center lose more energy than the those going through the periphery. For that reason, normally the high-Z scattering material is combined with a low-Z compensation material, e.g. plastic, with thickness designed to provide constant energy loss, while maintaining the appropriate scattering power variation. Hence, the thickness of the scatterer decreases with distance from the axis, whereas for the compensation material increases. If the energy-compensated contoured scatterer is used, the energy of the protons need to be increased in order to achieve the same range in the patient as with an uncompensated scatterer.

Finally, to conform the dose to the target, field-specific apertures and range compensators are used. The first ones block the beam outside the target and adjust the beam laterally, while the compensator is a variable range shifter that conforms the beam to the distal end of the target. This conformity is in 2D, as the SOBP is constant and equal to the maximum required to cover PTV.

Active scanning

The principle of active scanning proton therapy have been first proposed by [Kanai et al, 1980] and is strictly connected to the fact that protons are charged particles, thus can be deflected by magnetic fields (Figure 1.2/b). This approach was clinically implemented first at Paul Scherrer Institut (PSI), where patients have been treated since 1996 on a fully rotational treatment gantry [Pedroni et al, 2004], [Lomax et al, 2004]. In active scanning, also called Pencil Beam Scanning (PBS), the beam transported to the nozzle is directly sent to the patient without interacting with any scattering or energy-modulation devices. Active scanning has proven to be very good for clinical treatment as it modulates the dose in 3D, also proximal to the tumor, and not in 2D as for passive scattering.

This technique consists in the superposition of individual Bragg peaks, positioned in 3 dimensions inside the tumor's volume. The 3D allocation of these peaks is in general performed thanks to sweep magnets. However, the mechanical configuration can be different depending on the gantry. For example, at PSI, Gantry 1 and Gantry 2 are based on different systems: the first one uses one sweep magnet only and the movement of the couch, while the latter one exploits magnets along 2 dimensions. The third dimension is instead covered by changing the energy of the beam. For a synchrotron it can be simply varied changing the applied fields, while in case the accelerator is a cyclotron a degrader at the exit must be used. Moreover, range-shifter within the nozzle allows the delivery of Bragg peaks close to the patient surface. This expedient is introduced in order to have a proton beam with sufficient intensity, condition unreachable using the degrader only.

In traditional active scanning, namely discrete spot scanning, the dose is applied in discrete steps both laterally and in depth, with each position typically being called a spot. When the beam is on this spot is static and, after each spot, the beam is switched off and the magnetic and/or energy settings are changed to move to the next spot. The time required for these changes is called dead time. As a consequence of this, the total treatment time is substantially longer than the actual beam-on time, in which dose is delivered. A reduction in dead time can be achieved by scanning the beam continuously, at least along one of the axes in the lateral plane. This concept leads to the continuous line scanning. Therefore, another modality of PBS have been developed, called continuous line scanning. By modulating the scanning speed and the beam intensity, it is possible to apply almost arbitrarily complex, inhomogeneous proton fluences along each line. In this mode, position and dose checks are either performed during irradiation, after scanning a single line or after each isoenergy layer. Continuous line scanning can be considered as a superposition of an infinite number of spots on a scanning grid with an infinitesimal spacing [Schätti et al, 2014].

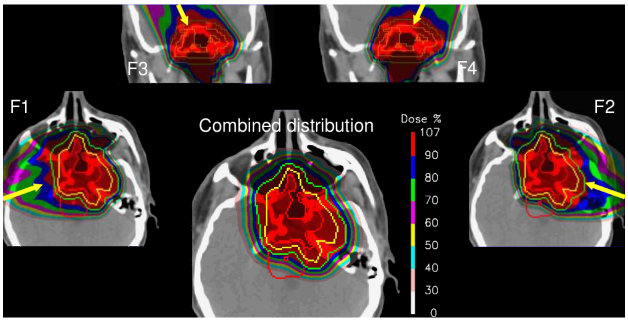

Figure 1.3: Example of SFUD plan to a large and complex skull-base chordoma, the same in Figure 1.3, together with the associated individual field dose distributions making up the total plans. The critical structure is contoured in red, i.e. the brainstem [Paganetti, 2011].

3.2 Treatment plans

Typically, two major categories of plans can be delivered, namely Single Field Uniform Dose (SFUD) and Intensity Modulated Proton Therapy (IMPT) plans [Lomax, 1999], [Lomax et al, 2001], [Lomax, 2008]. The first method can be delivered with passive scattering as well as by means of pencil beam scanning, while IMPT is restricted to active scanning only.

For both SFUD and IMPT with PBS, the treatment planning system considers pencil beam Bragg peak explicitly, rather than their combinations of any type as for scattering, and the quality of the beam is determined largely by the quality of the individual pencil beam [Lomax, 1999], [Pedroni et al, 2004]. The specification of a treatment beam is basically a list of Bragg peaks, each with the energy of the proton, the lateral location of the peak projected unto the isocenter plane and the number of protons, often given in the unit of Giga-protons [Paganetti, 2011].

SFUD

In treatment planning of proton therapy for Single Field Uniform Dose, each field is composed of different Bragg peaks with weights optimized in such a way that the single field dose distribution in the target is homogeneous. The plan is obtained by linear combination of individually optimized fields, which improves the dose homogeneity in the tumor, while distributing the entrance dose on a larger surface (Figure 1.3).

This approach essentially arises from passive scattering delivery, since also in this case the delivered SOBP applies a uniform dose across the target. However, there are few notable differences. In particular, the active scanning

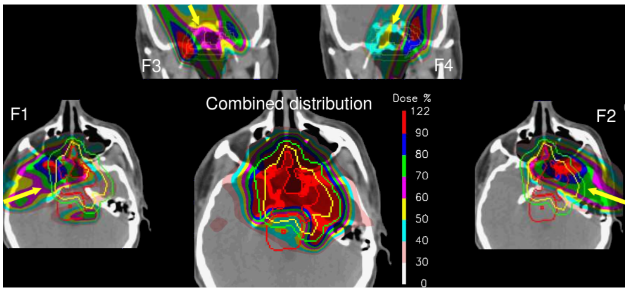

Figure 1.4: Example of IMPT plan to a large and complex skull-base chordoma, the same in Figure 1.3, together with the associated individual field dose distributions making up the total plans. The critical structure is contoured in red, i.e. the brainstem [Paganetti, 2011].

approach adds some flexibility, allowing both distal and proximal conformity for a single beam, thanks to the fact that range and modulation width are set on a per-proton-ray-beam basis [Paganetti, 2011]. For this reason, SFUD with active scanning can be considered more efficient in that only Bragg peaks delivered within, or close to, the target [Albertini et al, 2010].

IMPT

In treatment planning of proton therapy for Intensity Modulated Proton Therapy, also called Multi-Field Optimization (MFO), the desired homogeneous target dose coverage is achieved only by the combination of two or more treatment fields, each of which can deliver a highly inhomogeneous dose distribution to the target (Figure 1.4). The resulting plan is given by the simultaneous optimization of all Bragg peaks from all fields.

With this technique, the weight of the spots is optimized taking into account also the dose to healthy tissue and Organ At Risk (OAR) close to or embedded in the target. Depending on the anatomy and field direction, certain parts of the target can be irradiated only by certain fields. Moreover, another difference in this approach is that the uniform single field constraint is removed and the optimization is given full reign to weight Bragg peaks regardless of the final form of the individual field dose distributions, as long as the total dose, addition of all the individual field dose distributions, combines to give the desired result. For these reasons, the IMPT approach best exploits the full potential of scanned proton therapy, in fact it provides even more flexibility in tailoring the dose distribution to the target and in selectively avoiding critical structures [Albertini et al, 2010].

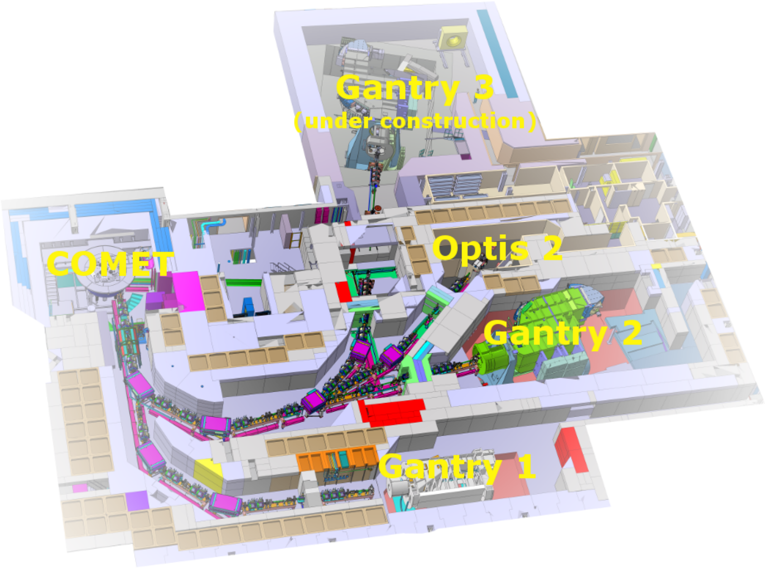

Figure 1.5: Illustration of the facilities for proton treatment at CPT, in PSI: the cyclotron COMET, OPTIS 2, Gantry 1, Gantry 2 and Gantry 3 (under construction).

4 PSI facilities

The Center for Proton Therapy (CPT) at Paul Scherrer Institut (PSI) is in operation since 1984, with more than 7.965 patients treated. Furthermore, since 1996 the center introduced the pencil-beam scanning technique, for treating larger and deep seated tumors, as for example chordoma and chondrosarcoma of the skull base or along the spinal cord. In fact, PSI has developed the worldwide first compact scanning gantry for the irradiation of deep seated tumors with proton beam.

The entire proton delivery system is shown in Figure 1.5. Core of the facility is COMET, a 250 MeV superconducting cyclotron where the protons are accelerated. The beam is then deflected by means of electromagnetic switches to one of the three therapy stations (Gantry 1, Gantry 2 and OPTIS 2), within less than a thousandth of a second. All hardware and software for control and safety systems of these three rooms have been completely developed at PSI. A third Gantry, with same capabilities as Gantry 2 on a technical level, is currently under construction and should be ready for patient treatment in 2017.

Figure 1.6: OPTIS 2 at PSI: gantry dedicated to treatment of ocular tumors using passive scattering technique.

4.1 OPTIS 2

OPTIS 2 (Figure 1.6) is dedicated to treatment of ocular tumors using passive scattering technique with a fixed horizontal beamline. It is the newer and more advanced version of its ancestor facility, OPTIS 1, that has been in operation from 1984 to 2010.

The patient is seated in a treatment chair facing the nozzle with head immobilized using individualized mask and bite block. The chair is mounted on a hexapod robot allowing the positioning of the patient with 6 degrees of freedom. For allowing the localization of the tumor during the treatment with sub-millimeter accuracy, several small clips are sutured on the sclera (eye surface) in the proximity of the target during previous surgical operation. For positioning the patient in the most accurate way, OPTIS 2 uses two X-rays, aligned with the treatment isocenter so to provide orthogonal images of the eye of the patient. The patient has to fix a LED light throughout the treatment, whose position is optimized at the time of planning as a compromise between patient comfort and best entrance direction of the beam, in order to cover in a better way the extension of the tumor, while sparing as much as possible eyelid and pupil. Intrafractional motion of patient eye is monitored using beam's eye view camera.

As eye tumors are shallow, the energy used for this type of tumor is 70 MeV. However, during the energy degradation from 250 MeV (energy given by the cyclotron) more than 99% of the original protons is lost. For that reason, in order to ensure higher efficiency of transport, a double-scattering process is implemented in OPTIS 2. The extracted beam passes through a range shifter, used for setting the range and ensuring pre-scattering of proton pencil beam. Subsequently, the beam encounters a scatter foil, which broadens the beam and ensures homogeneous field at the isocenter. Depend-

Figure 1.7: Gantry 1 at PSI: gantry dedicated to treatment with scanning technique, in operation since 1997.

ing on the needed ranges, 9 scatter foils are available. The SOBP is then realized using dedicated modulator wheels. The maximal diameter of the circular field is 35 mm, reduced for each patient using individually milled copper collimator aperture.

4.2 Gantry 1

Gantry 1 (Figure 1.7) is the first facility worldwide that used active scanning technique for treatments of deep-seated tumors. It is operational since 1997, treating tumors located mainly in the skull, spinal chord and in the pelvis.

The transverse movements of the pencil beam are done with a fast scanning magnet and patient-table motion respectively, while the third dimension (depth) is varied adjusting the beam range. To do that, 40 range-shifter plates of polyethylene are placed into the beam path by means of a pneumatic system, at the nozzle level. To ensure quality and safety of delivery, the beam is monitored in the nozzle using two plane-parallel ionization chambers for checking the dose, a strip chamber for controlling in two dimensions position and width of the beam.

The weak points of Gantry 1 are [Pedroni et al, 2004]:

- the unsatisfactory access to the patient table when the beam is applied from below;
- the slow speed of scanning, that is a limitation for applying repeatedly target repainting and, this makes the treatment of moving organs not really possible on this gantry.

Figure 1.8: Gantry 2 at PSI: gantry dedicated to treatment with scanning technique, in operation since 2013.

4.3 Gantry 2

The positive experience of using the scanning technique brought in the year 2000 the decision of PSI to expand and upgrade the facility. It is in the frame of this new project, called PROSCAN, that the realization of Gantry 2 was planned [Pedroni et al, 2011]. Treatments in this gantry (Figure 1.8) started in 2013. The design of the Gantry 2 is derived from the practical experience of using Gantry 1, but is substantially improved and renewed.

For what concerns the layout, Gantry 2 has a larger diameter, of 7.5 m (isocentric), with respect the 5 m (eccentric) of Gantry 1.

The major improvement is about the speed of the beam delivery. In fact, two high-speed magnets (scanning speeds of 2 cm/ms and 0.5 cm/ms for the two axes) are used to scan through the tumor in two dimensions. This double scanning and the isocentric layout permit comfortably large space around the couch, thus fast and easy access to the patient table. The depth of penetration of the protons can change from one tumor layer to the next one in about 100 ms (80 ms for 3 MeV energy changes). That approach permits to generate dose distributions less sensitive to organ motion and allows to implement repainting. Moreover, on this machine both discrete and continuous line scanning can be applied [Schätti et al, 2014]. However, for now, only the discrete approach is used on patients.

In addition, the components in the nozzle are designed to have as little material as possible along the beam path. This maintains a small spot size at all energies (width lower than 4 mm for 100-230 MeV). The nozzle can be also extended to reduce the air gap between the beam line exit window and the patient, mitigating in this way the angular spread of protons. An electronically controlled range-shifter of 4 cm water-equivalent thickness is mounted within the nozzle and can be remotely positioned into the beam to allow the delivery of Bragg peaks close to the patient surface (proton's energy lower than 70 MeV) [Scandurra et al, 2016].

A further notable development is the in-room imaging: a sliding CT, used for treatment planning and for the daily verification of the patient position. This allows to reach the CT in a single movement of the patient table. Moreover, another X-ray system is mounted on the gantry itself, which takes images in the direction of the proton beam, the so called "Beam's eye view". Thanks to its fluoroscopy capability, it provides increased precision and quality assurance, in particular in the treatment of moving tumors.

Chapter 2

Computed Tomography

> *"We often mark our progress in science*
> *by improvements in imaging."*
> - Martin Chalfie -

1 Principles of CT

X-ray imaging is based on the absorption of X-rays as they pass through the body of the patient. The amount of radiation absorbed during this process contributes to the dose released to the patient. In particular, X-rays can be used in two modalities: radiography and tomography. In the first one, 2D image is generated by recording residual radiation after interaction with the body of the patient. The first radiograph dates from 1895, when Wilhelm Conrad Röntgen took a picture of his wife's hand on a photographic plate (Figure 2.1/a). Computed Tomography (CT), instead, although also based on the variable absorption of X-rays by tissues, provides a different form of imaging, known as cross-sectional imaging. In fact the origin of the word "tomography" is Greek: "tomos" slice, section and "graphe" drawing. The first CT image dates from 1971, when Godfrey Newbold Hounsfield and James Ambrose reconstructed an image of a woman with a suspicious cerebral tumor in the frontal lobe (Figure 2.1/b). Basically, the term tomography refers to the reconstruction of an image using its projections at different angles. The polychromatic photon beam of incident intensity $I_0(E)$ and energies E is attenuated exponentially by the scanned object in accordance with the Lambert-Beer law:

$$I = \int I_0(E) e^{-\int \mu(x,y,E) dl} dE \tag{2.1}$$

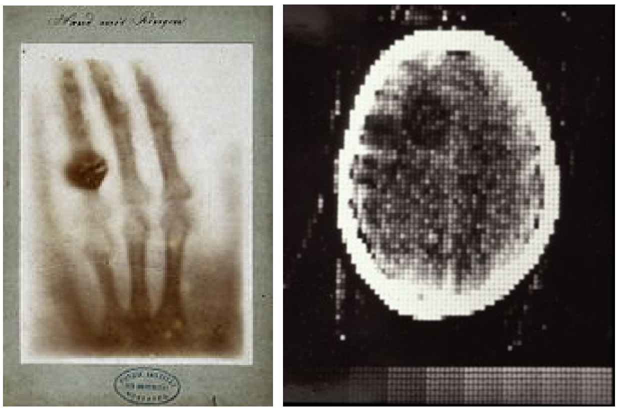

(a) (b)

Figure 2.1: First radiograph (on the left) and CT image (on the right) in the history, obtained respectively in 1895 and 1971.

that describes a single projection along a line l, where μ is the linear attenuation coefficient. The set of multiple projections acquired under different angles in one x-y plane is called sinogram. It is the starting point for the reconstruction of a 2D map of the linear photon attenuation coefficient of the object, namely the single slice. The repetition of this process for different planes gives the entire 3D CT reconstruction, i.e. a map in x, y and z of the spatial distribution of photon attenuation coefficients of the scanned object.

It has to be specified that in CT images, the measured μ of the voxel is presented in respect of the linear attenuation coefficient of water μ_w as the so called CT number, defined by:

$$CT\# = 1000 \cdot \frac{\mu - \mu_w}{\mu_w} \; (HU) \; . \tag{2.2}$$

The CT number is measured in Hounsfield Units (HU), in honor of the CT inventor Godfrey Hounsfield [Hounsfield, 1973], and it has been introduced in order to have a quantity comparable between different systems. Two fix points for the CT calibration are 0 HU and -1000 HU, respectively related to water and air.

1.1 Interaction of photons with matter

The linear attenuation coefficient μ represents the macroscopic cross section, which means that it can be expressed as the atomic cross section σ_a times the number of atoms per unit of volume n. Due to the relations between σ_a

and the electronic cross section σ_e ($\sigma_a = \sigma_e \cdot Z$) and between n and the mass density ρ, μ can be parametrized as follows:

$$\mu = \sigma_e Z \cdot \frac{\rho N_A}{A} \tag{2.3}$$

where Z is the atomic number, A the mass number and N_A the Avogadro's number. Since σ_a, for N initial number of photons and ΔN photons interacting per unit of time in a thickness Δx, is defined as:

$$\sigma_a = -\frac{\Delta N/N}{\Delta x \cdot n} \tag{2.4}$$

μ can be interpreted as the probability of photon interaction with matter per unit path length.

At commonly used X-ray voltages (up to 150 kVp), the interactions with higher probabilities between photons and matter are the photoelectric effect, incoherent and coherent scatterings. All these effects contribute to the total interaction probability.

Photoelectric effect

The photoelectric effect is the interaction of a photon with an electron belonging to an inner shell, whereby the total energy of the photon is absorbed. This electron, commonly called photoelectron, is finally ejected from the atom with an energy given by the difference between the energy of the incident photon and the electron's binding energy. The atom is therefore left in an excited state and consequently, when the vacancy of the inner shell is filled by an outer electron, the atom can either emit fluorescent radiation at characteristic energies or an Auger electron. The probability of this effect decreases with increasing energy and increases strongly with the atomic number, which is responsible for the excellent CT contrast between soft tissue and bone. For this reason, the electronic cross section of the photoelectric absorption is proportional to [Johns, 1983]:

$$\sigma_e^{photo} \propto \frac{Z^n}{E^{3.5}}; \quad n \sim 3-4\ . \tag{2.5}$$

Incoherent scattering

The incoherent scattering, or Compton effect, describes the inelastic scattering of a photon on an electron belonging to an outer shell. The transfer of part of the photon's energy to this latter depends on the photon's scattering angle θ:

$$\Delta\lambda = \frac{h}{m_e c}(1 - cos\theta) \tag{2.6}$$

where $\Delta\lambda$ is the difference between the wavelengths of scattered and incident photon, h the Planck constant, m_e the electron's mass and c the velocity of light in vacuum.

The incoherent scattering cross section for photons of incident energy $x = E/m_e c^2$ on free stationary electrons is formulated by the equation of Klein-Nishina [Johns, 1983]:

$$\sigma_e^{KN}(E) = \frac{3}{4}\sigma_T\Big(\Big(\frac{1+x}{x^2}\Big)\Big(\frac{2(1+x)}{1+2x} - \frac{ln(1+2x)}{x}\Big) + \frac{ln(1+2x)}{2x} - \frac{1+3x}{(1+2x)^2}\Big) \tag{2.7}$$

where σ_T is the Thomson cross section, with value $2.8 \cdot 10^{-13}$ cm^2. Recalling also Equation 2.3, it can be deduced that Compton scattering depends solely on tissue's electron density. In fact the light soft tissue contrast of CT is mainly determined by that.

Coherent scattering

The coherent scattering, or Rayleigh effect, describes the completely elastic scattering of a photon on an electron belonging to an outer shell. No transfer of energy occurs and the photon only undergoes to a change of direction.

The probability for this effect is higher for decreasing energy photons and increasing Z materials:

$$\sigma_e^{cohe}(E) \propto \frac{Z^{2.5}}{E^2} \ . \tag{2.8}$$

At diagnostic photon energies, coherent scattering is usually negligible compared to the other two interactions. The only exception is mammography, where X-ray energies between 15 keV and 30 keV are employed and the effect is therefore more relevant.

1.2 CT scanners

The CT acquisition system is composed by a source of X-ray, a detector and a table used for supporting the patient.

The tomographic acquisition system has quickly evolved over the last few years, with the purpose of speeding up the process of acquisition, in order to reduce the effect of movements and the delivered dose [Kohl, 2005]. In fact, effective dose values below 1 mSv are now routinely possible for a number of dedicated examinations, less than the annual natural background radiation (3.1 mSv/year on average in the United States) [Lell et al, 2015]. The first method of acquisition is the so-called incremental or serial CT. Basically, it is a step-and-shoot method, where each slice is acquired individually, with incremental steps of both tube and detector in between. Four generations of incremental CT have been developed. CT scanners belonging to the first one had just one detector, a pencil-like X-ray beam, with tube-detector movement composed by both translation and rotation, so to acquire projections at different angles. The duration of scan was on average 25-30 minutes. With the second generation, the elements of the detector became multiple (up to 30) with a fan-shaped X-ray beam. Also in this case the required movements were translation-rotation, though the steps needed for the translation were reduced, thus reducing the scan duration to less than 90 seconds. The third generation still used fan-shaped X-ray beam, but extended the number of detector's elements to 288 (newer ones use over 700) arranged in an arc, in order to cover the whole extension of the patient. In this way the translation is not needed anymore and the duration of the scan is approximately of 5 seconds. Expanding the arc to a fixed ring was the main change introduced by the fourth generation: only the X-ray tube rotates and the scan time is just few seconds. Nowadays helical, or spiral, CT image acquisition is the most affirmed method [Hsieh, 2009]. The patient is moved through a rotating X-ray beam and detector set. This means that the X-ray tube and detector perform a "spiral" movement with respect to the patient. That results in a three-dimensional fast and continuous data set acquisition, which can then be reconstructed into sequential images for a stack. Helical CT allows a scan to be performed in a single breath-hold and, for this reason, the major advantages are related to its speed and to the consequent reduction of misregistration from patient movement or breathing [Wilting, 1999]. With the introduction of the helical CT, new parameters affect the measurements. First of all the rotation time, that is the time required to scan the totality of 360°. It is usually 0.5-1 s, even though the newest CT scanners can achieve 0.28 s, less than an heartbeat. Another important parameter is the so-called pitch, defined as the table feed per gantry rotation divided by the beam collimation. It has typical values between 0.1 and 1.5: if it is smaller than one, the X-ray tube oversamples the measurement volume and gives an higher dose to the patient.

In CT scanners, X-rays are generated at the anode of X-ray tube, by acceleration of electrons emitted by cathode. Their kinetic energy is mostly converted to heat and only a small fraction, less than 1%, is emitted as X-ray radiation. This latter appears in two forms: Bremsstrahlung (around the 80%), due to the Coulomb scattering, and characteristic X-rays (around the 20%), caused by the filling of the vacancies created inside the atom of the target by the incident electrons. This results in a polychromatic and continuum spectrum that decreases linearly with increasing photon energy, with overlapped peaks at energies dependent on the target material of the anode. The maximum kinetic energy that the electrons can release to the Bremsstrahlung-photons depends on the applied voltage, which therefore determines the "quality" of the photon energy spectra. The tube current, instead, fixes the quantity of photons produced, thus the image quality. The current is often expressed as "tube current-time product", measured in mAs and defined as the product of the tube currents with the rotation time. Another possibility is to use the so called "effective mAs", or "exposure", that is the tube current-time product divided by the pitch.

1.3 Reconstruction techniques

Once acquired the detected photon intensities, these must be processed in order to reconstruct the final 3D image of the patient.

The most common method for image creation is the so called Filtered Back Projection (FBP). The basic idea of this technique dates from 1917, when the mathematician Johann K. A. Radon succeeded in solving the problem of the reconstruction of an object using its projections: he introduced the Radon's transform, that permits to reconstruct the value of a function knowing the values of its integrals over all the straight lines of the plane. However, his theory had received no attention until the Sixties, when the physician Allan McLeod Cormack solved with this transform some mathematical issues encountered during his studies about tomography. The purpose of FBP is the inversion of the Radon's transform of the object, which means to determine the linear attenuation coefficients of the object from the knowledge of its sinogram: each projection is spread backward along the same direction of its acquisition, namely it is back-projected. In this way, the value $ln(I_0/I)$ is associated to every pixel that are along the same line. This process creates star artifacts, that tend to be masked with increased number of projections. Furthermore, the convolution with a high-pass filter (ramp filter) is necessary as the radial symmetry in CT imaging would provoke a 1/r blurring of the back-projected image [Zargar et al, 2015]. This is due to the fact that the density of geometrical X-ray beam paths increases towards the center of the image. Since a convolution in the spatial domain is equivalent to a multiplication in the frequency domain, the projections recorded under different angles θ are first Fourier-transformed ($P(\omega, \theta)$) and then multiplied with the convolution kernel $|\omega|$ in the frequency domain. Finally, the inverse Fouriertransform is back-projected in order to yield $\mu(x,y)$ in the spatial domain. So, the FBP algorithm can be summarized as:

$$\mu(x,y) = \int_0^{\pi} d\theta \int_{-\infty}^{+\infty} P(\omega,\theta)|\omega|e^{i2\pi\omega t} \ . \tag{2.9}$$

Besides standard Filtered Back Projection, Iterative Reconstruction (IR) methods have been recently investigated [Grant and Raupach, 2012]. They are well-understood techniques, commonly used for SPECT and PET, that create the image looping iteratively through image reconstruction cycles. In traditional IR, once an image is reconstructed from the measured projections (raw data), a forward projection, back through the original image, is performed to re-create an estimate of the raw data. This forward projection simulates the CT measurement process, but now, the image serves as the measured object in place of the patient. The differences between measured and simulated projections are used to reconstruct a corrected image, which in turn, is used to update the original image. In each update cycle, nonlinear processing, called regularization, of the updated image is performed to ensure the convergence and to selectively reduce image noise in more homogeneous areas. After the regularization, the cycle is repeated until reaching a threshold value. Two major advantages of applying IR techniques are noise reduction and artifact reduction. By product of filtering, the lower image noise allows for dose reduction to patient. However, while traditional IR is a very robust technique, it is also impractical for clinical scenarios due to high computational hardware and processing time requirements for raw data reconstruction loops. Therefore, an alternative to traditional IR is very desirable.

1.4 CT artifacts

The artifacts are discrepancies between the CT numbers represented in the image and the expected ones based on the linear attenuation coefficients of the test object. They can deeply degrade the quality of the images, to the point to make them useless for clinical and diagnostic purposes. The fact that these effects are more prominent on CT images than on conventional radiographs is due to the nature of computed tomography, that requires the reconstruction from more than one million independent detector measurements.

The appearance of artifacts can be really diversified: streaking, generally due to an inconsistency in a single measurement; shading, typically related to a group of channels or views deviating gradually from the true

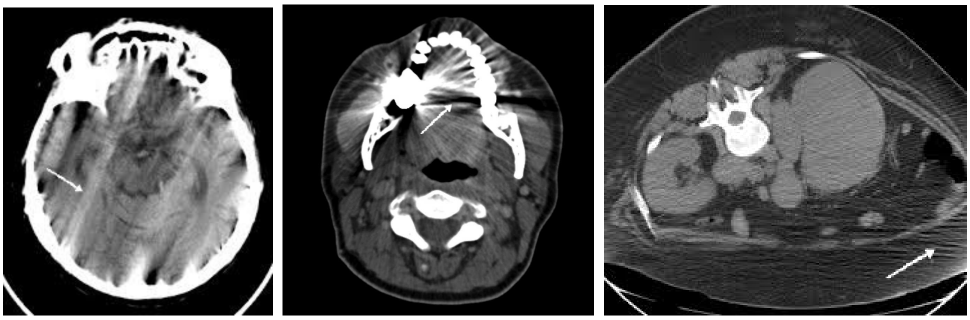

(a) (b) (c)

Figure 2.2: Examples of patient-based CT artifacts: (a) motion artifact on a CT image of a head [Boas and Fleischmann, 2012]; (b) metal artifact caused by dental fillings [www.healthcare.siemens.com]; (c) CT image of the body obtained with the arms of the patient outside the scanned FOV [Boas and Fleischmann, 2012].

measurement; rings, which are caused by errors in an individual detector calibration; and distortion, which is connected to helical reconstruction [Barrett and Keat, 2004].

For what concerns the origin, they can be classified in patient-based, physics-based and scanner-based artifacts. In many instances, careful patient positioning and optimum selection of scanning parameters are helpful factors in avoiding CT artifacts, especially if combined with specific algorithms for artifacts removal.

Patient-based artifacts

Patient-based artifacts are caused mainly by motion, presence of metallic implants and incomplete projections.

Motion (patient, cardiac, respiratory, bowel) causes "ghosting" effect objects and the CT image appears as if composed of superimposed images (Figure 2.2/a). Lower times of image acquisition, reachable using for example shorter rotation time (as 0.28 s) or higher current of the X-ray tube, help in reducing motion artifact, thanks to the fact that the patient has less time to move during the acquisition.

Metal implants in the scan field can lead to severe streaking artifacts (Figure 2.2/b). The cause is that the density of the metal is beyond the normal range that can be handled by the computer, namely its HU is saturated to the maximum value, resulting in incomplete attenuation profiles [Barrett and Keat, 2004]. In fact, metal artifacts are particularly pronounced with high atomic number metals such as iron or platinum, and less pronounced with low atomic number metals such as titanium. Additional artifacts due to beam hardening, partial volume and aliasing are likely to compound the problem when scanning very dense objects.

If any portion of the patient lies outside the scanned field of view, the collected projections will bring incomplete information about this portion and streaking or shading artifacts will be generated (Figure 2.2/c). Most critical directions are anterior-posterior and lateral. To avoid this type of artifact, scanners designed specifically for radiation therapy planning have wider borders and larger scan fields of view than standard scanners and permit greater versatility in positioning, independently on the size of the patient.

Physical-based artifacts

Physics-based artifacts result from the physical processes involved in the acquisition of CT data and can be classified in beam hardening, partial volume, photon starvation and under-sampling.

As known, the X-ray beam is polychromatic, so composed by photons belonging to a range of energies. Passing through the patient the less energetic photons are easily absorbed and in this way the beam becomes harder, namely its mean energy increases. The effects of the beam hardening are different for homogeneous and heterogeneous materials. For the first ones cupping artifacts are created (Figure 2.3/a), while for the second ones dark bands or streaks between dense objects appears (Figure 2.3/b).

Partial volume effect, instead, occurs either when the object is partially out of the scan plane or when the object size is smaller than the spatial resolution of the scanner. It is strictly related to the necessary averaging of the attenuation properties of the different materials each voxel consists of. This implies blurred boundaries to some extent, due to the not correct determination of the CT number (Figure 2.3/c).

Photon starvation can occur in highly attenuating areas, such as the shoulders (Figure 2.3/d). In fact, when the X-ray beam's direction is horizontal, the attenuation is so high that an insufficient number of photons reach the detectors, resulting in very noisy projections at these tube angles. The reconstruction process magnifies this noise, producing horizontal streaks in the image. An increased tube current could fix this problem, however the patient would receive an higher dose during the scanning. Therefore, to minimize photon starvation, most manufacturer use either automatic tube current modulation or adaptive filtration.

Under-sampling implies misregistration of the collected data, that can cause two different types of artifacts: “view aliasing” if the projections are too

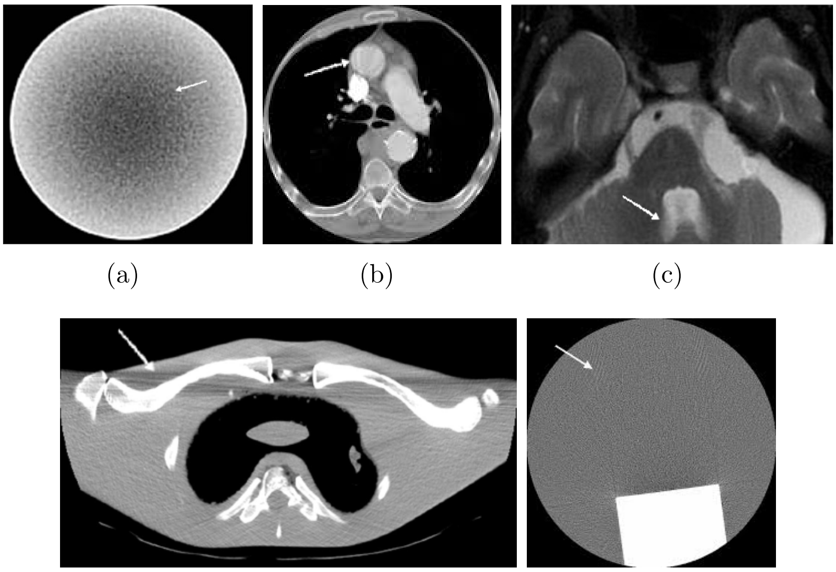

(a) (b) (c)

(d) (e)

Figure 2.3: Examples of physical-based CT artifacts: (a) cupping artifacts due to beam hardening [Yi, 2013]; (b) streaking artifacts due to beam hardening [http://slideplayer.com/slide/4563805/]; (c) partial volume effect on 5-mm-thick [http://mri-q.com/partial-volume-effects.html]; (d) streaking artifacts due to photon starvation in the shoulders [Barrett and Keat, 2004]; (e) aliasing caused by under-sampling at the edge of a Teflon block in a water phantom [Barrett and Keat, 2004].

separated from each other and "ray aliasing" if the under-sampling is within the projection itself. In the first case fine stripes appear to be radiating from the edge of, but at a distance from, a dense structure (Figure 2.3/e), while in the latter case the stripes appear close to the structure itself.

Scanner-based artifacts

Scanner-based artifacts are either caused by problems with the detector or related to the process of acquisition.

Miscalibrated or defective detector elements are a relevant source of artifact. The principal consequences that they can create are bright or dark rings centered on the center of rotation, the so called ring artifacts (Figure 2.4/a). Such effect can sometimes simulate pathology. Usually, recalibrating the detector is sufficient to fix this artifact, although occasionally it needs to be completely replaced [Boas and Fleischmann, 2012].

Multi-slice helical CT-systems suffer from windmill artifacts: black/white

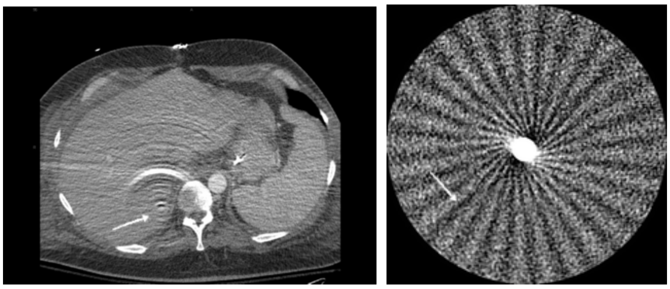
(a) (b)

Figure 2.4: Example of scanner-based CT artifacts: (a) ring artifacts inside the abdomen [http://www.upstate.edu/radiology/education/rsna/ct/artifact.php] and (b) CT image of an acrylic sphere showing windmill artifact [Barrett and Keat, 2004].

patterns that spin off of features with high longitudinal gradients (Figure 2.4/b). They are due to the fact that several rows of detectors intersect the plane of reconstruction during the course of each rotation. As the pitch increases, the number of detector rows intersecting the image plane per rotation increases and the number of "vanes" in the windmill artifact is higher.

2 CT imaging for treatment planning

Before treating the patient, the so called planning CT is acquired. On that single energy CT particular volumes are delineated and the proton treatment plan is calculated using a specific calibration curve necessary for the conversion from CT number to relative proton stopping power.

The choice of developing CT-based radiation treatment planning is quite natural, due to the related 3D information about both tumor location and electron density distribution. In particular, the knowledge of this latter quantity makes the CT a requirement for treatment planning in proton therapy, since it is central for dose and range calculations (Equation 1.4) Modern types of imaging entered the proton treatment planning scene only some years later. Magnetic Resonance Imaging (MRI) plays an important and still increasing role, since it gives further details with respect to the geographical relationship between tumor and normal tissues, with much higher spatial and contrast resolution than CT. Different MRI acquisition techniques are available, which allow better differentiation between malignant and healthy soft tissue than with CT. The outcome continuous 3D data set can be reformatted in any plane and co-registered or fused with the planning CT data set. Examples of proton treatment protocols where MRI is routinely used for planning volume definition include high-grade gliomas and brain metastases. Positron Emission Tomography (PET) and Single Photon Emission Computed Tomography (SPECT) are the latest additions to imaging technology supporting the definition of planning volumes for proton therapy. They added another dimension to the ability to see tumors and to distinguish them from normal tissue, based on differential metabolism. F-18 fluoro-deoxyglucose (FDG) is the most commonly used tracer in oncological imaging, thanks to the increased glucose metabolism of tumor cells. It can be particularly useful for lung cancer, allowing the distinction between tumor and scar or atelectatic lung tissue and the exclusion of advanced stages with multiple positive mediastinal lymph nodes [Schulte, 2007].

2.1 Target volumes definition

Accurate delineation of target volumes and critical anatomic structures is essential for planning and delivery of high-precision radiation therapy. Once the planning volumes have been outlined, proton treatment beams are selected and their dose distributions are calculated and optimized. As introduced in [ICRU, 1993], [ICRU, 1999], [ICRU, 2004] and [ICRU, 2007], several volumes related to both tumor and normal tissues must be defined before the treatment (Figure 2.5):

- Gross Tumor Volume (GTV);
- Clinical Target Volume (CTV);
- Internal Target Volume (ITV);
- Planning Target Volume (PTV);
- Organ At Risk (OAR);
- Planning organ-at-Risk Volume (PRV);
- Treated Volume (TV);
- Irradiated Volume (IV);
- Remaining Volume at Risk (RVR).

The GTV is defined as the gross palpable, visible, or clinically demonstrable location and extent of the malignant growth. However, the GTV alone generally does not cover the whole extent of tumor spread. For this reason, a CTV is defined as tissue volume that contains the GTV and/or sub-clinical malignant disease that must be eliminated. CTV is therefore the volume of tumor that must be irradiated with an appropriate dose in order to achieve tumor control. ITV instead is an expansion of CTV to account for tumor motion both intra- and inter-fraction. The final volume specified by ICRU is

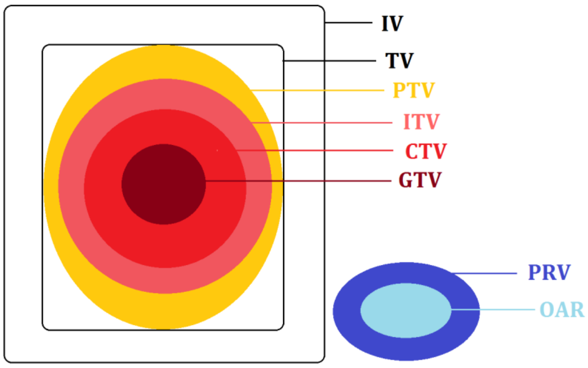

Figure 2.5: Illustration of volumes defined for treatment planning, in order to deliver the correct dose to the tumor, while sparing the normal tissues.

PTV, that is the ITV plus a set-up margin which accounts for uncertainties in patient positioning and alignment of the therapeutic beams during the treatment planning and through all treatment sessions.

In addition to these tumor related volumes, OARs are those organs that might be seriously affected by the radiation, either because of proximity to target or because of their inherent sensitivity. In order to spare these organs with an high probability, the OAR can be extended to PRV, adding an integrated set-up margin, as done for the PTV.

TV is the volume that receives a dose that is considered important for local cure or palliation, while IV is the tissue that receives a dose that is considered significant in relation to normal tissue tolerance. Moreover, the volume that is within the imaged region of the patient but outside all delineated OARs and CTVs is identified as RVR. The dose at RVR shall also be reported, in particular to estimate the risk of late side effects.

In conclusion, the goal of treatment planning is the evaluation of the parameters of the delivering system in order to give the prescribed dose to the PTV, while limiting the dose inside the PRV within certain limits.

2.2 CT number to RPSP conversion

In order to do the treatment plan on the planning CT of the patient, the HU value of each voxel must be converted, for proton therapy, to the associated relative proton stopping power, or electron density in case of photon therapy. The two main approaches to achieve this goal are tissue substitute and stoichiometric calibrations (Figure 2.6).

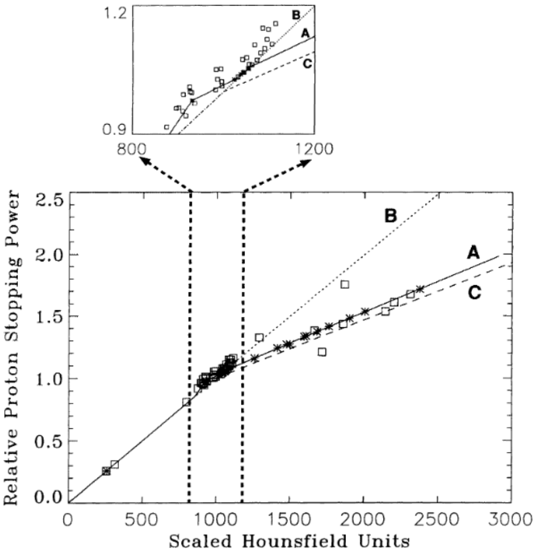

Figure 2.6: Calibration curves for the transformation of HU values into RPSP. The solid line shows the stoichiometric calibration (A) for biological tissues, while the dotted (B) and dashed (C) ones are the tissue substitute calibration using different substitutes. Calculated RPSP of some tissue substitutes (squares) and real tissues (stars) are plotted against the scaled HU values (HU values + 1000) [Schneider et al, 1996].

Tissue substitute calibration

The tissue substitute calibration is the first method proposed to relate CT number and RPSP [Chen et al, 1979], [Mustafa and Jackson, 1983]. It is an empiric method where HU values of tissue-equivalent samples with known compositions are measured with a specific CT protocol. The calibration curve is than defined as the linear fit of measured HUs to the related RPSPs, evaluated using the Equations 1.4 and 1.5. In its most simplified version, the curve consists of two linear segments, thus taking into account the dependency of photoelectric effect on the atomic number. One segment covers CT numbers up to 0 HU considering mixture of air and water, while the other one starts at 0 HU and describes mixture of bone substitutes and water. However, in Figure 2.6, it can easily be seen that the tissue substitute data varies substantially, hence the reliability of this calibration method is strongly affected by the choice of the tissue surrogates. The use of different tissue substitutes can lead to different calibration curves, therefore their chemical compositions must be equivalent to that of real tissues and known with a good accuracy.

Stoichiometric calibration

This method is currently the most used for CT-based treatment planning in particle therapy. It has been proposed to overcome the limitation given by the chemical composition of tissue surrogates, improving in this way the performance of the calibration for biological tissues [Schneider et al, 1996]. This method is also based on the measure of the tissue substitutes' CT numbers, but in this case the materials can be chosen arbitrary, on condition that their elemental composition is known. Taking into account Equation 2.2, the information related to these probes are then inserted in the following parametrized equation for the linear attenuation coefficient:

$$\mu = \rho_e \cdot \left(K^{photo} \sum_i \frac{\lambda_i Z_i^{3.62}}{\Lambda} + K^{cohe} \sum_i \frac{\lambda_i Z_i^{1.86}}{\Lambda} + K^{KN} \right) \tag{2.10}$$

where $\lambda_i = \omega_i \frac{Z_i}{A_i}$ and $\Lambda = \sum_i \lambda_i$. In this way, it is possible to extract K^{photo}, K^{cohe} and K^{KN}, that are respectively constants related to the cross sections of photoelectric effect, coherent scattering and Compton effect (Part I - 2.1.1). Thanks to these parameters, the CT numbers of selected ICRP tissues can be calculated using once again Equations 2.2 and 2.10, while the related proton stopping power values can be evaluated with Equations 1.4 and 1.5. Finally, fitting these CT number-RSPR pairs, the calibration curve is obtained. This curve is composed by the combination of three linear fits: between 0 HU and 850 HU (lung), in the range of 1023 HU - 1060 HU (various soft tissues) and for values greater than 1060 HU (bone tissues). To take into account also the adipose tissue, the lung fit is linearly connected with the fat data point (from 850 HU to 930 HU) and this latter one with the organ fit (from 930 HU to 1023 HU).

3 Dual Energy CT

In the single energy X-ray computed tomography, the differentiation and classification of different tissue types and contrast agents can be extremely challenging. In fact, the measured CT number of a voxel is related to its linear attenuation coefficient, which is not unique for any given material, but is a function of multiple parameters: composition, mass density and energies of photons interacting with the material. For this reason, same linear attenuation coefficient values can be measured for different materials at a given energy, depending on the mass density [McCollough et al, 2015].

On the contrary, in dual-energy CT, an additional attenuation measurement is obtained using a second X-ray spectrum, allowing the differentiation of multiple materials. The idea to scan an object with two different photon spectra, in order to obtain information from both energies, was already formulated at the time of the CT invention [Hounsfield, 1973], [Rutherford et al, 1976], [Alvarez and Macovski, 1976].

3.1 Technical approaches

At present, the main approaches to DECT are the following: sequential acquisition, rapid voltage switching, dual-source CT, layer detectors and quantum-counting detectors. Only the first three are commercially available, while the latter two are currently in development [Johnson, 2012].

Sequential acquisition

Sequential acquisition is the oldest and technically easiest implementation of DECT imaging. It can be achieved in two different ways. The first one implies two temporally sequential scans of the entire scan volume to acquire the data at each of the two tube potentials (Figure 2.7/a-I). Scans can be acquired in axial or spiral modes. Because the data are not acquired simultaneously, this technique is really sensitive to patient motion between both image acquisitions. The second approach instead implies switching the tube potential between each couch position, thus minimizing the time delay with consecutive scans of one anatomic section (Figure 2.7/a-II) [Johnson et al, 2011].

Rapid voltage switching

In rapid voltage switching systems a single source scanner alternates the X-ray tube potential rapidly between low and high kV during tube rotation (Figure 2.7/b). Data are collected twice for every projection or, in practice, for immediately adjacent projections. For this reason, the method allows spatial overlap of both acquired raw data sets. However, the rotation time usually must be around 0.5 s or longer, in order to take into account the time for the additional acquisition and for the voltage modulation. Furthermore, the tube current could not be increased quickly enough for the low tube potential measurements to achieve comparable noise and dose levels in both low and high tube potential data sets. In fact, the adaptation of the current to the related voltage, in order to achieve a similar output of photons at both energies, is technically challenging. The main reason is that the free electrons of the cathode do not become available rapidly enough to accommodate such fast changes. To deal with that, another possible approach is to acquire two low-voltage projections for each single high-voltage projection so

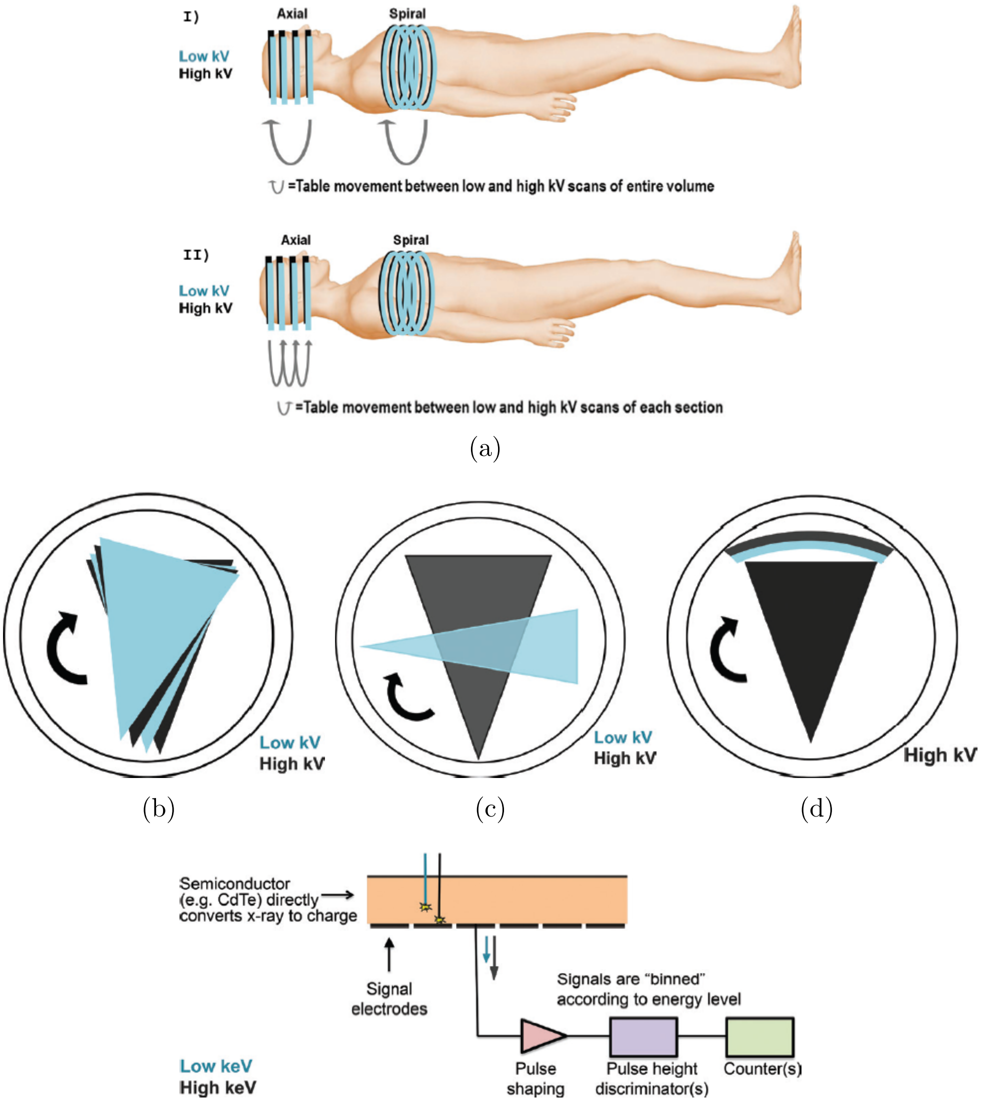

(a)

(b) (c) (d)

(e)

Figure 2.7: Schematic illustrations of technical approaches for acquiring Dual-Energy data set: sequential acquisition (a), rapid voltage switching (b), dual-source CT (c), layer detectors (d), and quantum-counting detectors (e). Images from [McCollough et al, 2015].

that the number of photons available at the two energy levels are balanced. In any case, due to its basic principle, rapid voltage switching remains limited by the spectral resolution and the additional dose, because other dose reduction features (i.e., tube current modulation or optimized filtration of each spectrum) are not possible [Johnson et al, 2011].

Dual-source CT

Dual-source CT systems use two tubes running at different voltages and corresponding detectors mounted orthogonally in one gantry (Figure 2.7/c). The twofold investments in hardware implies significant advantages: voltage, current and filter can be chosen independently for both tubes to achieve an optimal spectral contrast with sufficient transmission and the least overlap, data are acquired simultaneously by both systems and there is no temporal offset in data acquisition. Nevertheless, to preserve compact system geometry inside the same gantry, in some systems, one of the detectors is smaller, and can therefore reach a maximum FOV of 33x33 cm, versus the typical 50x50 cm. While for diagnostic this FOV is sufficient to cover all the vessels and organs in most patients and the eventual adipose tissue of obese patients outside the field is generally not of clinical relevance, this can be a limitation for radiotherapy. Proton therapy is very sensitive to this, as the knowledge of the entire body around the treatment area is essential for the accuracy of the treatment plan. An additional limitation is the scattered-radiation induced on the first detector from the second tube and vice versa, which is hardly removable by anti-scatter grids. Therefore, dedicated scattered-radiation correction algorithms are employed, in order to prevent image degradation and to restore image contrast [Petersilka et al, 2008].

Layer detectors

Standard CT detectors are energy integrating, so they convert photon quanta into an electrical signal independent from photon energy. Another approach for acquiring dual-energy CT projections data is the usage of a single high tube potential beam and an energy-resolving detector (Figure 2.7/d), composed by two layers made with different scintillator materials, to allow for different sensitivity profiles. The low-energy data from the polychromatic spectrum of the tube are collected from the innermost detector layer and the high-energy data are collected from the outermost detector layer. To achieve comparable noise in the low and high energy images, different detector thicknesses are used. The method is currently tested in a prototype scanner of Philips Medical Systems [McCollough et al, 2015].

Quantum-counting detectors

Quantum-counting detectors, also called photon-counting, can resolve photon energies. Possible applications include extended tissue characterization and dose saving. The process can be summarized as follows (Figure 2.7/e). The semiconductor detector (i.e., CdZnTe) directly converts the absorbed X-ray energy into electrical charge, which is then collected by discrete signal electrodes. The collected signal is proportional to the absorbed photon energy. Pulse height analysis is used to bin the signal from discrete photon interactions into two or more energy windows, depending on the capability of the application-specific integrated circuit coupled to the semiconductor detector. Energy resolving demands an extremely high time resolution with fast rather quick saturation of the detector material, resulting in a rapid drift of the measured signal. Tube currents and tube rotations must be lowered and longer scan times are expected. Therefore, these detectors are currently used for scanning small animals [Cormode et al, 2010] but, for now, they can't manage photon flux used in clinical CT [Kappler et al, 2011].

3.2 Potential of spectral information

In contrast to SECT, where a single CT number is determined as combination of the electron density ρ_e and atomic number Z, the DECT allows to separate both quantities. Obviously, the least the photon spectra are overlapped, the more meaningful is the information from DECT imaging.

Post-processing of the DECT data is possible either in the projection space or in the image space. Algorithms based on the projection space have the advantage of being free from beam hardening and other image artifacts but require the geometrical overlap of both projections. Instead, image space post-processing algorithms can achieve comparable good results when precise beam hardening corrections are applied.

There are two possibilities to separate the DECT information. The first one uses the separation of Compton and photoelectric contributions to photon attenuation (Part I - 2.1.1, [Alvarez and Macovski, 1976]):

$$\mu(E_i) = a_1 \cdot \rho_e \cdot \sigma_e^{KN}(E_i) + a_2 \cdot \rho_e \cdot \frac{Z^n}{E_i^3}; \quad n \sim 3 \tag{2.11}$$

where a_1 and a_2 are constants. The second method is based on a virtual decomposition of each voxel into two base materials present in fractions w_1 and w_2, with photon mass attenuation coefficients μ_1/ρ_1 and μ_2/ρ_2

[Goodsitt et al, 2011]:

$$\mu(E_i) = w_1 \cdot \frac{\mu_1(E_i)}{\rho_1} + w_2 \cdot \frac{\mu_2(E_i)}{\rho_2}. \tag{2.12}$$

Potential applications of such methods include the quantification of iodine and calcium content, the chemical differentiation of kidney stones in uric acid and calcified ones, the differentiation of inactive brain hemorrhage to fresh bleeding and the diagnosis of gout [Aran et al, 2014].

The implementation of DECT in the context of oncological imaging is still a challenging area. However, recent study showed clear advantages of DECT in tumor detection and lesion characterization within the chest and abdominal region as well as the genitourinary system. [Simons et al, 2014].

The application of DECT more attractive for proton therapy is the prediction of the stopping power ratios by using the electron density ρ_e and effective atomic number (average atomic number for a compound or mixture of materials) Z_{eff} information. In fact, an important component of proton therapy margin recipes is the uncertainty attributed to the conversion of HU values to RPSP. This uncertainty has been quoted as 3.5% of the proton range [Yang et al, 2012] and is related to the lack of one-to-one correspondence of photon attenuation coefficients with proton stopping power. DECT has been recently proposed as an attractive approach to reduce stopping power estimation errors [Yang et al, 2010]. Different techniques for extract these quantities from two CT values acquired at different energies have been proposed in literature [Rutherford et al, 1976], [Bazalova et al, 2008], [Landry et al, 2011], [Saito, 2012], [Landry et al, 2013]. Phantom experiments have shown that the method can yield stopping power with an accuracy of 1-2% [Hünemohr et al, 2013], [Bourque et al, 2014], [Farace, 2014], [Hünemohr et al, 2014a], [Hansen et al, 2015]. Recently, comparison of proton therapy treatment planning on the basis of DECT and SECT for base of skull tumors with surrogate patients showed relative range differences of -1,4% [Hudobivnik et al, 2016].

4 Examples of imaging systems

Examples of CT imaging systems are SOMATOM Sensation Open at CPT in PSI and SOMATOM Definition Flash at Kantonsspital Baden (KSB). These machines are the ones used for data acquisition in this project.

Figure 2.8: SIEMENS SOMATOM Sensation Open at PSI.

4.1 SOMATOM Sensation Open

The SOMATOM Sensation Open is the in-room sliding CT scanner of Gantry 2, at PSI (Figure 2.8). It is a Single Source CT scanner, with an ergonomic enlarged gantry opening and a scan plane located 35 cm from the gantry front.

This CT-system is equipped with the 0 MHU STRATON X-ray tube. The direct contact of the cathode with cooling oil implies for this newly developed X-ray tube a significantly reduced cooling time for shorter interscan delays and increased power reserves. The electron beam of the tube is deflected, creating two precise focal spots. In this way, the projections that reach each element of the detector are doubled, resulting in an oversampling in the axial direction. Thanks to this duplicated sampling, the slice width can be reduced and the windmill artifacts are almost completely removed. In order to read-out both projections for each detector element, high speed Ultra Fast Ceramic (UFC) detectors are used [Dehm and Reinsberger, 2012].

The z-coverage per rotation is given by the product of the number of active detector slices with the collimation, where this latter one is the slice thickness resulting from the effect of the tube-side collimator and the adaptive detector array design. For example, the common z-coverages for SOMATOM Sensation Open CT-system are 20 x 0.6 mm or 20 x 1.2 mm.

Four different voltage settings are available in this CT scanner: 80 kVp, 100 kVp, 120 kVp and 140 kVp. There are also four different types of kernels. They are indicated with a capital letter, a number and either *s* or *f*. The capital letter stands for the type of kernel: *H* for head, *B* for body, *C* for child's head and *S* for special application, as osteo CT. The number

Figure 2.9: SIEMENS SOMATOM Definition Flash at KSB.

that follows one of these four capital letters defines the image sharpness: the higher the number, the sharper the image and the lower the number, the smoother the image. The endings *s* or *f* depend on the rotation time, respectively slow and fast, which in the latter case is about double fast then the first one (1 s and 0.5 s generally). Usually at PSI, for proton therapy applications, kernel *B30s*, with intermediate image sharpness, is used. The underlying reason is that this kernel offers the better trade-off between the calibration curves of head and body. In fact, with *B30s* the difference among the two curves at HU 1000 is less than 3%.

CARE Dose 4D is a fully automated technique that permits to achieve minimal dose to the patient, together with a maximum quality of the image. The principle underlying the CARE Dose 4D is a current modulation of the X-ray tube in the angular and longitudinal directions, in order to adapt to different anatomical regions and patient sizes. For optimal effect, two topograms of the patient must be acquired, since the software will use it to determine the required current for each projection of the entire scan. The topogram is either anterior-posterior or lateral scan, where the tube is in a fixed position and the gantry translates along the couch as X-rays are delivered. The image appears similar to a radiograph.

4.2 SOMATOM Definition Flash

The SOMATOM Definition Flash is the Dual Source CT scanner of the radiology department in Kantonsspital Baden (Figure 2.9).

The combination of two sources, a high table feed, ultra-fast data transmission and a gantry that can perform a full rotation in 0.28 s make the SOMATOM Definition Flash truly unrivaled in terms of scanning speed. Its temporal resolution is 75 ms, so heart-rate independent. The X-rays generated by the SOMATOM Definition Flash's two tubes are captured by two Stellar detectors, each of them made by 128 slices. These high-end detectors with miniaturized electronic components generate ultra-thin slices with a very high spatial resolution. The z-coverage of this system is for that 128 x 0.6 mm.

The voltages can be set between 80 kVp and 140 kVp, in steps of 20 kV. Additionally, a tin filter (selective photon shield) on 140 kVp can be used to increase the spectral separation between low and high energy spectrum, while narrowing the 140 kVp spectrum. This prevents unnecessary exposure and ensures less beam-hardening artifacts [Johnson et al, 2011]. Other dose-reduction solutions, like CARE Dose 4D, further contribute to dose efficiency.

Two important algorithms are available on SOMATOM Definition Flash. The first one is SAFIRE, an alternative method for iterative image reconstruction from acquired raw-data. That possibility broadens the number of kernels, in this case identified with *I* as capital letter. Moreover, iMAR algorithm can be set in order to minimize metal artifacts, such as the ones caused by surgical, prosthetic and dental fillings, as well as pacemakers. Both these algorithms will be explained in detail in Part II - 4.2.2.

Part II

Experimental Work

Chapter 3

Contrast Enhancement

> *"Nature is often hidden,*
> *sometimes overcome,*
> *seldom extinguished."*
> - Francis Bacon -

The focus of this study is to develop an algorithm in MATLAB capable of creating tumor-canceled and bone-canceled images, by making use of Dual Energy X-ray imaging, for improving patient positioning.

1 Introduction

In proton therapy, the correct positioning of the patient is vital to ensure safe dose delivery to the target while sparing OAR.

At PSI, before each fraction, patient position is corrected by comparing daily lateral and anterior-posterior topograms with reference ones acquired together with planning CT. The couch corrections to compensate for mismatch are computed in the Patient Position Verification (PPV) software, comparing manually identified features on both image sets. However, inserting the control points in the correct position is not always straight-forward, in particular if the target moves due to the breathing, as in case of thoracic cancers.

Positioning could prove easier and more successful when bone and tumor structures are analyzed separately. DE X-ray imaging is capable of creating bone- or tumor-only images from a pair of images acquired at different energies exploiting the dependence of Compton and photoelectric effects on energy and type of material [Brody et al, 1981]. In fact, at low energies, indicatively lower than 90 kVp, the photoelectric effect is more prominent than the Compton one, that domains at higher energies, usually greater than 120 kVp. For high density materials, like bone, the major effect is the photoelectric, due to its dependence with the fourth power of the atomic number, while in less dense materials the Compton effect is dominant thanks to its dependence with the electron density. These considerations explain the different contrast that images of the same part of the body exhibit at different acquisition energies.

2 Materials and Methods

2.1 Considered approach

The analyzed methods for obtaining bone-canceled and tumor-canceled images from the ones acquired at low and high energies are weighted logarithmic subtraction [Brody et al, 1981], [Hoggarth et al, 2013], [Huo et al, 2014] and its linear simplification. In both cases a mono-energetic X-ray beam and absence of scattering are assumed. This leads to the Lambert-Beer relations:

$$I_L = I_{0L}\, e^{-\mu_{bL}x_b-\mu_{tL}x_t} \tag{3.1}$$

$$I_H = I_{0H}\, e^{-\mu_{bH}x_b-\mu_{tH}x_t} \tag{3.2}$$

where I_{0L} and I_{0H} are the initial intensities for low and high energy X-ray beams, I_L and I_H the final intensities, $\mu_{t(L/H)}$ and $\mu_{b(L/H)}$ the energy dependant linear attenuation coefficients of tumor and bone regions respectively, while x_t and x_b are the thicknesses of tumor and bone structures along the pathway of the radiation. The Low-Energy (LE) and the High-Energy (HE) images can be expressed, except for a proportional constant, as:

$$ln(I_L) \simeq -\mu_{bL}x_b - \mu_{tL}x_t \tag{3.3}$$

$$ln(I_H) \simeq -\mu_{bH}x_b - \mu_{tH}x_t\ . \tag{3.4}$$

In the logarithmic method, bone-canceled I_{BC} and tumor-canceled I_{TC} images are constructed as linear combination of the logarithms of I_L and I_H:

$$I_{BC} \simeq ln(I_H) - w_t ln(I_L) \tag{3.5}$$

$$I_{TC} \simeq -ln(I_H) - w_b ln(I_L) \tag{3.6}$$

with weighting coefficients that satisfy $w_t = \frac{\mu_{bH}}{\mu_{bL}}$, $w_b = -\frac{\mu_{tH}}{\mu_{tL}}$. In the linear method, instead, a linear combination of the original images is used:

$$I_{BCorTC} \simeq k_l I_L + k_h I_H \tag{3.7}$$

where the weighting coefficients satisfy $\frac{k_h}{k_l} = -\frac{\mu_{bL}}{\mu_{bH}}$ for the bone-canceled image and $\frac{k_h}{k_l} = -\frac{\mu_{tL}}{\mu_{tH}}$ for the tumor-canceled one. Due to the underlying

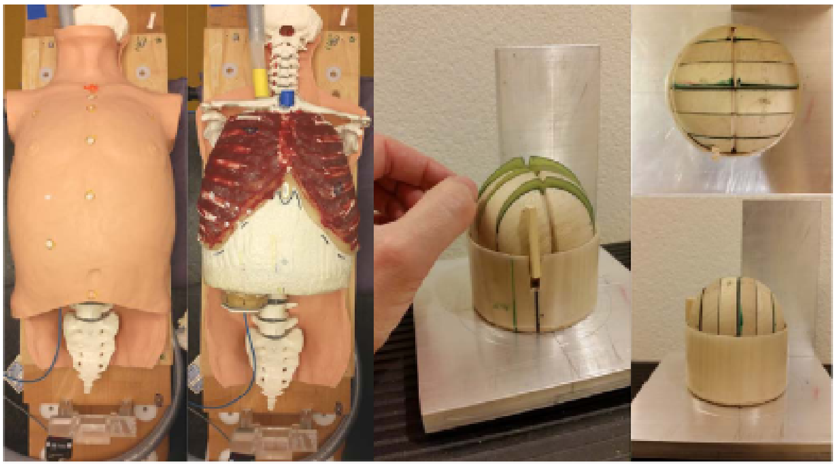

Figure 3.1: LuCa phantom with and without skin, revealing the ribs and lung compartment. Wood tumor sphere cut into 5 pieces to insert film for dosimetric measurements and mounted on a set-up tool with a vertical slab to enable alignment of the films to the coronal or sagittal plane of the phantom.

theory, this method of contrast enhancement based on DECT can be applied to 2D images only. In fact the basic assumption is that each pixel can be seen as result of the contributions from each material crossed by the beam, as in Equations (3.1), (3.2).

2.2 Phantom

The phantom used for this study is the anthropomorphic thorax phantom LuCa (Figure 3.1). It is a breathing phantom of the thorax, mainly used for testing new motion mitigation techniques for pencil beam scanning proton therapy [Perrin et al, 2015]. It consists of inflatable and deformable lungs surrounded by a skeleton, inter-skeletal muscle and two different skins mimicking either female or male patients. In addition, there is silicon heart and a mobile tumor, made of wood or silicon, in which radiochromic films can be inserted. Motion of the tumor and deformation of the thorax is controlled via a custom made pump system driving air in and out of the lungs. All components of the phantom are metal-free and ensure CT and MRI compatibility.

2.3 Generation of DE positioning images

All the images have been acquired with Siemens SOMATOM Sensation Open CT scanner of CPT, at PSI. Since at PSI positioning is performed using

Combination	**LE**	**HE**
1	80 kVp - 50 mAs	120 kVp - 35 mAs
2	80 kVp - 50 mAs	140 kVp - 38 mAs
3	80 kVp - 50 mAs	140 kVp - 100 mAs
4	80 kVp - 90 mAs	140 kVp - 28 mAs

Table 3.1: Low/High energies combinations investigated for contrast enhancement DECT algorithm.

topograms, both lateral and anterior-posterior DE topograms have been acquired. The anthropomorphic phantom was scanned with both tumors, in wood and silicon.

The first analysis done on the acquired images is the comparison between logarithmic and linear methods and between the different LE/HE combinations. The latter test is very important to be done on each system of image acquisition, in order to characterize it individually. In fact, the features of the CT scanner, like type of detector and source-detector distance, can influence the performance of the algorithm. For this reason the optimal combination of energies for DE might differ from one system to another. To find the optimal LE/HE combination for the creation of bone-canceled and tumor-canceled images, several combinations have been investigated (Table 3.1). The choice is based on the ones used by [Johnson et al, 2007], and on the combinations available on SOMATOM Sensation Open.

In practice, for each of the chosen materials, three ROIs (Regions Of Interest) are selected in order to improve the statistic related to the mean values, essential for the proper functioning of the algorithm. In this work three materials were considered (Figure 3.2): tumor, bone and background (soft tissue surrounding bone and tumor regions). Subsequently, the relevance of the selected materials' regions of interest for the creation of final images has been analyzed. For this reason the script has been slightly modified, in order to maintain fixed the ROIs associated to two materials and choose differently the ones belonging to the other tissue. The process has been repeated for each of the three cases.

To obtain bone- and tumor-canceled images, the weighting coefficients are chosen minimizing the difference between the mean values of the bone and the background ROIs and between the tumor and background ROIs respectively. The weighting coefficients are determined making use of an iterative process: for the logarithmic method both w_b and w_t are varied from -10 to +10, while for the linear one a value of 0.21 is given to k_h (linear

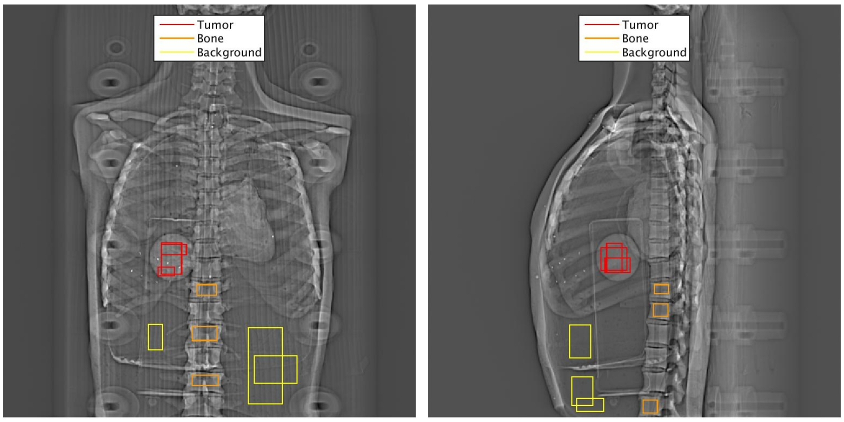

Figure 3.2: Example of ROIs' choice, for silicon tumor. Three regions of interest are chosen for each material: tumor, bone and background (soft tissue surrounding bone and tumor regions).

attenuation coefficient associated to the bone at 120 kVp) and than k_l is varied from 0 to 0.4. However, as it can be seen in Figure 3.3, these ranges are too large respect to the real values that minimize the contrast and for this reason they have been modified in a second step optimization. In the logarithmic method the coefficients are then varied from -3 to +3 in steps of 0.006 and in the linear one k_l is varied from 0.1 to 0.3 in steps of 0.0002. In this way a total of 1001 values is covered for the search of the optimal weighting coefficient.

To objectively assess the four obtained images, we evaluated image quality on the ROIs of the material under consideration with respect to the background. The metrics used are relative contrast C_r, relative noise σ_r and Signal Difference to Noise Ratio $SDNR$ (called also CNR, Contrast to Noise Ratio), defined as follows:

$$C_r = 2\,\frac{\mu_1 - \mu_2}{\mu_1 + \mu_2} \tag{3.8}$$

$$N_r = \frac{\sigma_1 + \sigma_2}{\mu_1 + \mu_2} \tag{3.9}$$

$$SDNR = C_r/N_r \tag{3.10}$$

where μ and σ are respectively the mean of the mean values and of the standard deviations related to the ROIs. The errors associated to C_r, N_r and $SDNR$ are evaluated applying error propagation on the uncertainties arising from the maximum semi-dispersion of mean values and of standard deviations.

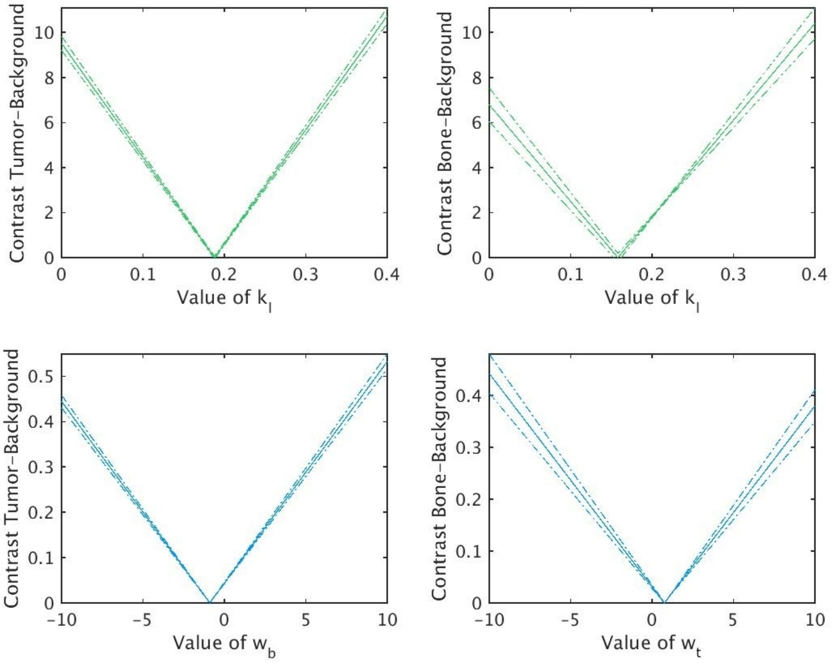

Figure 3.3: Example of trend of the difference between the materials in consideration for creating the bone-canceled and tumor-canceled images with the related weighting coefficients. The straight line represents the mean contrast of the ROIs and the dotted lines are the margins obtained adding the associated error. In green (upper part) graphs concerning the linear method are represented, while in blue (lower part) those for the logarithmic approach.

2.4 Experiments

The performance of bone- and tumor-canceled images for patient positioning was compared to standard single energy topograms when known shifts were applied to test object respect to its reference position (Table 3.2).

The shifts were calculated with two different methods: segmentation of the tumor in bone-canceled images and by matching of manually selected corresponding points on all images (mono-energetic, bone-canceled and tumor-canceled) in the clinically used Patient Position Verification (PPV) software. The segmentation of the tumor has been performed on bone-canceled images only, since in the mono-energetic case it is underneath the ribcage and thus the algorithm is not achieving the right goal.

Segmentation

For each position, both LAT and AP bone-canceled topograms has been segmented with the aim of determining the tumor's centroid. A region growing

Number of the shift	Δx (cm)	Δy (cm)	Δz (cm)
1	0.50	0.00	0.00
2	0.00	2.00	0.00
3	0.00	0.00	1.50
4	-0.50	-1.50	1.00
5	-0.05	0.00	0.00
6	0.00	0.05	0.00
7	0.00	0.00	-0.05
8	0.55	1.51	-1.09
9	-1.16	-1.17	1.18

Table 3.2: Shifts imposed to the couch in order to test the performance of bone- and tumor-canceled images for patient positioning compared to standard single energy topograms.

method is applied, in order to find the pixel belonging to the malignancy. The implemented method requires the delineation of two ROIs by the user, inside and outside the tumor, and the definition of a point that is roughly the furthermost one from the first contoured region. Figure 3.4 shows some examples of the algorithm, on both AP and LAT images, with silicon tumor. The presence of marked wood grain from the couch used to support the phantom makes it difficult to segment the tumor in AP. To tackle this problem a Gaussian filter is applied to the AP images, which smooths the grains and allows tumor identification. Moreover, in order to fill possible holes, a dilation is performed before centroid computation.

Once found the pixel coordinates associated to the centroid (y and z from LAT images, x and z from the AP ones), the corresponding shift is evaluated with respect to the coordinates in the reference image. Taking into account that the dimensions of the topogram's pixel is 1 mm x 1 mm, it is easy to convert the shift in mm. In this way, it has been possible to calculate all the shifts and the related absolute deviation from one effectively imposed. An uncertainty of 1 mm should considered, as consequence of the resolution of the topogram.

Matching of manually selected corresponding points

The software PPV (Patient Position Verification) is daily used for clinical patient positioning at PSI. The shifts are calculated manually selecting reference and control points in a benchmark planning and a daily image. An uncertainty of 0.5 mm due to the clicking error should be always taken into

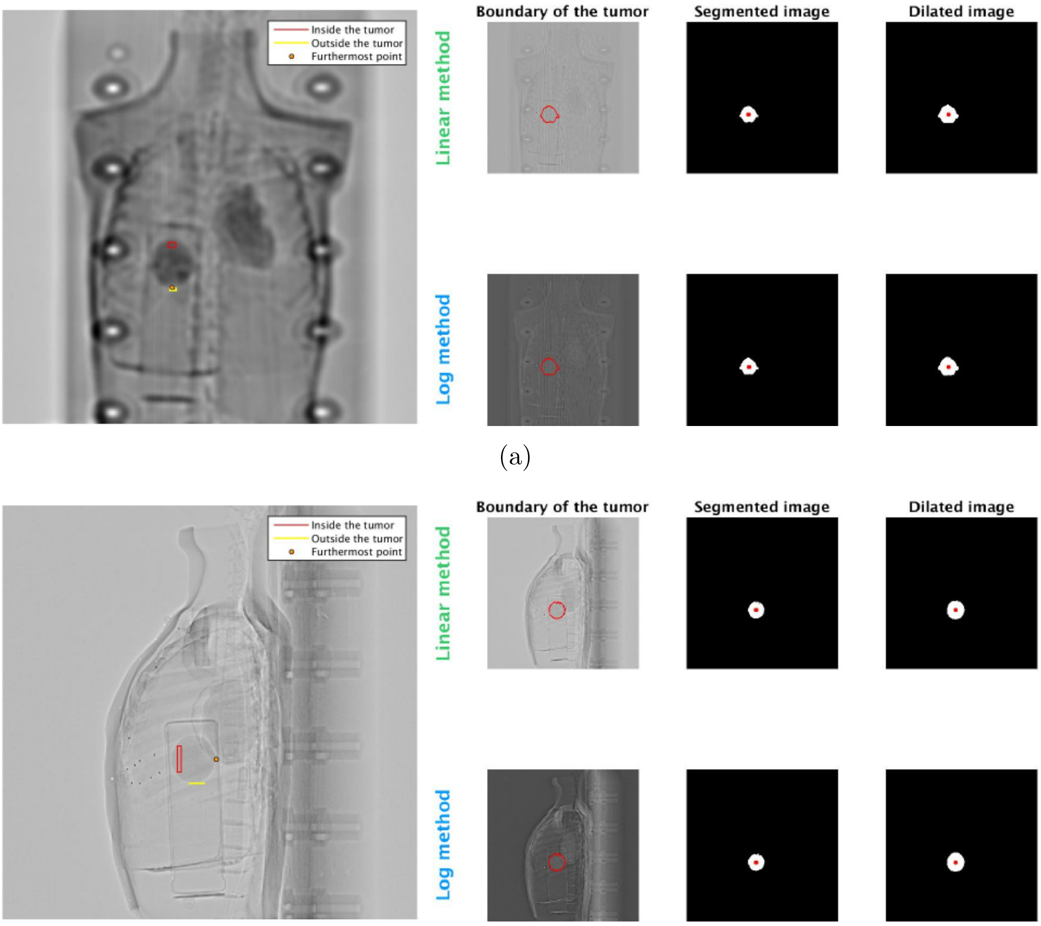

(a)

(b)

Figure 3.4: Example of outputs generated from the algorithm used for segmenting the tumor on bone-canceled images. AP and LAT cases are reported in (a) and (b) respectively. The interactive interface for the user's choice is reported on the left, while on the right the steps of the algorithm (delineation of the boundary, segmentation and dilation of the image) are shown for both linear and logarithmic methods. The red dot in the binary images represents the centroid of the tumor.

account. Mono-energetic, bone-canceled and tumor-canceled performances have been evaluated in this study. For the purpose of this work, the mono-energetic image is acquired at 140 kVp, because it is the more similar to the typical energy used for clinical application at PSI, that is 120 kVp, and it was the HE exploited for the dual energy approaches. As reference image we used for each of the three cases the correspondent one not shifted, in the initial position used of reference, while the test or daily image corresponds to the one with shifts applied.

3 Results

3.1 Comparison of methods and acquisition energies

The obtained SDNR values are reported in Figure 3.5.

For both compositions of tumor, the values of SDNR for anterior-posterior images are lower than those for the corresponding lateral and the results for bone-canceled images are better if the tumor is made by silicon. This is mainly due to the presence of the wooden couch behind the phantom. Furthermore, SDNR in tumor-canceled images are larger if it is made by wood, because it is easier to remove from the background since it is already not so distinguishable from it due to the similarity.

There are no big differences between linear and logarithmic methods, in fact the SDNR values are comparable, just as the related errors. Nevertheless, in the vast majority of cases the fourth combination of energy-current, namely LE 80kVp/90mAs and HE 140kVp/28mAs, shows a better performance than the others considered. For this reason the rest of the work takes into account this combination only. The complete analysis done with the winner combination is reported in Figures A.1, A.2, A.3 and A.4 in Appendix.

3.2 Choice of the ROIs

The second analyses concerns the ROIs choices.

First of all the ones regarding the tumor have been studied. In fact, in real cases, it is usually difficult to select ROIs containing only the tumor, as this can be hidden behind the ribcage and its density could be mixed with other tissues. Many choices of the tumor ROIs have been considered in the analysis: small ROIs between the ribs containing only the tumor (choice 1), large squares (choice 2), big horizontal rectangles (choice 3) and big vertical rectangles (choice 4) inside the tumor itself. The weighting coefficients that

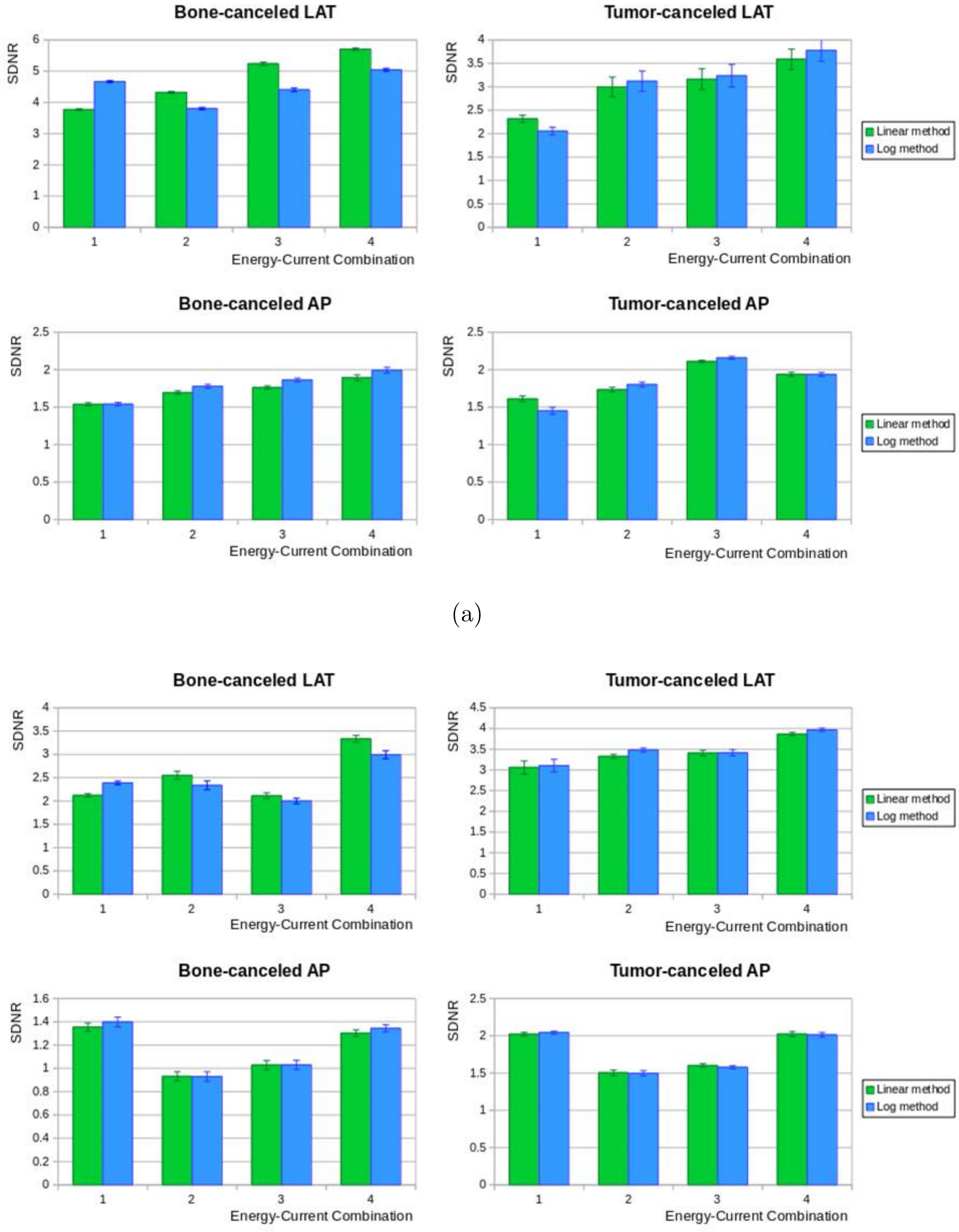

(a)

(b)

Figure 3.5: SDNR values and related uncertainties associated to bone- and tumor-canceled images, both AP and LAT. All the four LE/HE combinations are considered (Table 3.1). In green it is the linear method and in blue the logarithmic. In (a) the results for the tumor in silicon, while in (b) for the wood.

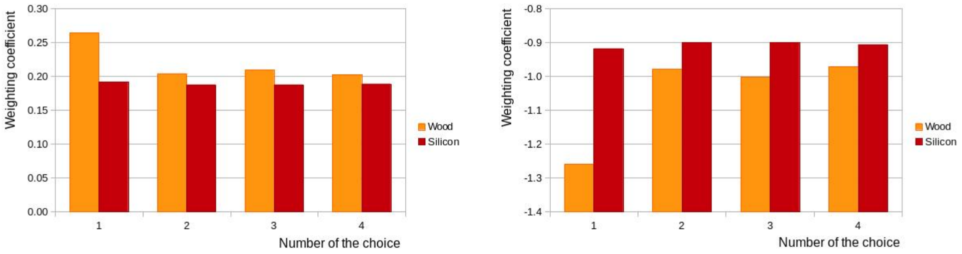

(a) (b)

Figure 3.6: Weighting coefficients for linear (a) and logarithmic (b) methods with different choices of the tumor ROIs in LAT images: 1 - small ROIs containing only the tumor, 2 - big squares, 3 - big horizontal rectangles, 4 - big vertical rectangles.

minimize the contrast for all the considered choices of the tumor ROIs are presented in Figure 3.6, while Figure 3.7 displays the related bone-canceled and tumor-canceled images for LAT acquisitions with wooden tumor. However similar results have been found for AP images and the tumor in silicon.

From the data, choosing large ROIs, not paying attention to avoid the overlapped ribs, gives better cancellation of the tumor. In fact for the choices 2, 3 and 4 the images appear clearer and the weighting coefficients are similar to each other. Moreover, images with silicon tumor are more robust with respect to the choice than the ones with wood. For this reason, in the rest of the work we selected large tumor ROIs. The only warning is being careful to not cross the border of the tumor, in order to do not mix different tissues, compromising the cancellation of the tumor.

Regarding the background choice, ROIs were placed inside the soft tissue (choice 1) and in the air surrounding the patient (choice 2). In Figure 3.8 bone-canceled and tumor-canceled images obtained with both choices of the background ROIs and silicon tumor (similar results for wood) are shown. In AP images, background ROIs inside the air give bad cancellation of the bones, while in LAT, comparable results were obtained with both choices in terms of SDNR values and subjective evaluation. The differences between AP and lateral are mainly due to the presence of the couch behind the phantom.

Despite contrast between background and bones being minimized, the complete bone removal with respect to the couch was not completely achieved. This could be a limitation for the application in real patient, due to the presence of other tissues and organs in the body.

For bone ROIs, it has been found that the better choice is always inside the lower part of the spine cord, since there the vertebrae are clearer and not hidden behind the ribs.

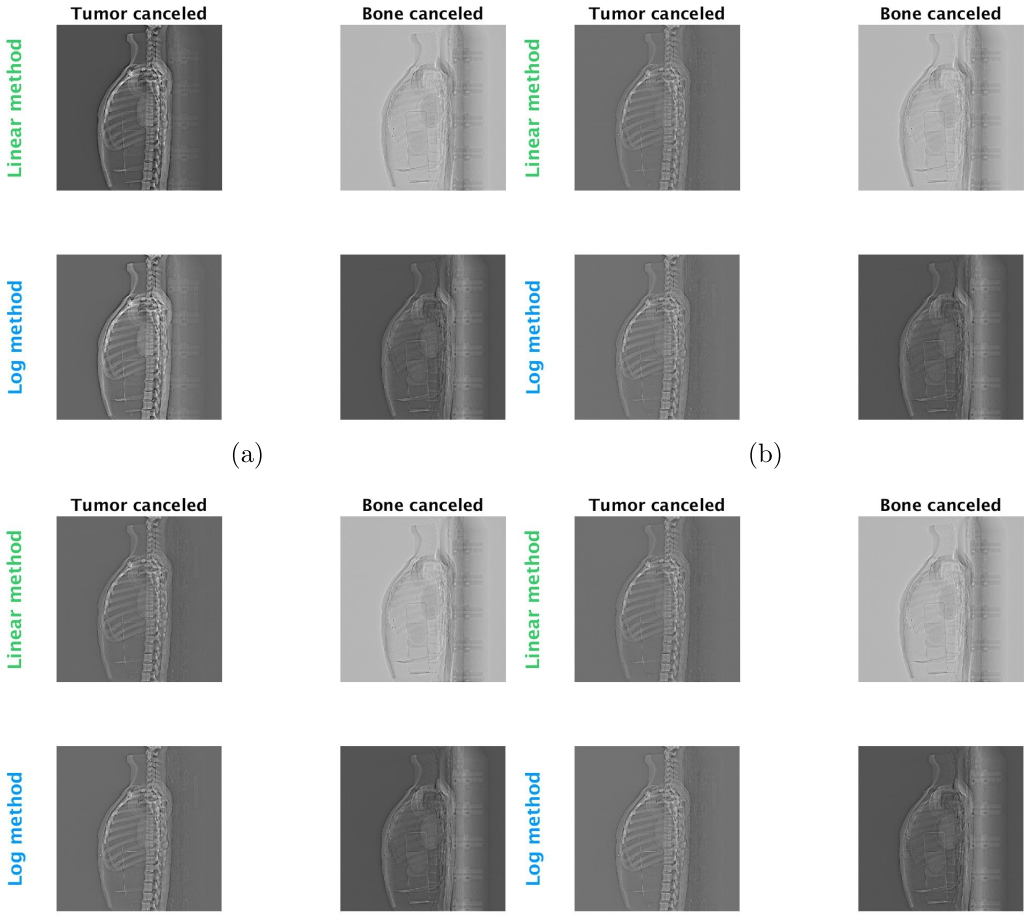

(a) (b) (c) (d)

Figure 3.7: Bone-canceled and tumor-canceled images obtained with different choices of the tumor ROIs for wood tumor in LAT images. Different choices are considered: small ROIs between the ribs containing only the tumor (choice 1, in a), large squares (choice 2, in b), big horizontal rectangles (choice 3, in c) and big vertical rectangles (choice 4, in d) inside the tumor itself.

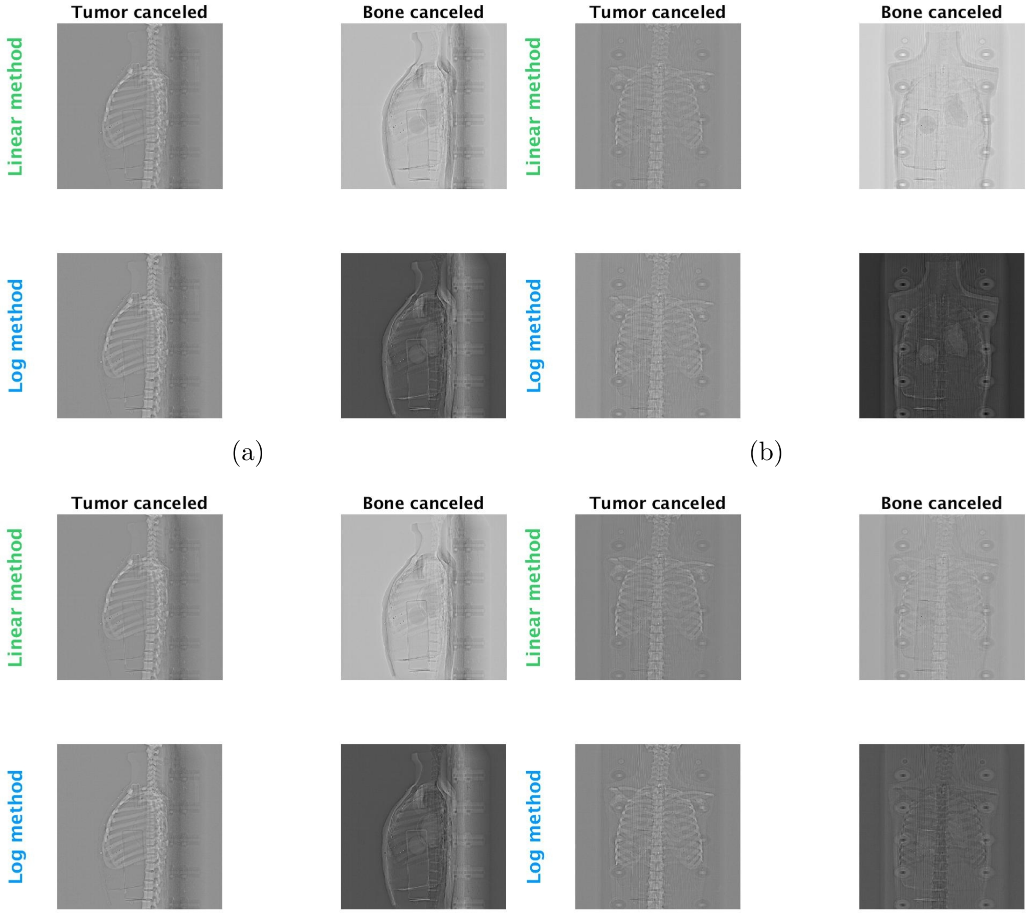

(a) (b)

(c) (d)

Figure 3.8: Bone-canceled and tumor-canceled images obtained with different choices of the background ROIs for silicon tumor. Different choices are considered: inside the soft tissue (choice 1, in a for LAT and in b for AP) and in the air surrounding the patient (choice 2, in c for LAT and in d for AP).

3.3 Relevance for patient positioning

All the shifts found with the segmentation algorithm and the related absolute deviations from the known ones are reported in Figure 3.9, for the case of silicon tumor. The residuals are within 2.0-2.5 mm, with improved values if using the dilation. The logarithmic method seems to give in general better results than the linear one and therefore we further used that one. Because of the poor quality of segmentation, the wooden tumor has not been further analyzed.

In Figure 3.10, the absolute deviations from the reference shifts found with both segmentation algorithm on bone-canceled images and PPV on the mono-energetic images acquired directly with the CT are reported. Based on these results, PPV is definitely the method between the two that gives better and more satisfying results, with deviations of the shift from the known ones of maximum 0.5 mm.

For that reason we focused our attention on the PPV software only, by comparing its performance using mono-energetic and both canceled images (Figure 3.11). It can be concluded that the smallest deviations are reached with the tumor-canceled images, proving the relevance of contrast enhancement for the patient positioning.

4 Discussion and Outlook

The developed algorithm for contrast enhancement based on dual-energy X-ray imaging has shown its potential in obtaining bone-canceled and tumor-canceled images for 2D images, as topograms. In particular, the images where the bone has been removed allows to enhance the tumor contrast, making visible tumors otherwise not visible by human eyes, due to either the hidden position or the low density.

Linear and logarithmic methods gave comparable results in terms of SDNR and image quality. Only for the segmentation of the bone-canceled images, the logarithmic method seems to give better results and was finally chosen for the final implementation of the algorithm. These low differences between the two methods can be explained by the fact that both of them are combinations of the input images, with different weighting coefficients that are minimized in order to achieve the same goal. As regards the energies required for the acquisition, LE 80kVp/90mAs and HE 140kVp/28mAs gave the better performance in our CT. This can be explained considering that the associated spectra are in this combination less overlapped than for example 80 kVp with 120 kVp. Therefore, more information can be extrapolated from

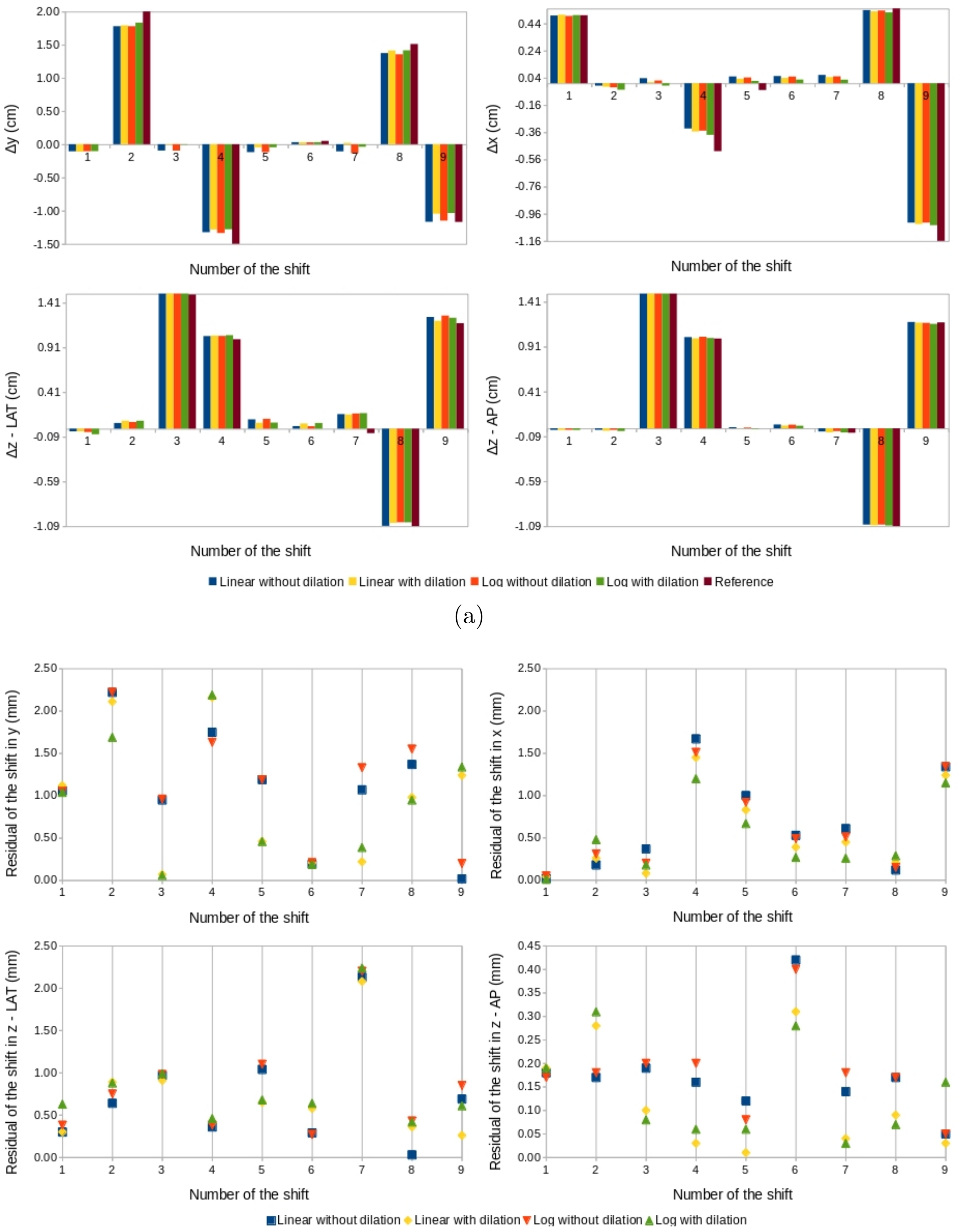

(a)

(b)

Figure 3.9: Shifts (a) and related absolute deviations from the known ones (b) found by segmenting the bone-canceled images, with silicon tumor. Nine different shifts have been analyzed, as reported in Table 3.2. Both linear and logarithmic methods are considered, with and without dilation.

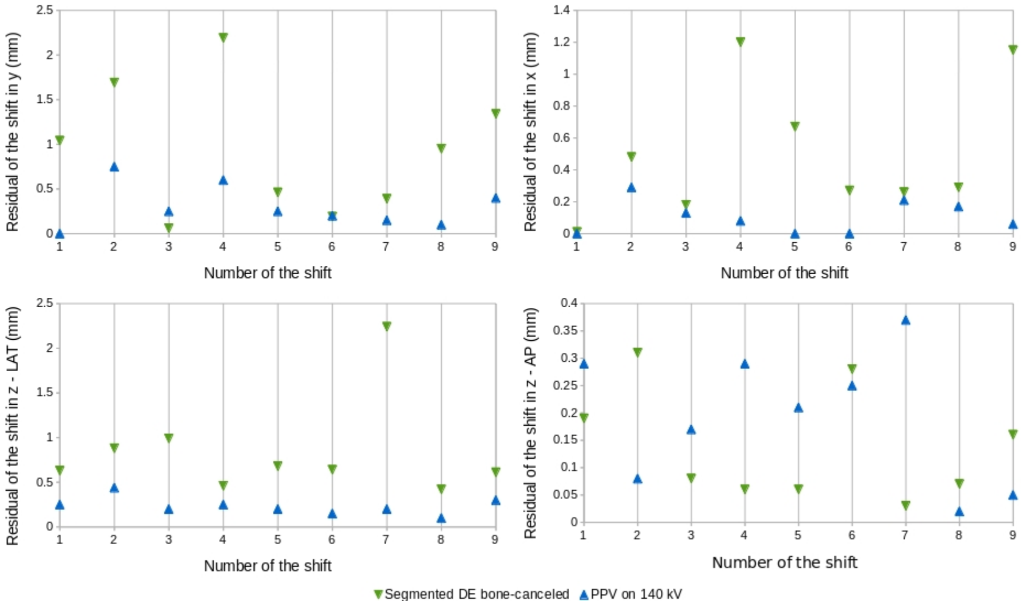

Figure 3.10: Absolute deviations from the known shifts found with segmentation algorithm applied on bone-canceled images (logarithmic method with dilation) and with PPV applied on images acquired at 140 kVp. Nine different shifts have been analyzed, as reported in Table 3.2.

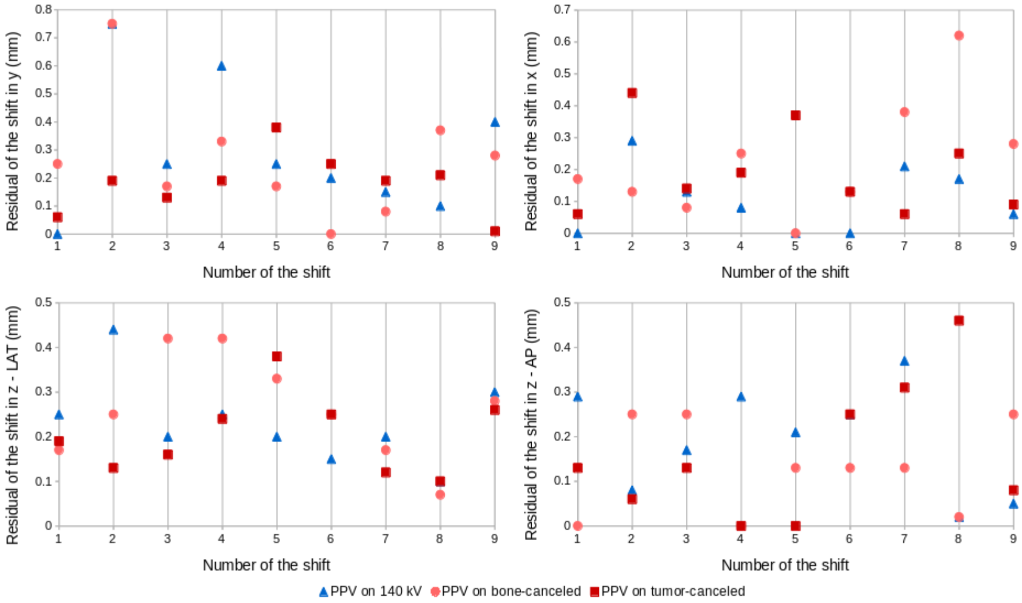

Figure 3.11: Absolute deviations from the known shifts found with PPV on 140 kVp, bone-canceled and tumor-canceled images. Nine different shifts have been analyzed, as reported in Table 3.2.

the data and better performance can be achieved. However, to choose a clinical combination, each system should be characterized individually. In fact, different properties, such as detector, X-ray tube and set-up of the machine, might affect the optimal energy combination.

Furthermore, the method is robust respect the choice of the tumor ROIs, whose only constraint is being completely inside the border of the malignancy. Looking at the clinical application, this would mean that the ROI choice does not have to be too accurate. In fact it is usually difficult to select regions containing only tumor, especially for those cases where it is located in the thoracic region, therefore hidden by the ribs. For what concerns the ROIs for the background, we saw that for lateral images they should be chosen inside the surrounding soft tissue, instead of the air around the patient. This could be a limitation for the application in real patients, due to the inhomogeneity caused by the presence of other tissues and organs inside the human body and of the tumor itself.

The effect of inhomogeneities on the algorithm have to be further investigated. We could anyhow successfully reproduce a typical patient positioning work-flow, confirming the advantage of DE X-ray imaging over SECT for proton therapy. In fact, using the resulting bone-canceled and tumor-canceled images, the patient could be positioned based on both bone and tumor structures. Moreover, using the additional segmentation of the tumor on bone-canceled images, the algorithm might be used for positioning the patient based on the tumor position, which in some cases could provide more useful information than patient positioning based on bony anatomy only.

In this work, we did not account for breathing motion, which shall be compensated for before going into clinical routine. In fact, it could affect the performance of the algorithm. For that reason a real DECT might be used, instead a double scanning using a single source CT.

Chapter 4

Dealing with Metal Artifacts

"The painter's only solid ground is the palette and colors,
but as soon as the colors achieve an illusion,
they are no longer judged."
- Pierre Bonnard -

Focus of this study is the investigation, in an experimental scenario, of different possible approaches for dealing with metal artifacts introduced in the planning CT of patients presenting stabilizing implants.

1 Introduction

Many patients referred to PSI are evaluated for post-operative radiotherapy. In cases of tumors as chordomas and chondrosarcomas along the spinal cord, surgery often implies the partial or complete removal of one or more vertebrae, with the consequent insertion of metal stabilizing rods. These implants, although essential for supporting the remaining vertebral bodies, can cause great problems for radiotherapy, especially in proton therapy. First of all, metal artifacts present in the planning CT introduce non negligible uncertainties in stopping power evaluation. Moreover, their presence makes contouring and delineation of volumes extremely difficult [Verburg and Seco, 2013]. Furthermore, the extremely sharp interface between soft tissue and metal degrade the accuracy of the dose calculation by clinical algorithms. This is mainly due to an inaccurate simulation of proton beam transport through the implants, which have very different properties compared to human tissue [Lomax, 2008].

An indication that proton therapy is more successful for patient without implants has been found in the study of [Rutz et al, 2007]. The author studied a total amount of 26 patients with extra cranial chordomas, among which

13 had metal implants. Five patients, all with metal rods, developed a local failure, which is defined as the radiologically documented tumor progression at the irradiated site on two consecutive examinations or as the documented progression causing clinical symptoms. Moreover, the local control (i.e. the arrest of cancer growth at the site of origin) after three years was 100% for patients without any implant, and 69% for those with a metal rod inside the tumor region. There is so a probable significant influence of the metal implants on the proton therapy's outcome. Anyway, it must be said "probable" because it is to remark that patients need a stabilizing titanium's rod only when their vertebrae (or part of them) have to be removed. That means that the disease is in an advanced state because the tumor has already penetrated deep into the bone and it's of course more resistant.

At PSI, the current method to compensate for these effects relies on a manually correction of the artifacts by the clinician [Dietlicher et al, 2014]. However, this procedure is time-consuming (depending on the complexity up to eight hours) and the result is a region of interest with constant HU value (close to HU average of the substituted tissue). With the scientific and technical progress of the recent years, many other techniques have been introduced in order to reduce the reconstruction artifacts. Two examples are the Sinogram AFfirmed Iterative REconstruction (SAFIRE), i.e. an iterative method for CT data reconstruction alternative to Filtered Back Projection (FBP), and Iterative Metal Artifact Reduction (iMAR), i.e. an algorithm that has been already proposed as an alternative in a first preliminary planning study on photons and protons [Axente et al, 2015]. These two imaging tools, together with a Dual Energy approach, are subjects of this study, in order to verify their potential as alternative methods for dealing with metal artifacts present in the planning CT. To do that, a treatment plan has been defined on the anthropomorphic head phantom and afterwards, for each scenario, calculated dose distributions have been compared with the corresponding measured ones.

2 Materials and Methods

2.1 Phantoms

The study is based on CT acquisitions, dose calculation and dose delivery for an anthropomorphic head phantom. For all the different options of single energy CT, conversion HU-RPSP (Part I - 2.2.2) was determined on CT acquisition of Head and Body phantoms.

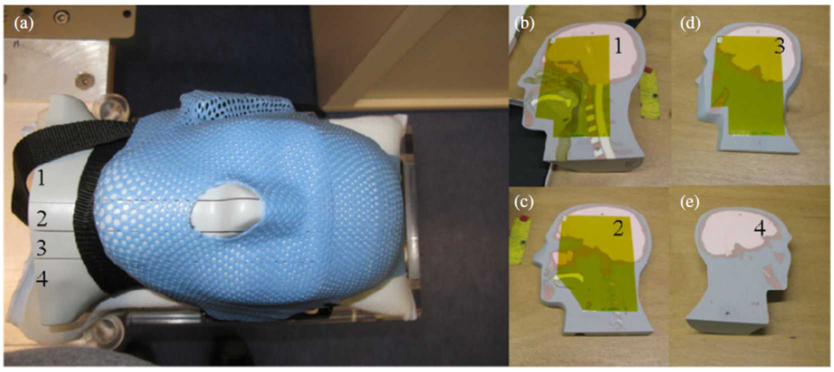

Figure 4.1: Charlie phantom with its individualized fixation device: the four (1–4) components of the phantom are shown, both combined together (a) and individually (b–e) [Albertini et al, 2011].

Anthropomorphic phantom

The anthropomorphic head phantom Charlie (Figure 4.1) corresponds to an adult human head in size and in its anatomic structures [Albertini et al, 2011]. Additionally, it contains a titanium rod fixed with two screws implanted in a cervical vertebra. The phantom is sliced into four segments along the cranio-caudal direction such that radiochromic films can be placed in three different planes, one being adjacent to the titanium rod. Probes made of its five constituent materials are also available, with compositions reported in Table 4.1.

Material	**Substitute for**	**H**	**C**	**N**	**O**	**Mg**	**Al**	**P**	**Cl**	**Ca**	ρ ($\frac{g}{cm^3}$)
DTB 109	Trabecular Bone	0.0699	0.5630	0.0203	0.2273	0	0	0.0330	0.0016	0.0849	1.16
LDT	Sinus Cavities	0.0833	0.6337	0.0316	0.2047	0	0.0330	0	0.0137	0	0.21
VSC 31	Spinal Cord	0.0736	0.5428	0.0217	0.2660	0.0937	0	0	0.0022	0	1.07
BT 358-1	Brain	0.0817	0.5361	0.0154	0.2650	0.0999	0	0	0.0019	0	1.07
STG 955	Soft Tissue	0.0848	0.5745	0.0165	0.2460	0.0763	0	0	0.0019	0	1.05

Table 4.1: Tabulated compositions (percentage weights normalized to one) and mass density for the five probes of Charlie phantom.

Calibration phantoms

To obtain the parameters necessary for stoichiometric calibration (Part I - 2.2.2), Body and Head phantoms, presented in Figure 4.2, are used for the measurements. Both of them are made of polymethyl methacrylate (PMMA) and contain five probes of tissue substitutes, the same used by [Schneider et al, 1996] (Table 4.2). The Body phantom is a 32-cm-diameter solid disk with five holes for insertion of the probes, used to simulate an adult

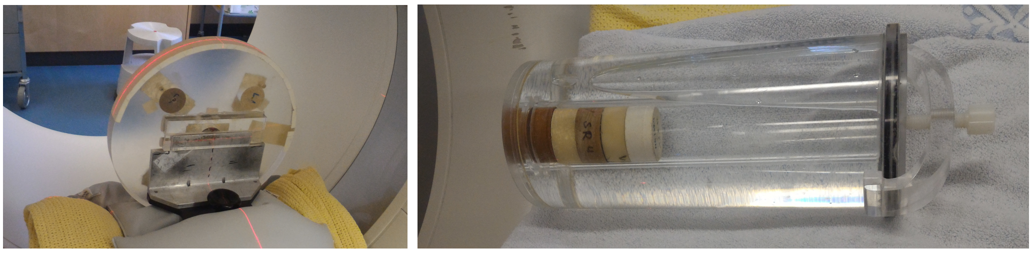

(a) Body (b) Head

Figure 4.2: Phantoms used at Paul Scherrer Institut for CT stoichiometric calibration: Body in a) and Head in b).

abdomen. The Head phantom is a hollow cylinder filled of water, containing the samples in column in the central cavity, used to represent an adult head or small pediatric bodies.

The common procedure is to acquire their images with the CT scanner and subsequently find the mean values of HU associated to each probes, averaging ROIs belonging to 3-5 slices. With the Head phantom the mean HU of water is also found. A larger water phantom to simulate body water is also present at PSI, however not used such as this one.

The stoichiometric calibration is assessed with both phantoms because the beam hardening effect is in general different in the two geometries, due to the distinct composition materials, dimension and thickness. The difference between the two obtained curves, in standard conditions, is in general 3-5% (higher in the bone regions).

Material	Substitute for	H	C	N	O	F	Na	Mg	P	S	Cl	K	Ca
Water		11.19	0	0	88.81	0	0	0	0	0	0	0	0
AP6	Fat	8.36	69.14	2.36	16.94	3.07	0	0	0	0	0.14	0	0
MS/SR4	Muscle	9.5	70.25	3.48	15.15	0	0.08	0.02	0.18	0.50	0.12	0.30	0.01
IB/SR1	Inner Bone	8.73	63.19	2.36	17.83	0	0.06	0	2.62	0	0.12	0	5.09
TSK/SR1	Skeleton	6.4	46.4	2.80	26.4	0	0.30	0.10	7.0	0.20	0.10	0.20	10.0
HB/SR4	Hard Bone	4.45	29.09	3.88	31.93	0	0.06	0.21	10.0	0.32	0.06	0	19.99

Table 4.2: Tabulated compositions (percentage weights) of the calibration probes used for Body and Head phantoms.

2.2 CT approaches in presence of metal artifacts

For this study, seven different options coming from imaging have been considered, in order to determine which of them could be relevant for dealing with metal artifacts. The methods are the following:

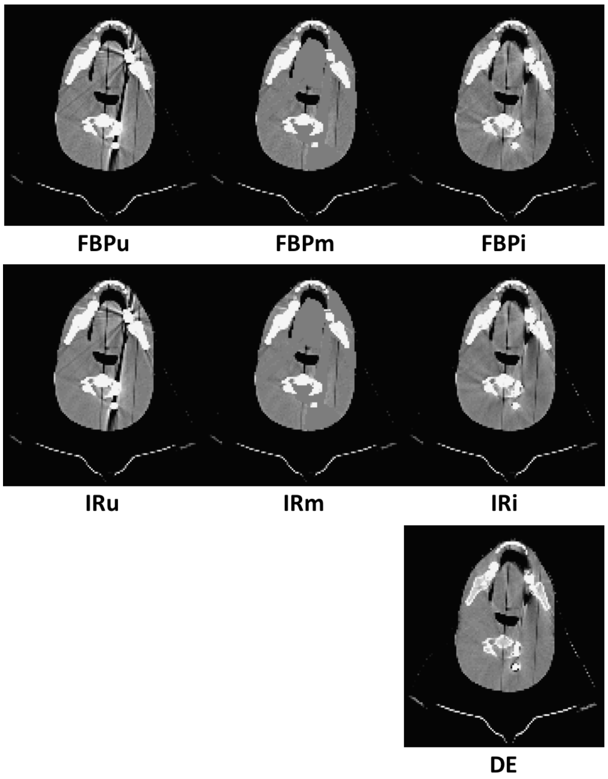

FBPu FBPm FBPi

IRu IRm IRi

DE

Figure 4.3: Effect of the seven approaches for dealing with metal artifacts investigated in this study on the same slice of Charlie's CT.

- SECT using FBP and no correction of the metal artifacts;
- SECT using FBP and manual correction of the metal artifacts;
- SECT using FBP and iMAR algorithm;
- SECT using SAFIRE and no correction of the metal artifacts;
- SECT using SAFIRE and manual correction of the metal artifacts;
- SECT using SAFIRE and iMAR algorithm;
- DECT using FBP and iMAR algorithm.

In Figure 4.3 the effect of the different approaches on the same slice of the anthropomorphic head phantom is shown. In the following sections they will be denoted with the following denotation: FBPu, FBPm, FBPi, IRu, IRm, IRi, DE.

All these approaches are underpin the dose calculation. For the first six, based on SECT, stoichiometric calibration curve based on Head and Body phantom is used. Instead, for the last approach based on DECT, ρ_e and Z_{eff} are extrapolated in order to directly find RPSP maps.

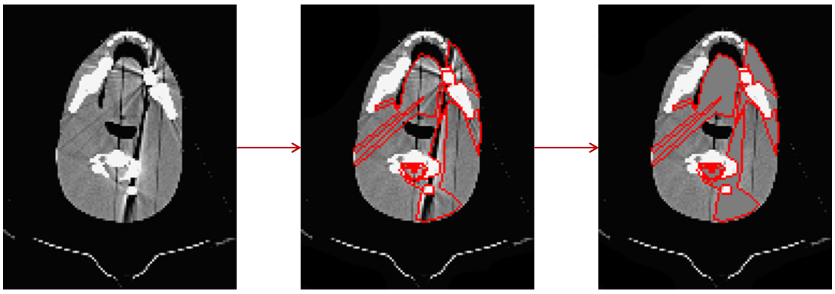

Figure 4.4: Procedure of manual correction of a slice of Charlie's CT: the doctor delineates the regions affected by the artifact and replaces these HUs with the mean CT number of the surrounding soft tissue.

Manual correction

The manual correction of metal artifacts is the method currently used at PSI for treating patients with metal implants. Once the planning CT of the patient has been acquired, the clinician manually contours the artifacts, for each CT slice. Subsequently, the CT numbers corresponding to the delineated region of interest are replaced by the mean HU value of the surrounding soft tissue (Figure 4.4). For that reason this procedure is extremely time-consuming and permits to insert inside the delineated artifact only a single hypothetical value of the real CT number. However, although this method implies an approximation of the linear attenuation coefficients, it has been shown that the accuracy of the dose calculation using this approach is surprisingly good, implying that, at least from a dosimetric point of view, the beam directions are carefully selected and any reconstruction artifacts are adequately corrected [Dietlicher et al, 2014]. In this way, this previous study demonstrated that patients with metal implants could be clinically treated with multiple fields approach.

iMAR

As previously outlined, a very prominent CT artifact is caused by the presence of high density objects in the field of measurement, such as metal objects like dental fillings, screws, fixations or hip and knee implants (Part I - 2.1.4). In many cases, there is no usable information in the detector readings behind the metal, therefore the regions of the artifacts need to be replaced by some surrogate data. Besides manual correction, described in the previous paragraph, a possible way to do that is by inpainting the data gaps using linear interpolation. The risk in using this approach is the introduction of new artifacts in the image. However, it has been shown that applying the in-

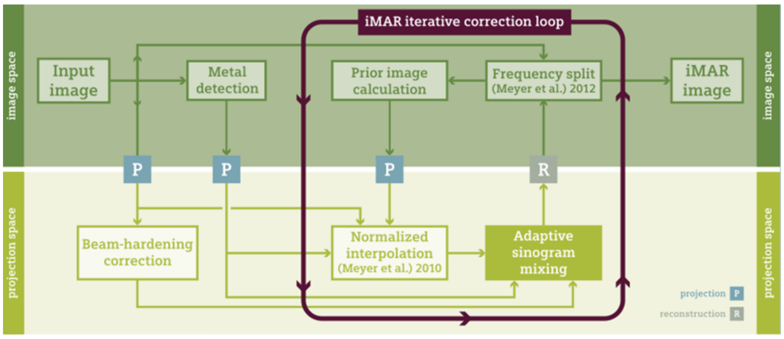

Figure 4.5: Diagram of Iterative Metal Artifact Reduction (iMAR) algorithm [Kachelrieß and Krauss, 2015].

painting method on a normalized sinogram, instead of the original raw-data, can overcome that issue, providing clinical valuable results. In addition, a frequency split technique can restore the original noise texture and the high frequency details that may have been lost during the previous inpainting.

The great innovation of Iterative Metal Artifact Reduction (iMAR) algorithm developed by Siemens is the combination of three successful and well-known methods used to either reduce or remove metal artifacts: beam hardening correction, normalized sinogram inpainting and frequency split [Kachelrieß and Krauss, 2015]. The iMAR process, represented in Figure 4.5, can be summarized as follows:

- Metal detection: very dense objects are detected using a thresholding process in the original CT image and then converted to sinogram by forward projection. This metal sinogram is zero in regions not influenced by the metal artifacts, and non-zero where a correction shall occur.
- Beam hardening correction: the sinogram of the original CT image is beam hardening corrected in the non-zero regions of the metal sinogram.
- Cycle of iteration (up to six times):
  - Prior sinogram: a prior image is calculated from the CT image by assigning the CT number of water to metal and soft tissue pixels, while bone, air and lung tissue pixels remain unchanged. In this way a classification into metal, bone, soft tissue and lung tissue is performed through a thresholding process based on the HU value. Then, the prior image is forward-projected to obtain the prior sinogram.
  - Normalized Interpolation: inpainting is performed on the normalized sinogram (initial sinogram divided by the prior one) using

1D linear interpolation. Then, the normalized sinogram is denormalized by multiplication with the prior sinogram.
- Adaptive sinogram mixing: the inpainted sinogram is mixed with the beam hardening corrected one. This mixing is done according to the total metal attenuation: pixels corresponding to low metal attenuation are preferably taken from the beam hardening-corrected sinogram, while those corresponding to larger metal attenuation are preferably taken from the inpainted one.
- Frequency split: the adaptively mixed sinogram is reconstructed in an image and then low-pass filtered, while the original image is high pass filtered, with low and high pass filters being complementary. Both filtered images are added, in order to obtain the metal artifact-corrected image. However, this operation could insert high-frequency streak artifacts into the corrected images. Therefore, this corrected image is taken as a starting point for the next iteration.

SAFIRE

As mentioned in Part I - 2.1.3, traditional IR is extremely time-consuming due to its raw data reconstruction loops. For that reason, in 2010 Siemens introduced an alternative method, in order to overcome this limit while preserving the benefits of the traditional one. This technique is the so called Sinogram AFfirmed Iterative REconstruction (SAFIRE).

The basic idea of SAFIRE relies on the linear nature of CT image reconstruction. In fact, it has been mathematically demonstrated that, thanks to this property, noise reduction can be achieved with the same performance of traditional IR using the image domain, instead of raw data space. For that, the required computational time can be extremely reduced: just a rough modeling of the projection rays is necessary and the loop cycles inside the raw data space is only used for artifact reduction and increased spatial resolution. The SAFIRE reconstruction is composed by an initial reconstruction using a FBP, followed by two different correction loops (Figure 4.6). In the first one, used to correct imperfections in the original reconstruction and remove any artifacts, data is re-projected into the raw data space. The detected differences between measured and simulated data are again reconstructed using the FBP, yielding an updated image. This loop is then repeated a number of times depending on the exam type. Furthermore, within each iteration a dynamic raw-databased noise model is applied. The second loop is done in the image space, where noise is removed from the image through a statistical optimization process. However, the regularization is still based on the

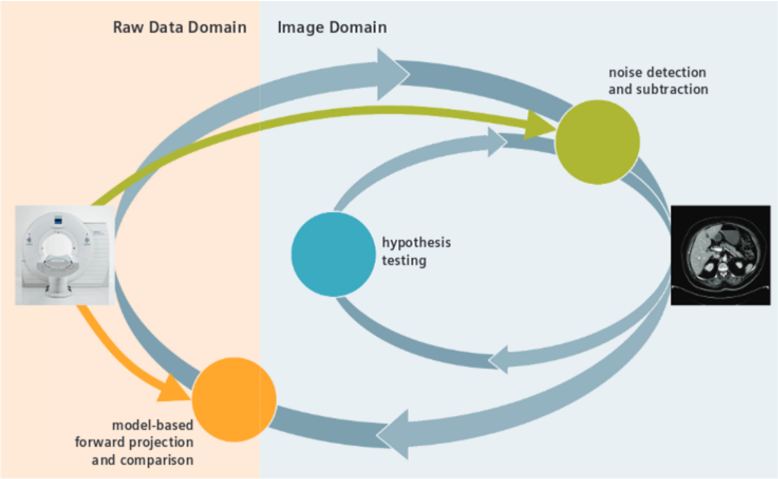

Figure 4.6: Diagram representing the process underlying Sinogram AFfirmed Iterative REconstruction (SAFIRE) [Grant and Raupach, 2012].

knowledge of how noise in the projection data propagates into image space. Also in this case, the corrected image is compared to the original one and the process is repeated a number of times depending on the exam type.

In contrast to traditional IR, SAFIRE is available right on the scanner. It can reconstruct up to 20 images per second, providing up to 60% reduction in dose. Five different "strengths", defining parameters of the underlying noise model/regularization, are settable: with strength 1 is the noisiest image, while with strength 5 is the smoothest one [Grant and Raupach, 2012].

DECT-based RPSP evaluation

DECT images are converted to RPSP in an almost direct and more physics-related approach as compared to the SECT stoichiometric calibration, which is based on the CT number that is influenced by both ρ_e and Z_{eff} (Part I - 2.2.2).

The possibility to obtain stopping power images from DECT relies on its potential in predicting electron density relative to water $\hat{\rho}_e$ and effective atomic number Z_{eff} maps from the knowledge, for each voxel, of the linear attenuation coefficients at two different energies. These two parameters can be related to the HU values at low (HU_{LE}) and high (HU_{HE}) energies through [Hünemohr et al, 2014a]:

$$\hat{\rho}_e = A \cdot \left(\frac{HU_{LE}}{1000} + 1 \right) + (1 - A) \cdot \left(\frac{HU_{HE}}{1000} + 1 \right) \tag{4.1}$$

$$Z_{eff} = \sqrt[n]{\frac{B \cdot \left(\frac{HU_{LE}}{1000} + 1\right) + (Z^n_{eff,w} - B) \cdot \left(\frac{HU_{HE}}{1000} + 1\right)}{\hat{\rho_e}}} \tag{4.2}$$

where A and B depend on the two employed spectra and can be found using dual energy scan of calibration materials, with known $\hat{\rho_e}$ and Z_{eff}, while $Z_{eff,w}$ is the effective atomic number of water. Instead, n is a parameter dependent on the photon spectra of the scanner and for standard tissue compositions it varies approximately from 2.8 and 3.8 in the diagnostic X-ray regime, dependent on the photoelectric and Compton effect contributions to the overall photon attenuation. For this work, n was set to 3.1 representing the scanner spectrum combination available in the second generation of dual source [Hünemohr et al, 2014a], [Hünemohr et al, 2014b]. However, it must be noticed that Siemens dual energy CT scanner are already equipped with software developed for the direct and instant extraction of electron density relative to water and effective atomic number images related to the two dual energy images given as input. From the knowledge of $\hat{\rho_e}$ and Z_{eff}, stopping power images are then evaluated inserting this information into Equation 1.6. In fact the effective atomic number is related to the mean excitation value I through an empirical relationship [Yang et al, 2010], [Bourque et al, 2014]:

$$ln(I) = \begin{cases} e_1 + e_2 Z_{eff} & Z_{eff} < 7 \\ e_3 + e_4 Z_{eff} + e_5 Z^2_{eff} + e_6 Z^3_{eff} + e_7 Z^4_{eff} + e_8 Z^5_{eff} & 7 \leq Z_{eff} \leq 12 \\ e_9 + e_{10} Z_{eff} & Z_{eff} > 12 \end{cases} \tag{4.3}$$

where the parameters $\boldsymbol{e}$ can be obtained by least square fits (two linear and one fifth grade polynomial) using 71 standard human tissues, the same used in [Schneider et al, 2000]. Using their tabulated elemental compositions, related effective atomic numbers [Johns, 1983] and I-values [ICRU, 1993] can be calculated from:

$$Z_{eff} = \sqrt[n]{\frac{\sum_i \frac{\omega_i Z_i^{n+1}}{A_i}}{\sum_i \frac{\omega_i Z_i}{A_i}}} \tag{4.4}$$

$$ln(I) = \frac{\sum_i \frac{\omega_i Z_i}{A_i} ln(I_i)}{\sum_i \frac{\omega_i Z_i}{A_i}} \tag{4.5}$$

where ω_i, Z_i, A_i and I_i are respectively weight, atomic number, mass number and mean excitation energy of the i-th component of the mixture. Following

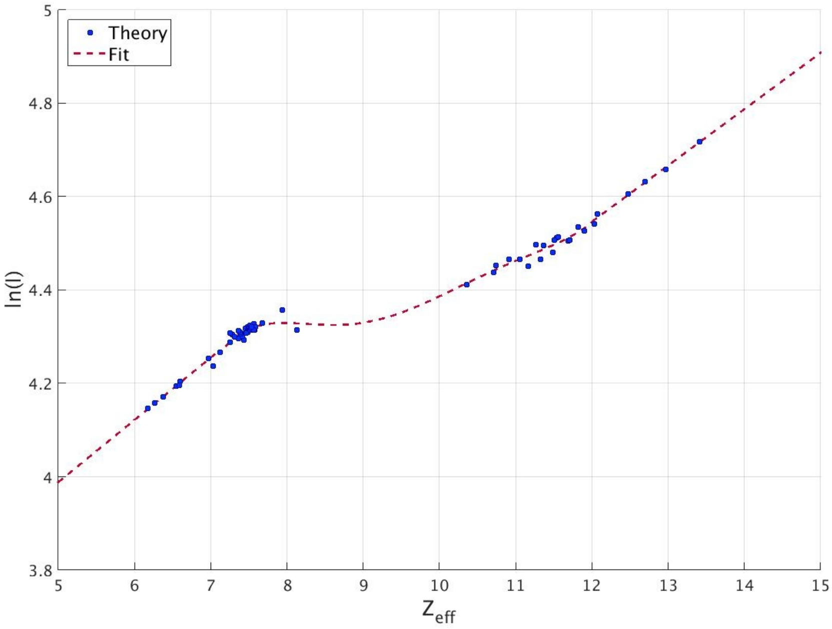

Figure 4.7: Fit of mean excitation energy as a function of the effective atomic number for the 71 ICRP tissues presented in [Schneider et al, 2000].

this procedure, the parameters $\boldsymbol{e}$ were extracted from the fit of the data related to the 71 tissues. The obtained values are reported in Table 4.3, while the parametrization of the I-value through Z_{eff} is shown in Figure 4.7.

	$\boldsymbol{e_1}$	$\boldsymbol{e_2}$	$\boldsymbol{e_3}$	$\boldsymbol{e_4}$	$\boldsymbol{e_5}$	$\boldsymbol{e_6}$	$\boldsymbol{e_7}$	$\boldsymbol{e_8}$	$\boldsymbol{e_9}$	$\boldsymbol{e_{10}}$
fEstimate	3.32	0.133	-150	80	-16	1.7	-0.09	0.0017	3.1	0.121
Error	0.03	0.004	40	20	4	0.4	0.02	0.0005	0.1	0.005
p-value	$4.7\cdot10^{-10}$	$3.8\cdot10^{-7}$	$1.3\cdot10^{-4}$	$1.3\cdot10^{-4}$	$1.9\cdot10^{-4}$	$2.6\cdot10^{-4}$	$3.5\cdot10^{-4}$	$4.7\cdot10^{-4}$	$1.4\cdot10^{-6}$	$2.4\cdot10^{-5}$

Table 4.3: Parameters $\boldsymbol{e}$ *found with least square fits of Equation 4.3 on* Z_{eff} *and* $ln(I)$ *values of 71 ICRP tissues presented in [Schneider et al, 2000].*

2.3 Image acquisition

The data acquisition was done with Dual Energy CT SOMATOM Definition Flash of Kantonsspital Baden, KSB.

The acquired images are:

- SECT using FBP, without iMAR (for FBPu and FBPm approaches);
- SECT using FBP, with iMAR (for FBPi approaches);
- SECT using SAFIRE, without iMAR (for IRu and IRm approaches);
- SECT using SAFIRE, with iMAR (for IRi approaches);

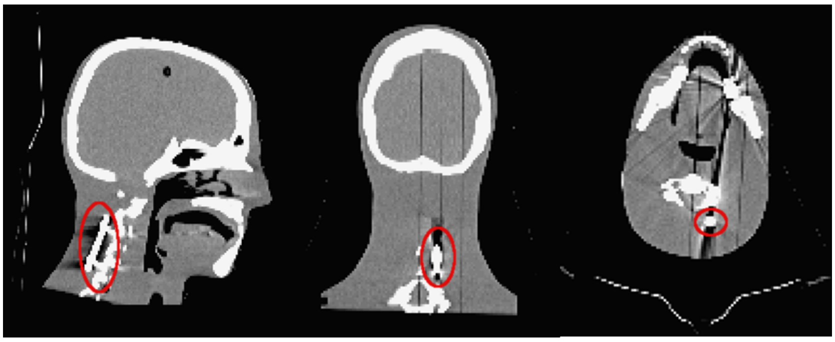

Figure 4.8: Sagittal, coronal and axial views of Charlie phantom, acquired with CT scanner. Metal artifacts are created due to the presence of the titanium implant (circled in red).

- DECT using FBP, with iMAR (for DE approach).

SE images have been acquired with voltages 80 kVp, 100 kVp, 120 kVp and 140 kVp. The kernels used are B30f and I30f (strength 3) respectively for FBP and SAFIRE. Both FOV (500 and 330) have been considered. However, it must be noticed that for the SE images only those with 120 kVp and FOV 500 have been used as planning CT for the treatment plan, in order to be consistent with the protocol currently applied for real patients in PSI. The others have been used for the preliminary analysis. DE images have been reconstructed with kernel D34f. This is a DECT specific kernel that provides an edge enhancement in combination with an advanced beam hardening correction, thus permitting precise definition of large attenuation gradients. The acquisition has been done with the energy combination 80 kVp - 600 mAs, 140 kVp - 232 mAs. From these DECTs, ρ_e and Z_{eff} images have been extracted from the software, in order to reconstruct the related RPSP map using Equations 4.3 and 1.6.

During the acquisitions of the anthropomorphic phantom, individual tailored vacuum pillow and thermoplastic mask were used to immobilize it such as for a real patient. In Figure 4.8 sagittal, coronal and axial views of Charlie phantom are shown, so to see the impact of the artifacts caused by the metal implant.

2.4 Treatment plans

To calculate a realistic dose distribution, a clinician defined a volume correspondent to PTV chordoma in the vertebral area, in the region of the titanium implant. The prescribed dose is 74 Gy(RBE), with 2 Gy(RBE) per fraction, which corresponds to the delivered dose in our experiment.

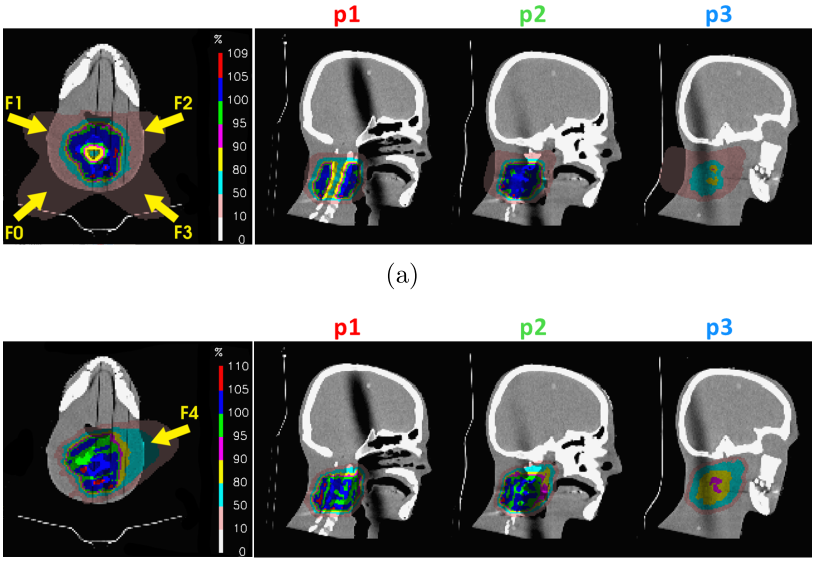

(a)

(b)

Figure 4.9: Calculated and delivered treatment plans: 4-fields IMPT (a) and 1-field SFUD (b). For each plan the proton dose distributions planned in the TPS are reported for the three sagittal planes of the anthropomorphic phantom considered for the measurements.

Two different treatment plans (Figure 4.9) have been calculated with the Treatment Planning System (TPS):

- 4-fields IMPT;
- 1-field SFUD.

The 4-fields plan is a star arrangement with two posterior oblique and two anterior oblique fields commonly used for treatments of head and neck tumors [Albertini et al, 2010]. This has been studied for all the seven approaches. For clinical cases, the delivery of multiple fractions typically reduces the errors, due to the fact that residual positioning errors are mainly random [Bolsi et al, 2008]. As the multiple fields approach can smooth differences between calculated and measured dose due to combination of different single fields doses, we studied a single field plan too. This latter was studied for five approaches (FBPu, IRu, IRi, IRm, DE) only. The four fields of the IMPT plan are reported in Table 4.4, while the field used for the SFUD is the copy of F2.

Both SFUD and IMPT plans have been optimized for each CT approach scenario with constraint for maximum dose in the spinal cord of 90% of the prescribed dose. This means that for each CT approach scenario, the

	F0	**F1**	**F2**	**F3**
α	130°	70°	70°	130°
β	160°	160°	20°	20°

Table 4.4: Gantry angle α and Couch angle β for each field used in the IMPT plan. The SFUD's field is the copy of F2.

optimized spot list is not exactly the same but the resulting dose distributions are not significantly different considering both target coverage and spinal cord sparing. This can be noticed looking at Table 4.5, since dosimetric values related to defined volumes are similar among different approaches.

		4-fields IMPT							**1-field SFUD**				
		FBPu	**FBPm**	**FBPi**	**IRu**	**IRm**	**IRi**	**DE**	**FBPu**	**IRu**	**IRm**	**IRi**	**DE**
PTV	$D_{max}(\%)$	109.8	109	109.3	109.8	109.3	109.4	110.2	111.3	111.3	113.4	113	112.1
	$D_{min}(\%)$	75.1	74.9	75.1	75.1	74.9	74.9	75	69.6	71.6	65.5	72.5	66.5
	$D_{95}(\%)$	77.97	78.85	78.56	78.28	78.58	78.57	78.21	92.45	93.61	92.45	93.93	93.26
SC	$D_{max}(\%)$	89	87.8	89.2	88.6	88.2	89.1	89	106.5	106.5	106.1	106	106.1
	$V_{50}(\%)$	52.45	52.52	52.48	52.45	52.78	52.45	52.45	54.99	54.86	55.31	54.86	55.12
cSC	$D_{max}(\%)$	86.7	85.7	86.7	86.4	86.4	86.4	85.4	103.9	104.1	104.2	104	104.3
	$V_{50}(\%)$	55.62	55.62	55.62	55.62	56.2	55.62	55.62	59.08	59.08	59.08	59.08	59.08

Table 4.5: Percentage values of maximum dose (D_{max}), minimum dose (D_{min}), minimum dose delivered to 95% of the volume (D_{95}) and volume receiving at least 50% of the prescribed dose (V_{50}) for PTV, spinal cord (SC) and center of the spinal cord (cSP) in IMPT and SFUD plans.

Subsequently, the plans have been delivered in Gantry 2 (12 deliveries in total), immobilizing the phantom with the individual tailored vacuum pillow and thermoplastic mask, in order to reproduce its positioning during both the CT planning process and the irradiation (Figure 4.10).

2.5 Radiochromic films

For the spatial dose verification of treatment planning on the anthropomorphic phantom, radiochromic films Gafchromic EBT3 are used. They are well-established and reasonably cheap dosimeters for conventional radiotherapy, capable to measure 2D or 3D dose distributions with a much higher resolution than many commercially available tools. They consist of an active layer (LiPCDA salt) of a thickness of 27 μm. Two PET layers of a thickness of 125 μm with PET-SiO$_2$ layers of a thickness lower than 5 μm are mounted symmetrically around the active layer forming a film of 287 μm total thickness. The major advantages of these films are: broad range of response (from 0.01 Gy, up to 3000 Gy), high spatial resolution ($\sim$ 25 μm), fast optical density growth after exposure, water-resistant properties, low

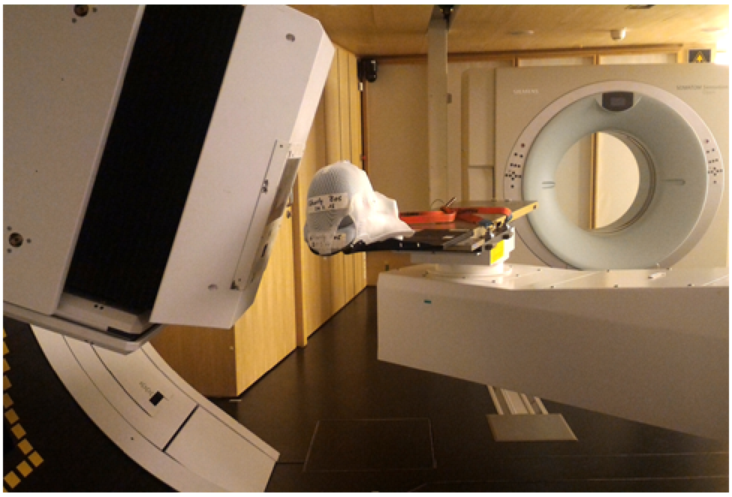

Figure 4.10: Anthropomorphic phantom on the patient couch, with the individual thermoplastic mask, just before the delivery.

sensitivity to visible light, minimized Newtons rings patterns from forming, symmetric along their thickness [Williams and Metcalfe, 2011]. However, the amount of work required to extract dose information makes them highly time consuming.

For each delivery, films were cut in order to fit the anatomical profile of the phantom and then they were inserted in the three sagittal slices, as shown in Figure 4.11. The first slice is positioned in the middle of the target, the second 20 mm laterally and the third one 40 mm. Before and after irradiation, films were scanned and digitized using a commercial A3 size flatbed scanner (Expression 10000XL, Epson) in transmission mode using a transparency adapter. Each film is scanned separately in landscape orientation (shorter side of the whole film parallel to the scanner short side) at the same position in the middle of the scanner bed. The scanning before irradiation was used to measure the background of the film, while the one after the delivery, scanned approximately 24 hours after irradiation, showed the proton dose distribution. The software used for image acquisition was supplied with the hardware (Epson scan v3.04s). All films were scanned in 48-bit color RGB and analyzed using the red channel only, due to its higher sensitivity [Borca et al, 2013]. Multiple scans of each film were taken to obtain a mean value over the regions of interest.

A calibration procedure is required in order to have a convert transmission value into Gray, allowing absolute dose measurements. Moreover, their response is energy dependent with increasing under response at low particle energies, corresponding to high LET regions. In fact, the darkening effect

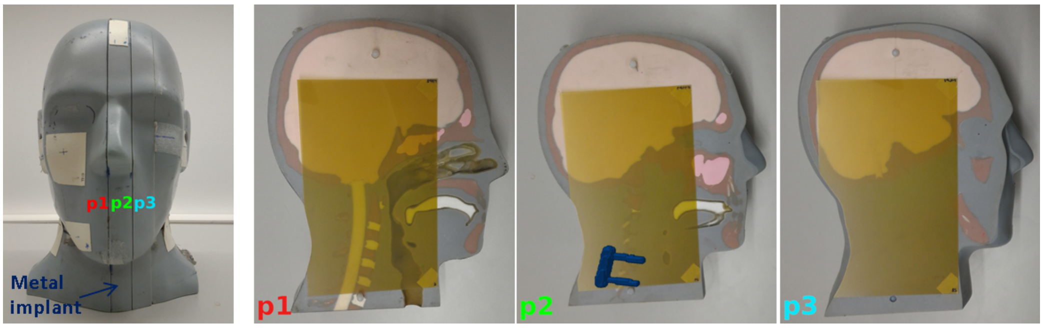

Figure 4.11: Set-up used for measuring delivered dose distributions in the three sagittal planes (p1, p2 and p3) of the anthropomorphic phantom with Gafchromic films EBT3. The metal implant is located between the planes 1 and 2 and, to know where it is positioned inside the neck, a 3D reconstruction of it is superimposed in the plane 2.

caused by the presence of organic monomers, which polymerize under irradiation and which allows to measure an increased optical absorption with increased absorbed dose, is compromised at high LET. One possible explanation is that the polymerization sites are spaced out with some separation: if all sites close to a single ionizing particle track are hit, the polymerization of the film is locally saturated and part of the particle energy loss remains unmeasured [Fiorini et al, 2014]. Their underestimation of the dose has been found to be up to 20% in the Bragg peak, while it is negligible in the plateau region [Reinhardt et al, 2012]. This effect is commonly called “quenching”.

Film calibration

The calibration of radiochromic films is necessary to convert their darkening in actual delivered proton dose. The procedure used at PSI exploits a plane-parallel ionization chamber for the measurement of the unitary dose and a CCD camera for the sampling of the rest values of dose. The calibration has been done with a single layer Bragg peak (mono-energetic 174 MeV), with all the measurements in the plateau region, in order to minimize the quenching effect. The process can be summarized with the following steps:

1. Deliver an homogeneous and nominal dose of 1 Gy and, using a plane-parallel ionization chamber, measure the delivered dose released in the plateau region. In this way nominal and delivered dose (it can fluctuate day by day) were obtained: the delivered dose correspondent to 1 Gy was 0.991 Gy.
2. Run the film background acquisition on the CCD camera for a time

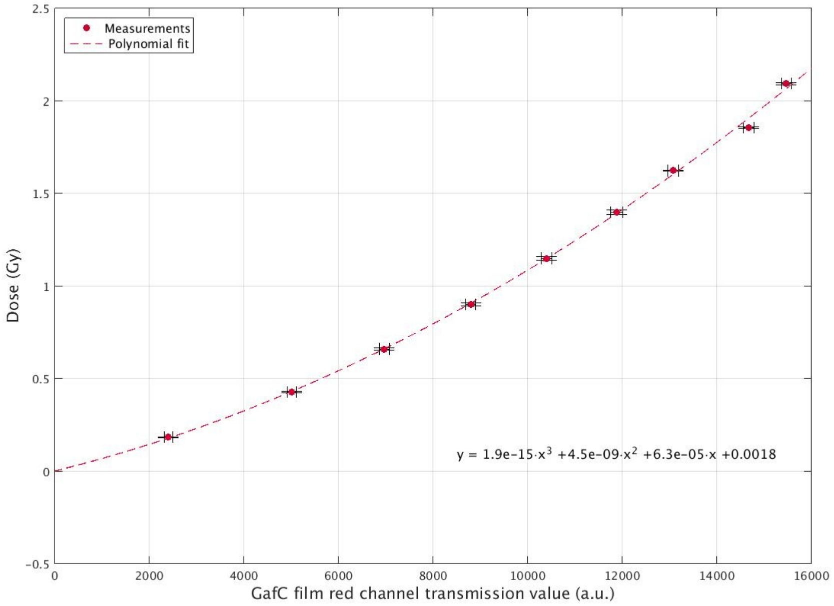

Figure 4.12: Calibration curve related to the batch of radiochromic films used for the measurements. The x-axes is the difference between the mean of the background and the mean red channel value of the irradiated field, while the y-axes represents the real dose applied.

corresponding to the field delivery. Subsequently apply the same steering file used before, inserting layers of plexiglass to get water-equivalent depth needed to measure in the plateau region. In this way, using the additional point (0,0) for the linear interpolation, the light output of the CCD camera (background subtracted) per dose calibration is found.

3. Generate steering files of mean energy matched to fields used for the further deliveries, with 6-8 nominal dose levels (25, 50, 75, 100, 125, 150, 175, 225 cGy), and apply them to the CCD camera. In this way, using the previous step and the measured light outputs, it is possible to find the real doses related to the nominal ones applied. The value of light output is evaluated as difference between the mean of the irradiated field and the mean of the background, while its error is the sum in quadrature of the two related standard deviations. Errors related to the real doses derive from the ones associated to the light outputs.
4. Scan the background of the Gafchromic films and then apply the same steering files also to them. Then, scan the films 24 hours after irradiation, in order to get the transmission values as subtraction of the mean red channel value of the irradiated field from the mean of the background. Since both values are averaged over many pixels, their

standard deviations have been used to estimate the error related to the transmission, adding them in quadrature.

5. Tabulate the transmissions of the films against the related delivered doses, thus fit these data points by a cubic polynomial. This give the continuous function (Figure 4.12) which could then be used to get the dose from an arbitrary darkening value.

The whole calibration procedure has to be performed for each box of films separately since films of different boxes show slight variations in their response to radiation. Since all films used in the measurements were from the same film batch, only one calibration curve has been derived. Furthermore, the result of the calibration is reliable within six months after the procedure.

Quenching correction

It is well-known that radiochromic films are affected by quenching, namely, by an under-response in the high-LET regime around the Bragg peak. Assuming that dY/dx is the darkening per unit length for the film, e is the efficiency and dE/dx is the proton stopping power, Birk's empirical formula for the quenching effect gives [Birks, 1964], [Torrisi, 2000]:

$$\frac{dY}{dx} = \frac{e}{1 + q \cdot \frac{dE}{dx}} \cdot \frac{dE}{dx} \tag{4.6}$$

where q is the quenching factor. This equation can be approximated in terms of doses in:

$$D_q(x) = \frac{e}{1 + q \cdot D(x)} \cdot D(x) \tag{4.7}$$

where D and D_q are the real and quenched doses respectively.

To determine the quenching quantitatively, depth-dose profiles of three mono-energetic pencil beams were measured with the films and compared with the related depth-dose profiles measured with a plane-parallel ionization chamber (Figure 4.13). The energies investigated are 80 MeV, 120 MeV and 150 MeV. By a least square fit, the parameter q was found for the three proton energies, while the efficiency e was extrapolated by imposing the entrance dose in the plateau to be equal in both real and quenched cases. Subsequently, the parameters have been interpolated in order to find q and e for each possible tune. In order to take into account the quenching effect of the Gafchromic films EBT3 in the further analysis, quenched depth-dose profiles have been evaluated from the tabulated ones using the quenching correction.

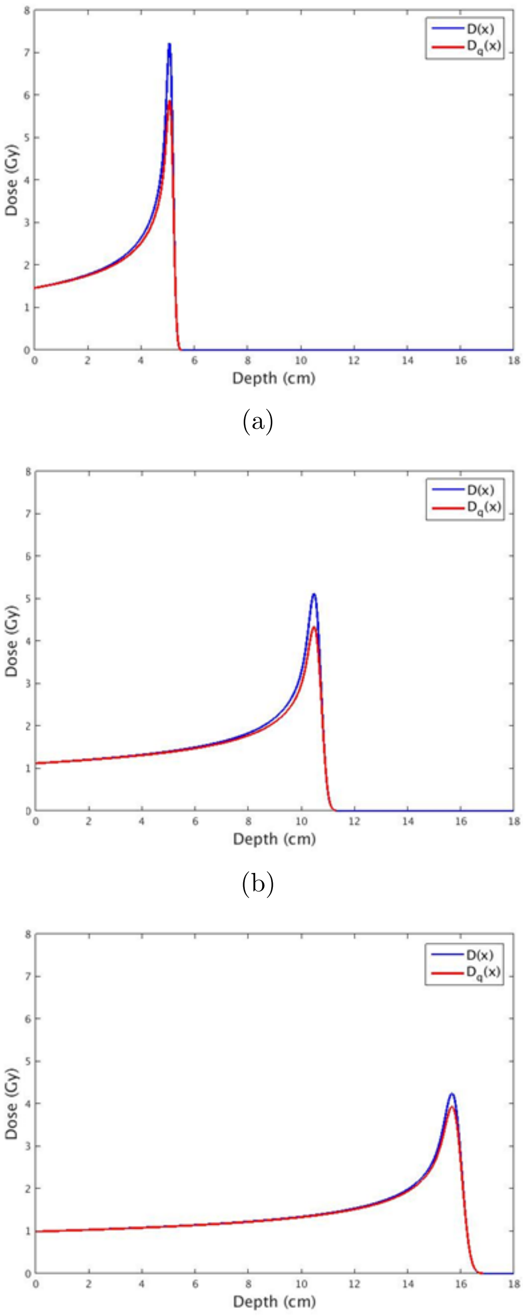

(a)

(b)

(c)

Figure 4.13: Depth-dose profiles of three mono-energetic pencil beams of 80 MeV (a), 120 MeV (b) and 150 MeV (c), measured with both films ($D_q(x)$) and plane-parallel ionization chamber ($D(x)$).

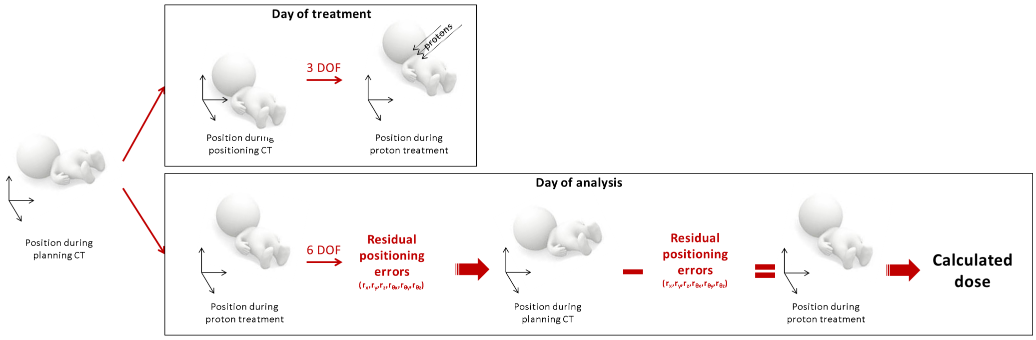

Figure 4.14: Schematic representation of the 3D-3D match used for taking into account residual positioning errors encountered during measurements.

2.6 3D-3D match

The entire process regarding the correction of positioning errors is represented in Figure 4.14.

As previously mentioned, the phantom CT acquisitions were performed in KSB. A shift of the CT cube imported in the TPS was necessary to guarantee correspondence between CT position and treatment position. Positioning set-up errors of the phantom were corrected by daily image guidance procedure, just like for real patients. Thus, at the treatment day, another CT was acquired before the delivery (one for each plan), using the in-room CT of Gantry 2. In this acquisition the phantom was not perfectly in the same position of the planning CT, due to intrinsic misplacement during the immobilization on the couch. Therefore, in order to ensure the correct delivery, a 3D-3D match with 3 degrees of freedom (DoF) was performed between the planning CT and the positioning CT using the in-house software *r33* [Fattori et al, 2015]. The three extracted parameters where then applied to the couch to compensate phantom misalignment. Subsequently, the plan was delivered. However, using 3 DoF permits to adjust translational set-up errors, while re due to residual rotations are not considered. This means that if these rotational discrepancies are not negligible, the phantom (and also the real patient) must be repositioned and another position CT is acquired.

To further reduce the errors derived by residual rotations, a 6 DoF 3D-3D match was performed between the planning and daily CT corrected based on the translational offset. The six extracted parameters were then applied to the planning CT, to mimic the delivery set-up. The nominal plan was then recalculated on this planning CT (with residual shifts and rotations) as at the delivery.

2.7 Extraction of the calculated dose

The calculated dose distributions for each delivered treatment plan, to be compared with measurements, has been evaluated using the in-house software *DoseCalc* [Meier et al, 2015]. With this tool, three effects have been considered during the calculation:

- Residual positioning errors.
  The CT used for the calculation is the planning CT corrected for residual positioning errors, as explained in the previous section.
- Daily machine dependent uncertainties.
  The resultant 3D Bragg peak fluence map resulting from the optimization done by the TPS needs to be converted into machine readable files and then correctly interpreted and delivered by the treatment machine. Both of these steps are potential sources of errors, especially given the complexity of the individual fields and many dynamic effects, such as random noise during delivery due to magnet hysteresis and current fluctuations [Meier et al, 2015]. For instance, at the PSI Gantry 2, the relative and absolute spatial accuracy of each pencil beam needs to be substantially improved through the use of spot specific positional offsets, obtained from an initial delivery of each field in an approach called “teaching” [Bula et al, 2013]. For this reason, the actually delivered spot positions can vary from the planned positions of up to a millimeter. At PSI, the so-called Therapy Control System (TCS) manages the delivery. It consists of two independent computer systems: Therapy Delivery System (TDS) and Therapy Verification System (TVS). The first one actively steers the delivery by setting the beam energy, sweeper magnet currents and switching the beam on and off. The latter one, instead, uses independent monitors and detectors to assure that the TDS has functioned properly, interrupting the treatment if any of its measured values lies outside defined tolerances. All such on-line measurements are performed on a pencil beam basis and are then logged in the so called “delivery log file”. Dose calculations based on these files can provide a valuable method for reconstructing the delivered dose to the patient, since these online checks and measurements can be considered as a form of entrance dosimetry [Li et al, 2013], [Scandurra et al, 2016]. For these reasons, the calculation with *DoseCalc* was based on log files analysis.
- Quenching effect.
  To take into account the quenching effect of Gafchromic films EBT3, quenching modified depth-dose profiles have been used for the calcu-

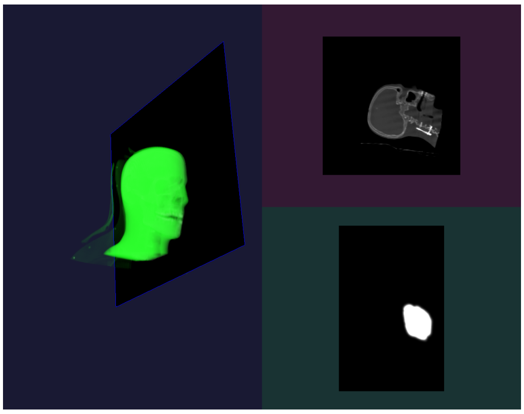

Figure 4.15: Screenshot of the in-house software Slice, necessary to select one arbitrary plane of the 3D dose distribution extracted from the TPS.

lation. It must be noticed that the correction was applied to the calculated dose distributions, and not to the measured ones. This can be explained by the fact that quenching is different along the depth-dose profile and thus it cannot be applied to measured dose. In fact, it is not a scaling factor since the under-response in only present at the Bragg peak.

From 3D dose distributions calculated with *DoseCalc*, 2D profiles correspondent to the three planes where the films were positioned were then extracted using the in-house software *Slice*. This tool, after requiring as input the related CT and dose distribution, permits to actively change both direction and angle of the considered plane by clicking inside it in the interactive 3D reconstruction (Figure 4.15).

2.8 Data analysis

In order to evaluate the different options coming to help dealing with metal artifacts, we compared the agreement between calculated and measured proton dose distributions for each approach. To do that, a MATLAB algorithm has been developed, which can be summarized as follows:

- Load measured and calculated 2D dose distributions.
- The calculated dose is normalized to 100%, which corresponds in the plan to 2 Gy(RBE). Physical delivered dose is then 1.8182 Gy, assuming RBE=1.1 for protons [Paganetti, 2011].
- Calculated and measured dose present different resolutions, respectively of 0.1953125 cm x 0.2 cm and 0.03524 cm x 0.03524 cm. For

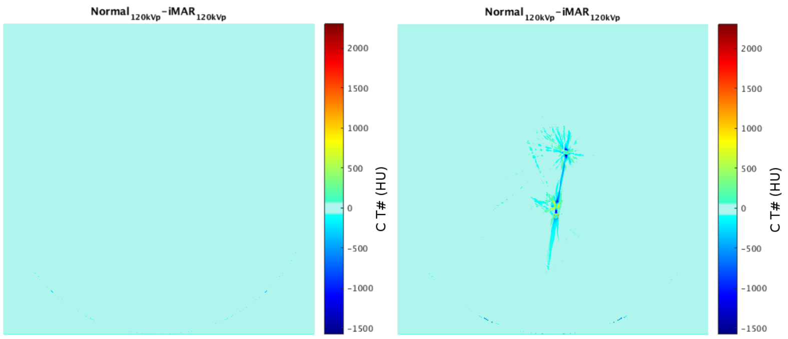

(a) (b)

Figure 4.16: Differences between CT images without (called normal) and with iMAR of the anthropomorphic head phantom. In (a) a slice without metal artifacts is considered, while (b) refers to the slice shown in Figure 4.3.

this reason, we up-sampled the calculated proton dose distribution to the same pixel size of the measured one.

- Manual registration is performed through rigid transformations, of the calculated dose on the measured one.
- The outside region of the images is removed.

3 Results

3.1 Inspection of iMAR and SAFIRE

The initial doubt concerning the exploited algorithms, especially iMAR, was their effect on the HUs of the image in the regions not affected by metal artifacts. For this reason their impact on CT images has been analyzed.

First of all we studied in detail the effect of iMAR on CT images. For each of the four energies employed during the acquisitions of SECT, the difference between normal and iMAR 3D images has been evaluated, together with its gray level histogram. Furthermore, the gray level histograms related to each CT have been superimposed, in order to analyze the main differences. Some of their peaks have been studied more precisely, in terms of mean value and standard deviation. The results are reported for the anthropomorphic head phantom Charlie only (Figures A.5, A.6, A.7, A.8), however they can be generalized for the other phantoms. The first consideration is that iMAR is affecting only those voxels belonging to metal artifacts, whereas the others are not modified (Figure 4.16). The gray-level histogram of the difference is really peaked around 0 and the two histograms related to the acquisitions

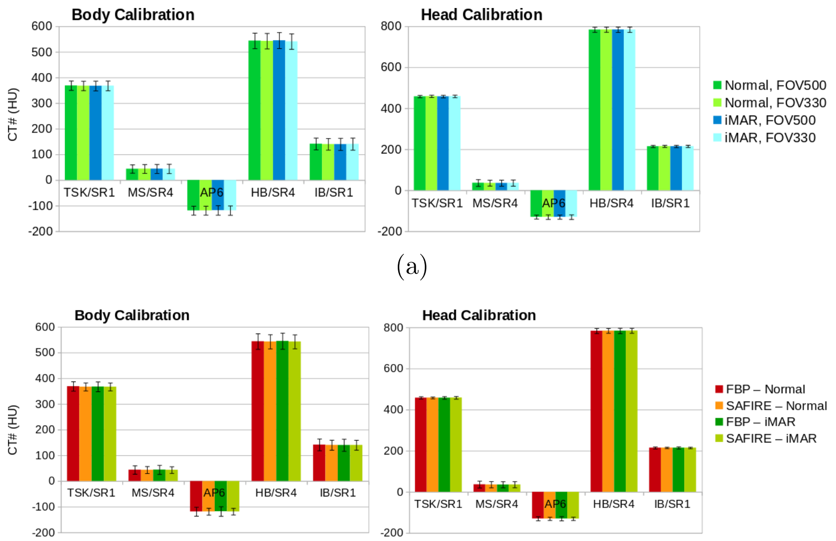

(a)

(b)

Figure 4.17: Mean CT numbers and related errors associated to the probes inserted in Body and Head phantoms, necessary for the stoichiometric calibration. In (a) acquisitions with and without iMAR, with different FOV are compared, while in (b) FBP and SAFIRE techniques are considered with and without iMAR.

with and without iMAR are quite superimposed, excluding any hypothesis of distortion caused by iMAR algorithm. The effect of iMAR is enhanced on the first peak, around 40 HU, associated to the spinal cord and brain tissues of the anthropomorphic phantom. In fact, the mean value is approximately the same (i.e. for 120 kVp it is 39.1 and 38.68 HU for the case without and with iMAR respectively) but the maximum value is smaller (i.e. for 120 kVp there is a difference around 2-3%) and the standard deviation is larger (i.e. for 120 kVp it is 18.7 and 19.2 HU for the case without and with iMAR respectively), so the peak is expanded. Moreover, this peak seems robust respect the change of the energy. Regarding the second peak, corresponding to the trabecular bone, it is very sensitive to the change of energy but unchanged by iMAR. Finally, it seems that iMAR introduces major differences using higher energies.

The second inspection concerns the impact of the algorithms on the stoichiometric calibration curve. To evaluate the HU values of tissue substitutes, samples have to be measured in order to generate the HU-RPSP calibration curves. This is performed by an in-house specific software , part of TPS. Subsequently, the curves are applied to the CT images of the anthropomorphic head phantom, in order to obtain its RPSP maps. Figure 4.17 shows

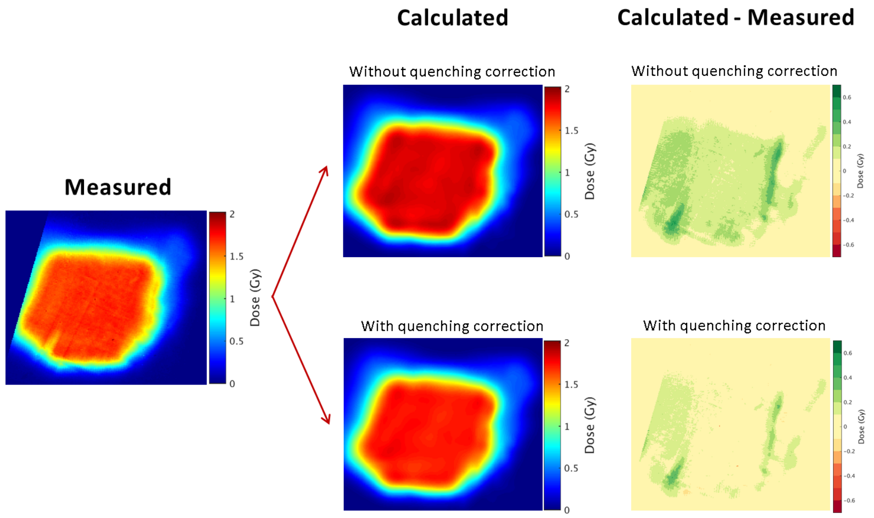

Figure 4.18: Example of Filtered Back Projection without correction of metal artifacts for 4-fields IMPT plan revealing the relevance of the quenching correction. All the other options present analogous results.

the HUs values of the calibration probes using iMAR and SAFIRE, with different FOV. It can clearly be seen that both FOV and iMAR/SAFIRE do not affect HU values. As regards the FOV, it doesn't influence the HU because the considered ROIs for the evaluation of the CT number are pretty homogeneous and therefore the border effect is not evident. The results for iMAR and SAFIRE confirm that these algorithms do not induce a shift or a change of the HU related to materials not eroded by the metal artifacts. Moreover, thanks to the iterative nature of SAFIRE, lower standard deviations are related to the mean values, since less noise is present in the images. Thanks to agreement shown for the CT numbers of the probes, only one curve has been used for the stoichiometric calibration.

3.2 Relevance of quenching correction

In a first step, calculated doses, which were compared to the measured ones, were computed based on depth-dose profiles including and neglecting quenching effect of radiochromic films. However, the relevance of the correction is quite evident. A representative example is shown in Figure 4.18 for a specific approach and plane. All other options present analogous results. As expected, if quenching effect is neglected, the calculated doses are higher than the measured ones. This can be seen also in terms of dose differences, on the right, where the introduction of the quenching corrections reduces the homogeneous under-response of the film.

3.3 Comparison of the approaches

The different approaches for artifacts correction have been studied for both IMPT and SFUD plans, by comparing measured and calculated dose distributions for the three planes in the anthropomorphic phantom. For this purpose, the comparison has to be performed only between calculated and measured. As calculated dose are derived from different optimizations, small differences in calculated dose for different approaches are expected and found.

4-fields IMPT plan

Figure A.9 shows measured and calculated dose distributions of the 4-fields IMPT plan, calculated on the CTs related to the seven different approaches, for all three measurements planes. On the measured dose distributions, projections of the metal implant are faintly visible. This effect is enhanced for planes 1 and 3, whereas for plane 2 it is not possible to recognize the entire shape of the metal but only in the lower left corner.

Dose differences between measured and calculated doses are represented in Figure A.10. Delivered over-dosed areas are depicted in red, while the under-dosed ones in green. Quantitative terms evaluations included percentage difference (*pd*) maps, as ratio between dose difference and related calculated dose for each voxel. We limited the analyzes to the 50% isodose (with 100% corresponding to 2 Gy(RBE) prescribed dose). From these maps we extracted four principal quantities, as reported in Table 4.6. First of all, maximum and minimum values of the percentage difference as indexes for the intensities of under- and over-dosed regions. Moreover, to indicate the extension of those regions, percentage areas have been evaluated as ratio between the area of pixel having percentage difference higher (lower) than +10% (-10%) and the total area of the 50% isodose:

$$A_{\pm 10} = \frac{Area_{pd \gtrless \pm 10\%}}{Area_{50\% isodose}} \, . \tag{4.8}$$

These parameters A_{+10} and A_{-10} denote the extension of the under- and over-dosed areas respectively.

Finally, we performed 2D gamma analyzes for dose distributions comparisons, as reported in Figure A.11 and Table 4.7 [Low et al, 1998]. In this way, regions where the dose difference and the Distance to Agreement (DTA, distance between a reference point and the nearest point in the compared dose distribution that exhibits the same dose) are simultaneously lower than a preselected criteria are identified. The measurement is used as reference information, while the calculated distribution is queried for comparison. The

		FBPu	**FBPm**	**FBPi**	**IRu**	**IRm**	**IRi**	**DE**
p1	$\boldsymbol{A}_{+10}$ **(%)**	10.9	12.0	14.2	24.8	18.2	18.5	8.8
	$\boldsymbol{A}_{-10}$ **(%)**	0.3	0.1	0.0	0.0	0.0	0.0	0.1
	Max (%)	32.6	34.1	38.4	43.1	41.0	43.1	36.8
	Min (%)	-17.2	-13.8	-7.7	-6.8	-9.4	-10.0	-11.8
p2	$\boldsymbol{A}_{+10}$ **(%)**	12.0	11.0	10.4	10.1	11.5	8.5	6.8
	$\boldsymbol{A}_{-10}$ **(%)**	0.0	0.1	0.0	0.0	0.0	0.0	0.3
	Max (%)	26.7	30.3	22.7	24.8	25.8	23.2	24.2
	Min (%)	-8.5	-13.9	-10.5	-8.0	-6.3	-9.6	-15.5
p3	$\boldsymbol{A}_{+10}$ **(%)**	22.5	58.9	41.7	23.5	41.6	26.8	35.7
	$\boldsymbol{A}_{-10}$ **(%)**	2.3	0.0	0.3	3.1	0.0	1.7	3.3
	Max (%)	31.2	39.7	34.8	31.7	38.4	31.2	32.1
	Min (%)	-22.6	-4.8	-12.5	-18.4	-9.9	-17.5	-21.0

Table 4.6: Quantitative analyzes of percentage difference on the 50% isodose for the seven approaches investigated with 4-fields IMPT plan: percentage areas having percentage difference higher (lower) than 10% (-10%) A_{10} (A_{-10})*, maximum and minimum values of percentage difference.*

dose-difference criterion ΔD_M and the DTA criterion Δd_M were chosen for our study equal to 3% and 3 mm respectively. Denoting with $D_m(\boldsymbol{r}_m)$ and $D_c(\boldsymbol{r}_c)$ measured and calculated doses in the point $\boldsymbol{r}_m$ and $\boldsymbol{r}_c$, it is possible to define a quality index γ for the measurement point $\boldsymbol{r}_m$ as:

$$\gamma(\boldsymbol{r}_m) = min\{\Gamma(\boldsymbol{r}_m, \boldsymbol{r}_c)\}_{\forall \boldsymbol{r}_c} \tag{4.9}$$

where:

$$\Gamma(\boldsymbol{r}_m, \boldsymbol{r}_c) = \left(\frac{|\boldsymbol{r}_c - \boldsymbol{r}_m|^2}{\Delta d_M^2} + \frac{(D_c(\boldsymbol{r}_c) - D_m(\boldsymbol{r}_m))^2}{\Delta D_M^2} \right)^{1/2} . \tag{4.10}$$

The pass-fail threshold is 1: if $\gamma(\boldsymbol{r}_m) \leq 1$ the correspondence between measured and calculated dose is within the specified acceptance, otherwise it fails.

From these results, it can be seen that lower differences between calculated and measured dose distributions are related to the Dual Energy approach, although the over-dosage in plane 3 is a bit broader than other methods, but not too intense. In general, it can be seen that the majority part of the differences is located in plane 3 and plane 1, in regions of gradients. Moreover, in plane 1 there is a cold spot of under-dosage in the lower part of the metal implant. Since present for all the approaches, this could be related to the inaccurate calculation of the dose in presence of sharp interfaces created by the metal. The three methods investigated with SAFIRE proved to be worse for plane 1 than the related ones with FBP, while planes 2 and 3 are comparable or even slightly better.

	p1	p2	p3
FBPu	93%	89%	89%
FBPm	87%	88%	52%
FBPi	78%	90%	75%
IRu	63%	90%	89%
IRm	71%	91%	76%
IRi	71%	92%	86%
DE	94%	93%	79%

Table 4.7: Percentage of points satisfying the gamma 3%/3mm calculated on the 50% isodose for the seven approaches investigated with 4-fields IMPT plan.

1-field SFUD plan

Figure A.12 shows measured and calculated dose distributions of the 1-field SFUD plan, calculated on the CTs related to the five different approaches, for all three measurements planes. On the measured dose distributions, clear projections of the metal implant are visible on the plane 1, since it is crossed by the beam after passing through the metal implant. Moreover, unlike the IMPT plan, the effect of the thermoplastic mask used for immobilizing the phantom is quite clear on planes 2 and 3, showing the regular pattern with dots on both measured doses and dose differences. This effect is enhanced as compared to the clinical cases, due to the fact that the entire fraction dose of 2 Gy(RBE) is delivered by a single field. As shown from the 4-fields plan, the presence of the mask can be neglected for multiple field arrangement.

Dose differences are represented in Figure A.13 and, as for the IMPT, over- and under-dosages are respectively shown in red and green. The quantitative analyzes regarding percentage differences is reported in Table 4.8.

Results regarding gamma analyzes for comparisons between measured and calculated dose distributions are reported in Figure A.14 and Table 4.9). As for IMPT, dose-difference and DTA criteria were chosen 3% and 3 mm respectively.

Also from these results, DE approach confirm its potential in achieving the better agreement between calculated and measured dose distributions. Moreover, in this case, the method exploiting SAFIRE with iMAR is showing low dose differences too. In addition, a broad and intense over-dosage is present in plane 1 for the FBP uncorrected, then reduced in the other considered cases, especially in the manually corrected ones. Close to it, an under-dosage in the lower part of the metal implant can be seen, as for the IMPT plan.

		FBPu	**IRu**	**IRm**	**IRi**	**DE**
p1	**A_{+10} (%)**	16.2	13.3	13.0	10.4	12.7
	A_{-10} (%)	0.8	0.9	0.2	0.9	2.1
	Max (%)	70.7	74.5	86.6	79.9	63.7
	Min (%)	-46.0	-38.0	-18.9	-28.7	-39.4
p2	**A_{+10} (%)**	5.4	11.1	12.6	20.0	10.7
	A_{-10} (%)	0.1	0.0	0.0	0.0	0.0
	Max (%)	30.7	25.9	36.1	28.9	25.4
	Min (%)	-13.7	-5.9	-3.8	-1.2	-6.9
p3	**A_{+10} (%)**	56.0	81.2	72.7	9.6	10.7
	A_{-10} (%)	0.0	0.0	0.0	0.0	0.0
	Max (%)	29.3	30.0	30.3	25.9	22.6
	Min (%)	0.0	0.0	0.0	-10.8	-6.6

Table 4.8: Quantitative analyzes of percentage difference on the 50% isodose for the five approaches investigated with 1-field SFUD plan: percentage areas having percentage difference higher (lower) than 10% (-10%) A_{10} (A_{-10}), maximum and minimum values of percentage difference.

	p1	**p2**	**p3**
FBPu	92%	99%	41%
IRu	98%	71%	30%
IRm	98%	68%	30%
IRi	99%	50%	100%
DE	98%	80%	99%

Table 4.9: Percentage of points satisfying the gamma 3%/3mm calculated on the 50% isodose for the five approaches investigated with 1-field SFUD plan.

4 Discussion and Outlook

In this study, we assessed the performance of different approaches based on imaging, in order to help dealing with CT metal artifacts for proton therapy treatments of patients with metal implants. To do that, we compared calculated and measured dose distributions on realistic plans delivered to an anthropomorphic head phantom with titanium rods implanted in the neck.

First of all, we studied the consistency of HUs values for the different metal artifact algorithms, such as iMAR and SAFIRE. As no significant HU differences were found, a single HU to RPSP curve was used for all the six SECT cases. However, iMAR differences are larger at higher energies; this can be related to the fact that scanning at higher voltages results in a harder X-ray beam, and thus less beam hardening artifacts. In addition, artifacts are less at higher energies, due to X-rays beam penetration. Therefore, for high energies, lower artifacts are present, thus implying an easier removal of them by iMAR reconstruction and then higher histogram differences.

Furthermore, the quenching correction for Gafchromic films EBT3 proved to be essential in order to have a fair comparison between measurements and calculations in absolute dose.

The seven investigated methods give good results in terms of dosimetry accuracy. In general, the manual correction is associated to a broader and more intense under-dosage, while the over-dosage is smaller respect to the other methods. This can be due to the choice of the mean HU used to fill this region, too lower than the actual CT number related to the defined area. This is a real limitation of this approach, especially for real patients as it has intrinsic approximations (value of HU) and uncertainties (ROI delineation). Time required is also significant (6-8 hours). No correction of the artifacts, together with iMAR and DE, generally result in more broader and intense over-dosage. That effect can be instead explained looking at a typical metal artifact, composed by a combination of both dark and white stripes. The first ones have HUs similar to air, while the latter ones mimic dense objects, such as implants and teeth. In this way, depending on the field direction, the presence of white stripes can lead to a significant over-estimation of tissue water equivalent thickness, implying over-shooting in distal tissue. This over-dosage can be slightly seen also in iMAR and DE approaches, since during the process of reducing of the artifact the false dark and white information could remain in some voxels of the output image.

However, no correcting the artifact is not a reliable approach for clinical purposes [Dietlicher et al, 2014]. For example, depending on the shape of the artifact and on the delivered plan, it could be possible for the beam to cross the artifact along its entire extension. In this case planned and delivered doses would be significantly different. For this reason, it can be concluded that DE approach is the best choice, based on our results. This is mainly due to the related RPSP estimation, which is based on a physical model. We used DECT based on FBP, however with SAFIRE the results could be further improve. In fact, it has been proved that standard deviations for ρ_e and Z_{eff} are reduced up to a factor 2 when using SAFIRE instead of FBP, improving as a consequence also the dose calculation accuracy [Landry et al, 2015].

Projections of the metal implant and of the thermoplastic mask are visible on the measured doses, while absent on the calculated ones. One of the reasons is the calculated grid as compared to measurement resolution. However, using plan with multiple fields they become faintly perceptible compared to a single field. The 4-fields IMPT plan was found to be also quite robust against the errors introduced by the titanium implants, even for the uncorrected approaches, whereas the single field exploited for the SFUD plan seemed to be more sensitive to metal artifacts inside the planning CT. This is mainly a result of the higher number of proton beams used. The use of multiple fields, as shown by [Albertini et al, 2011], is a good method to increase plan robustness. This has proven to be valid also when dealing with metal artifacts. The overall impact of dosimetric errors in the individual proton fields strictly depends on the design of the treatment plan, as already found by [Verburg and Seco, 2013]. Our results, therefore, do not show evidence for dosimetric inaccuracies in the treatment planning being a significant factor in the reduced tumor control of patients with titanium implants, which was instead reported by [Staab et al, 2011], [DeLaney et al, 2009].

It may be possible that differences between approaches are too small to be detected with the tools and methods we used, as they are included in the film measurements errors bars. For example, intrinsic uncertainties related to radiochromic films play an important role in the total error related to the measurement. For Gafchromic films EBT, the total 2-sigma dose uncertainty, including the fit uncertainty of the calibration curve, the variation in film response for different film sheets, the uniformity within the area and the noise in the scanned films was found 6% and 4% at 1 Gy and 5% and 3.5% at 2 Gy [Saur and Frengen, 2008]. Besides, the anthropomorphic phantom presents with limitations in handling (due for example to small air-gaps between the planes) which could not be avoided. Besides, the anthropomorphic phantom was scanned during the planning CT without radiochromic films inside and, secondly, it was not always easy to close properly the slices. The quenching correction has been established for each proton tune using an interpolation based on measurements done at three energies only, so a more accurate correction may improve the reference doses used for the comparison with the measured ones. Moreover, extremely sharp interfaces between soft-tissue and metal can degrade the accuracy of the dose calculation [Lomax, 2008]. Therefore, a Monte Carlo simulation may improve the prediction of the dose distribution in presence of heterogeneity. Another common uncertainty to all approaches could be related to the fact that the dimension of the metal inside the CT image appears to be larger than the real one [Elliott and Slakey, 2014]. Another limitation concerns the up-sampling of the calculated dose to the higher resolution of the measured one, done for having a sufficient statistics related to the analyzes.

Finally, it must also be noticed that this study concerns an anthropomorphic phantom, therefore different results could be found for real patients due to the complexity of the human body and to the different amount and extension of metal artifacts.

Conclusions

In this thesis we investigated two major applications of Computed Tomography for proton therapy treatments. The first one aims at obtaining contrast enhanced images using DECT, to improve patient positioning. The second one analyses different imaging approaches, such as DECT and iterative methods of reconstruction, for dealing with artifacts, introduced in the planning CT due to the presence, after surgical operation, of metal stabilizing rods inside the patient.

We developed an algorithm to obtain bone-canceled and tumor-canceled images from 2D dual energy topograms. This tools proves to be useful for patient positioning, where the tumor is hidden behind the rib cage. In fact, the bone-canceled image enhances it and makes it visible. The two investigated methods (linear and logarithmic) give comparable results in terms of SDNR and image quality, but for segmenting the bone-canceled images the logarithmic one proved to be better. Therefore, this is the one used for the final implementation of the algorithm. The combination of low and high energies giving better performance for the used CT scanner is 80kVp/90mAs - 140kVp/28mAs. The method proved to be robust with respect to the choice of the ROIs, requiring only to select them inside the border of tissue of interest. However, the performance of the algorithm is strictly related to the characteristics of the target, especially its density and homogeneity. The feasibility study concerning the application of the algorithm to patient positioning seems to have been successful. Moreover, using the additional segmentation of the tumor on bone-canceled images, the algorithm might be used for patient positioning based on the tumor position, rather than bone anatomy only. Nevertheless, further research will be necessary. For a future application in the Center for Proton Therapy, real DECT scanner should be used for the acquisitions, instead of a double scanning using a single source CT, in order to exclude also motion artifacts.

In the second part of this work, we experimentally assessed the performance of different imaging approaches, by comparing their calculated and measured dose distributions. Moreover, we presented a first verification of

DECT-based RPSP evaluation based on anthropomorphic phantom. First of all, we proved that iMAR does not affect regions not belonging to the artifact, and both iMAR and SAFIRE do not require different stoichiometric calibration curves as long CT parameters are the same. During the analyses, residual positioning mismatch, machine delivery uncertainties, as well as Gafchromic films EBT3 quenching were taken into account. All the approaches seem to give good results in terms of dosimetry accuracy, with slightly worse results obtained with SAFIRE than with FBP. Moreover, manual correction is associated to a broader and more intense under-dosage, while no correction of the artifacts, together with iMAR and DE, has in general larger over-dosage. If on one side the results can be considered clinically comparable, not correcting the artifact is not a reliable approach. This is due to the not real information enclosed in the voxel of the artifact and, thus, depending on the shape of the artifact and on the delivered plan, it could be possible to deliver the beam directly along the artifact, thus resulting in quite substantial delivery uncertainty. Dual energy approach combined with iMAR proved to be the best one. In general, we saw that plans with multiple fields are more robust against the errors introduced by the metal implants than single field. However, it may be possible that differences between the approaches are not visible with the exploited experimental set-up, especially considering the common sources of errors related to the measurements. This includes for example intrinsic uncertainties related to radiochromic films, absence of film in the planning CT, difficult reproducibility of the set-up of the phantom, low accuracy in dose calculation across sharp interfaces and heterogeneity, larger size of the metal than the real one and up-sampling of the calculated dose to the higher resolution of the measured one.

To conclude, we achieved the desired goals of improving patient positioning using DECT and investigating different imaging approached for dealing with metal artifacts. The use of the contrast enhancement algorithm proved to reduce residual positioning errors. On the other hand, iMAR showed its clinical potential as an alternative method for metal artifact correction, especially if combined with DE approach.

Appendix

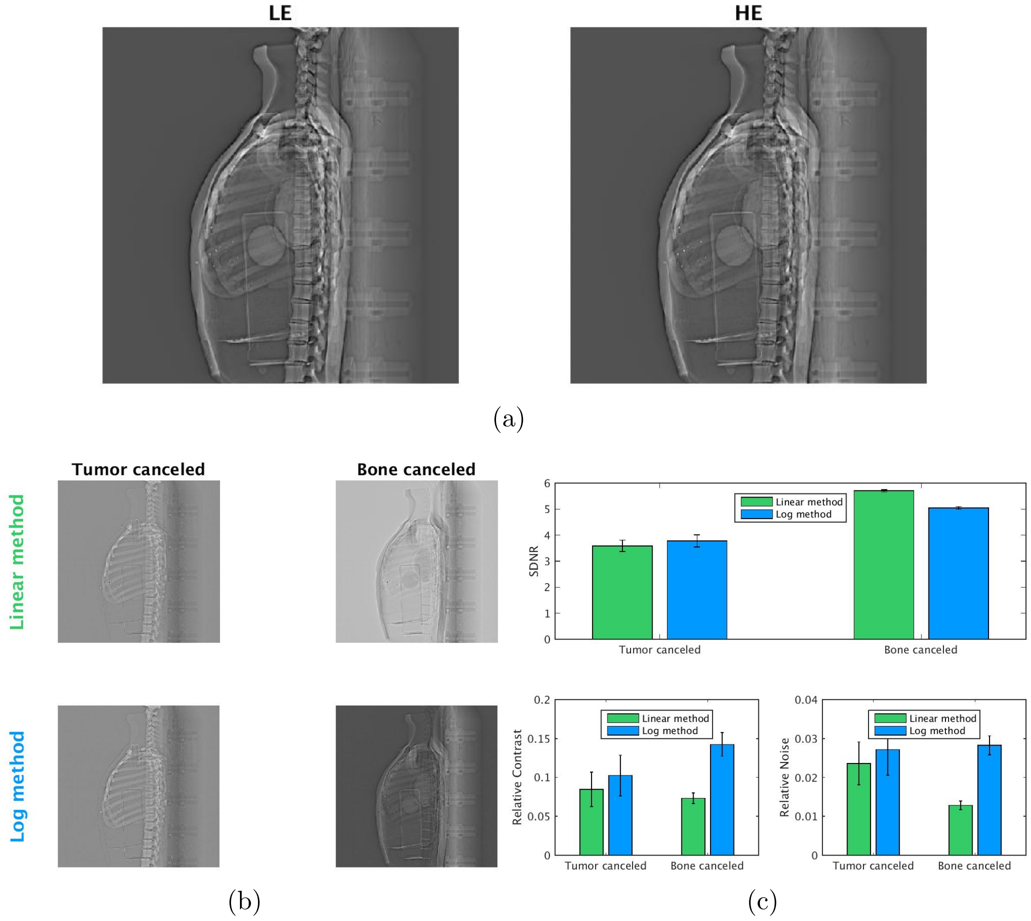

(a)

(b)

(c)

Figure A.1: Study made on the silicon tumor, LAT images. Acquired LE and HE images (a), output images (b) and related quality image analysis (c) are reported. Acquired LE and HE images (a), output images (b) and related quality image analysis (c) are reported.

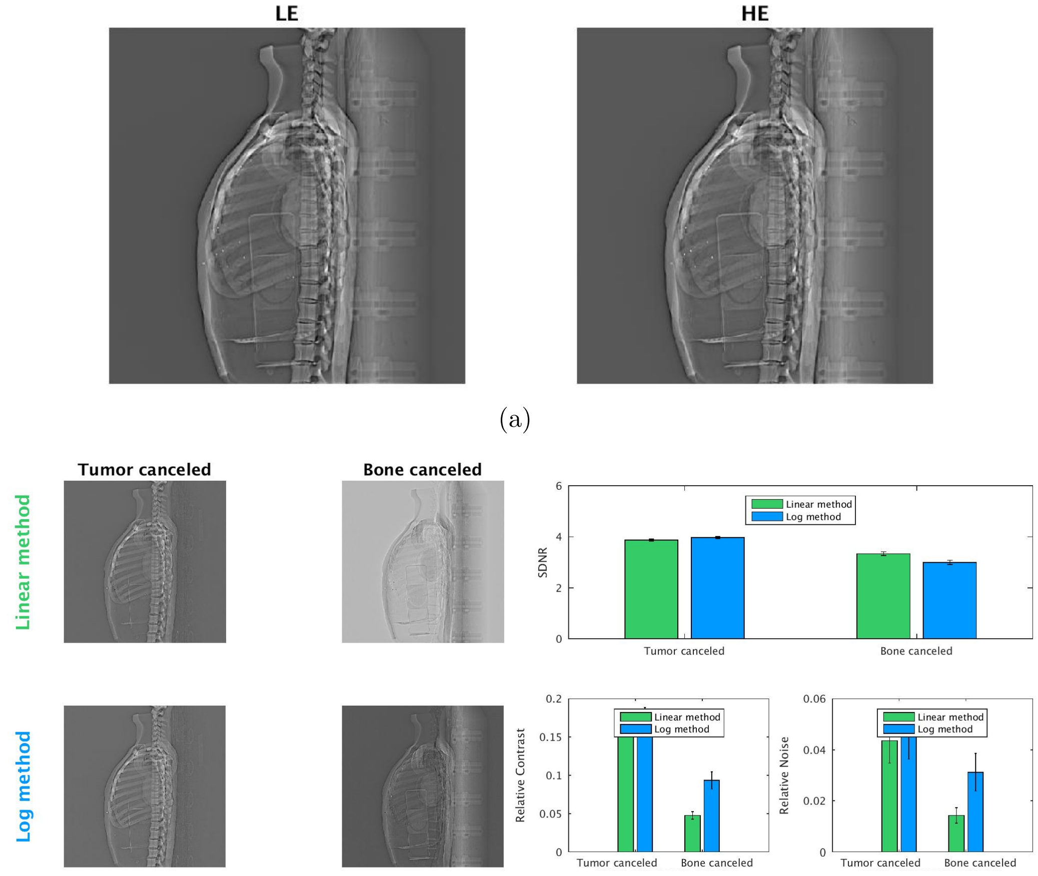

(a)

(b)

(c)

Figure A.2: Study made on the wood tumor, LAT images. Acquired LE and HE images (a), output images (b) and related quality image analysis (c) are reported. Acquired LE and HE images (a), output images (b) and related quality image analysis (c) are reported.

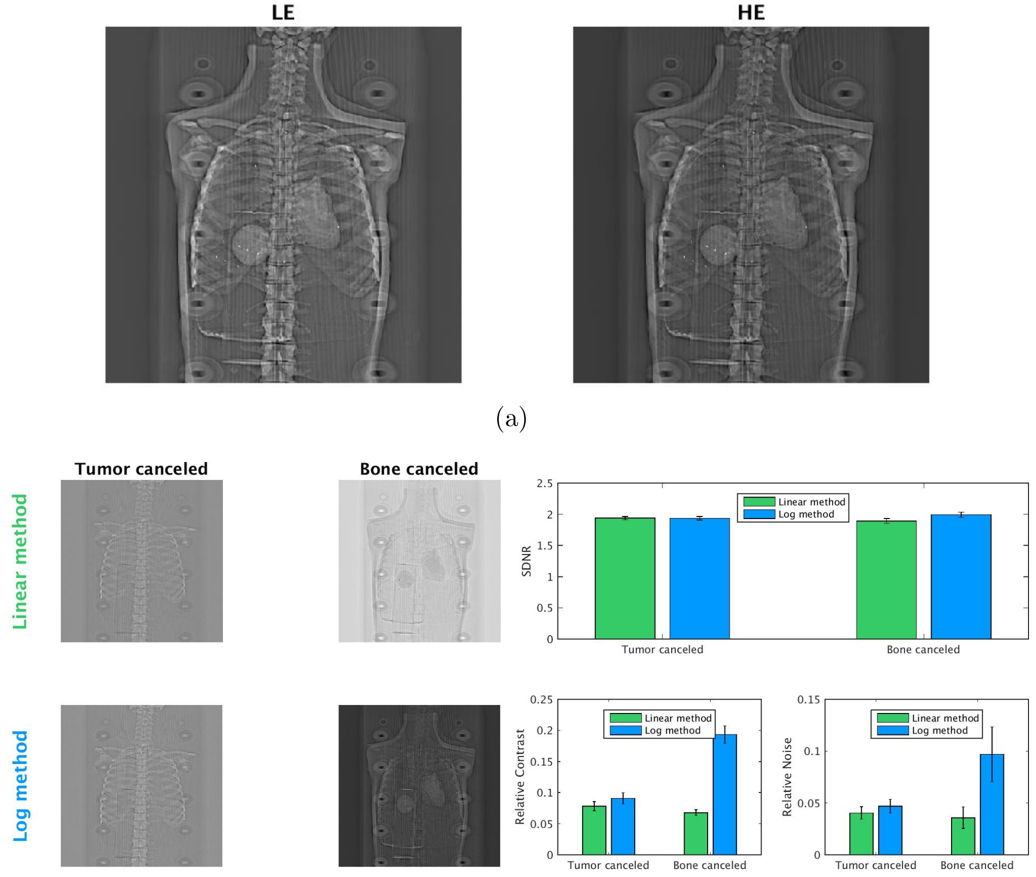

(a)

(b)

(c)

Figure A.3: Study made on the silicon tumor, AP images. Acquired LE and HE images (a), output images (b) and related quality image analysis (c) are reported. Acquired LE and HE images (a), output images (b) and related quality image analysis (c) are reported.

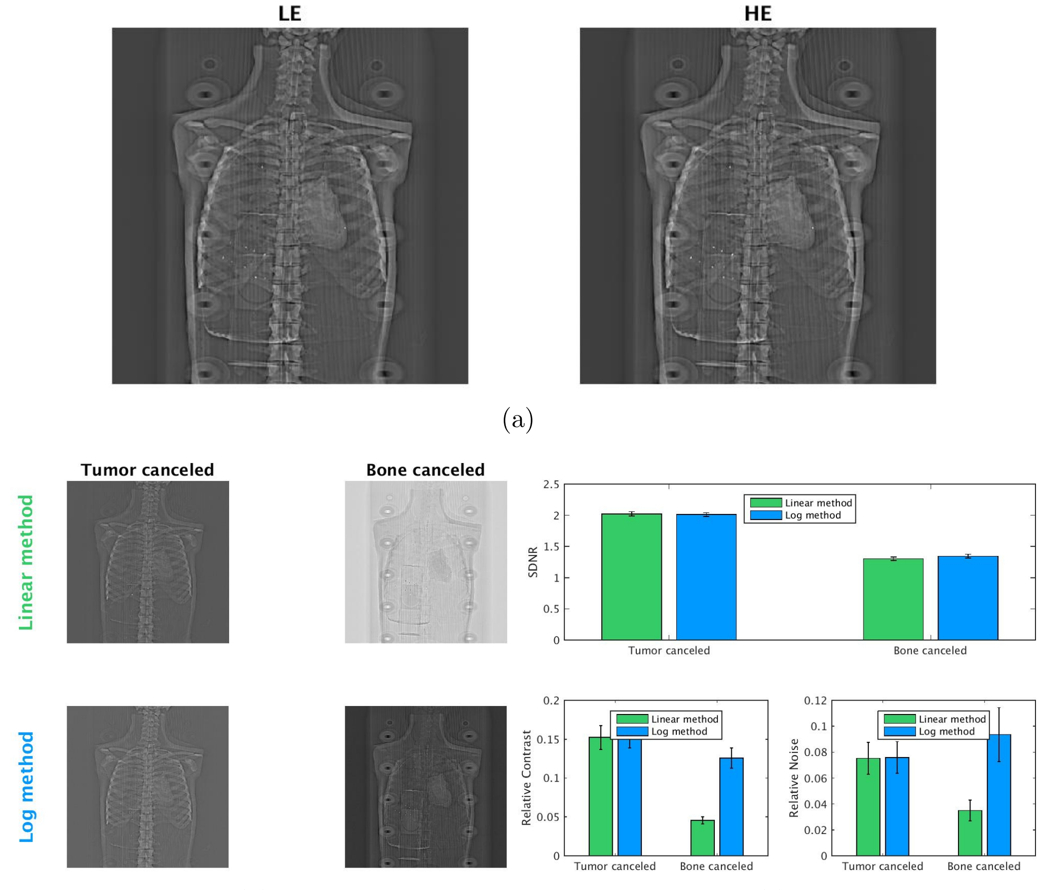

(a)

(b)

(c)

Figure A.4: Study made on the wood tumor, AP images. Acquired LE and HE images (a), output images (b) and related quality image analysis (c) are reported. Acquired LE and HE images (a), output images (b) and related quality image analysis (c) are reported.

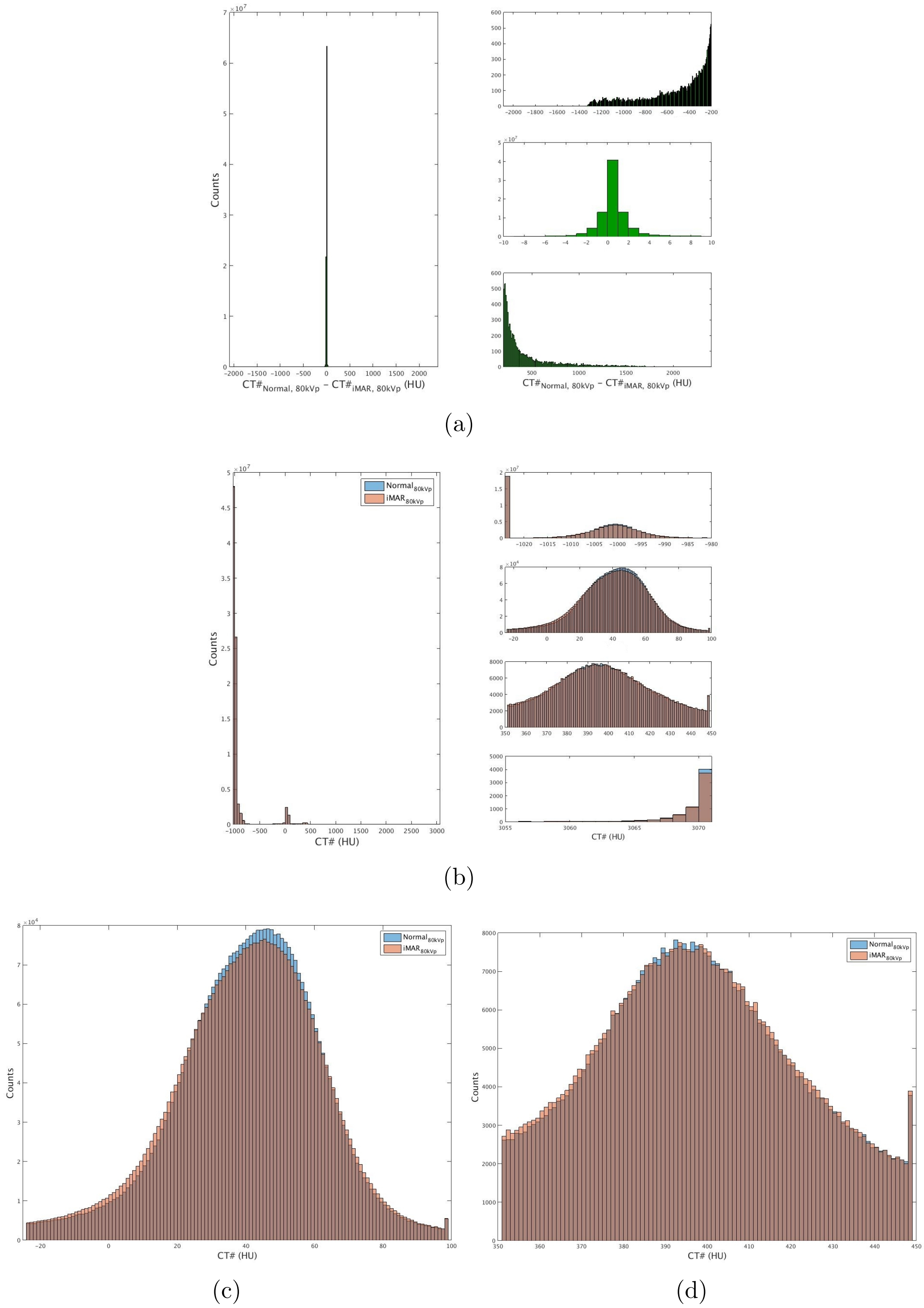

(a)

(b)

(c)

(d)

Figure A.5: Gray level histogram of the difference between the acquisitions with and without iMAR (a), histograms of each CT (b), with two major peaks (c, d) for 80 kVp.

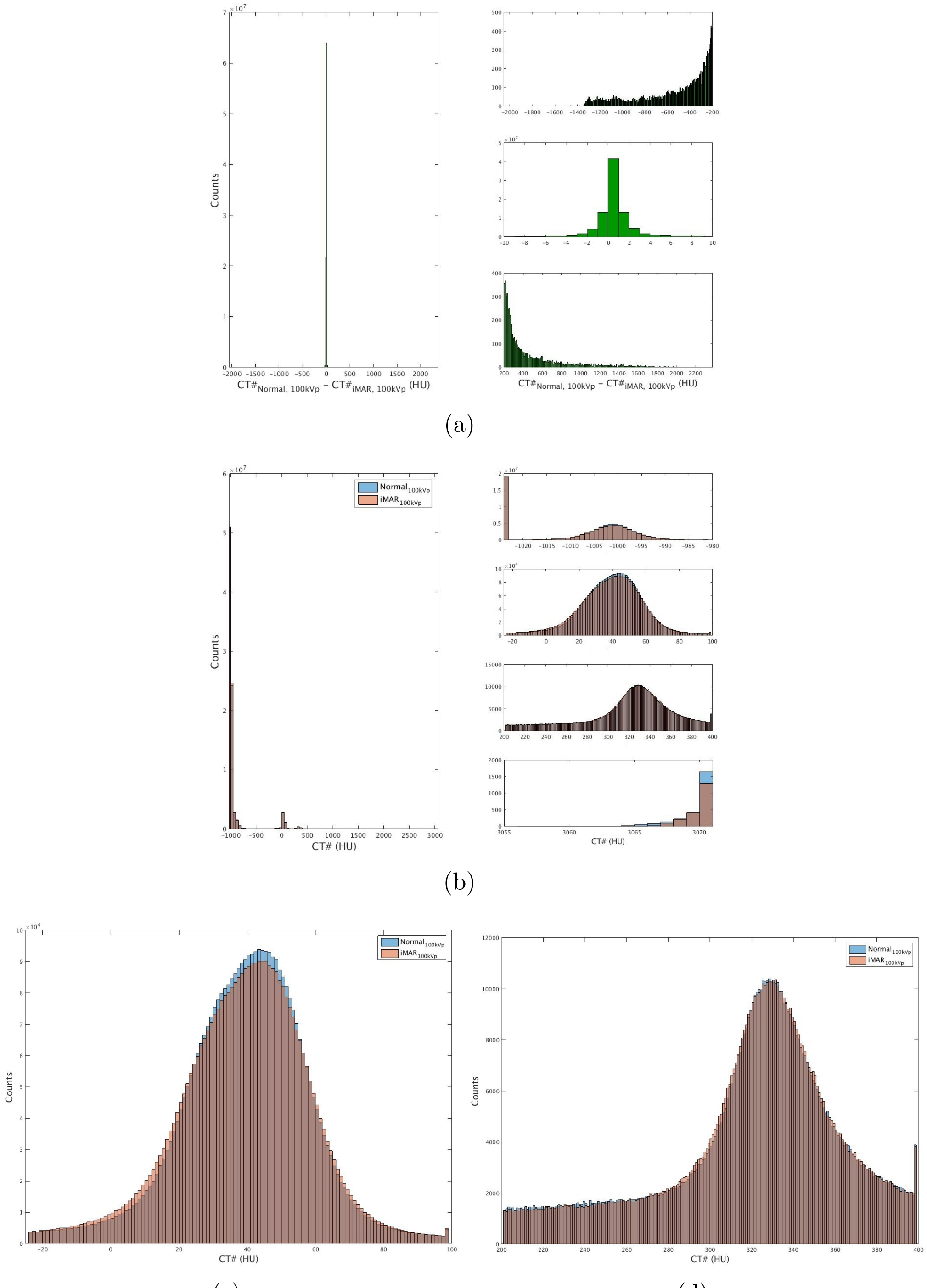

(a)

(b)

(c)

(d)

Figure A.6: Gray level histogram of the difference between the acquisitions with and without iMAR (a), histograms of each CT (b), with two major peaks (c, d) for 100 kVp.

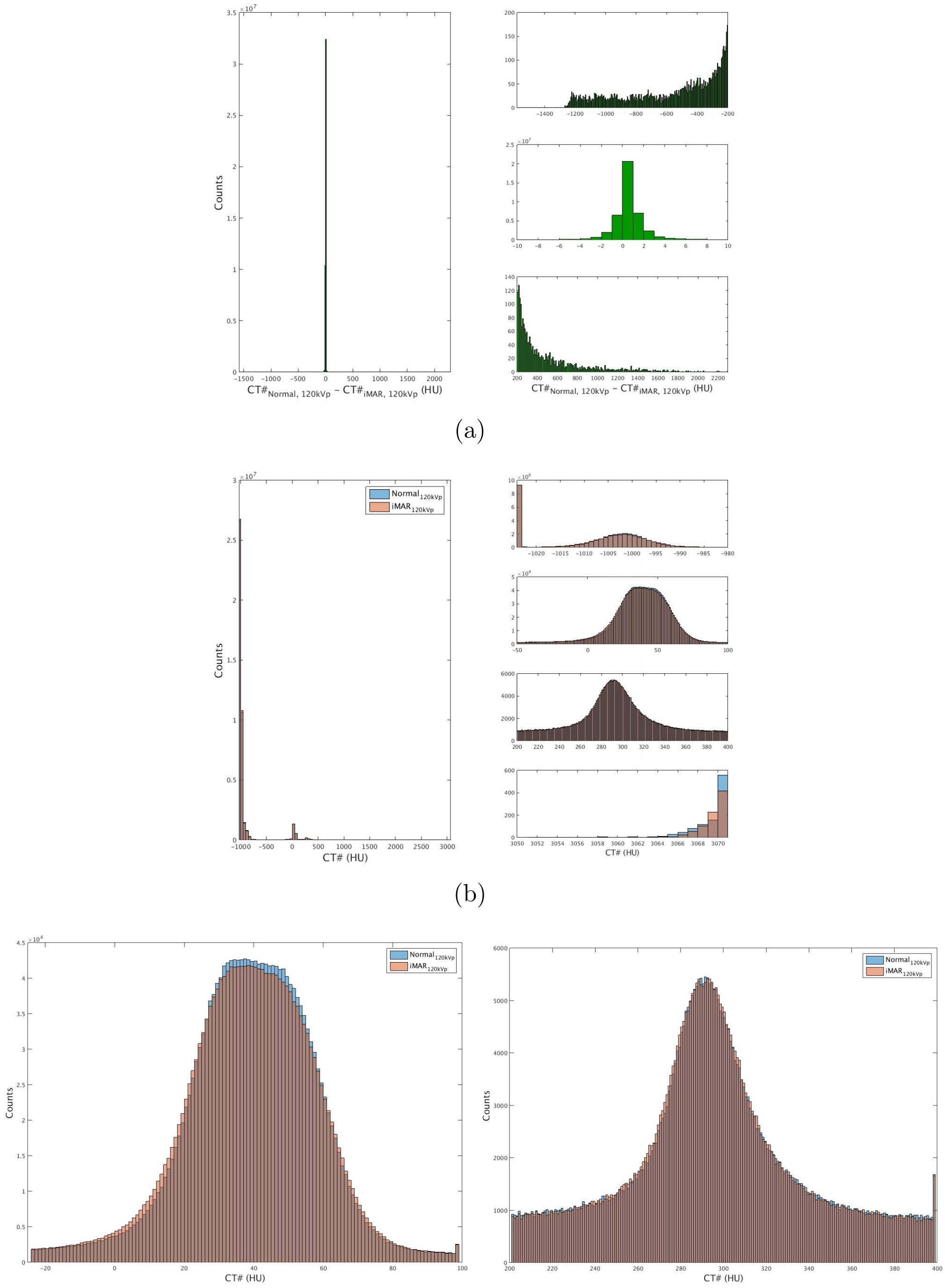

(a)

(b)

(c) (d)

Figure A.7: Gray level histogram of the difference between the acquisitions with and without iMAR (a), histograms of each CT (b), with two major peaks (c, d) for 120 kVp.

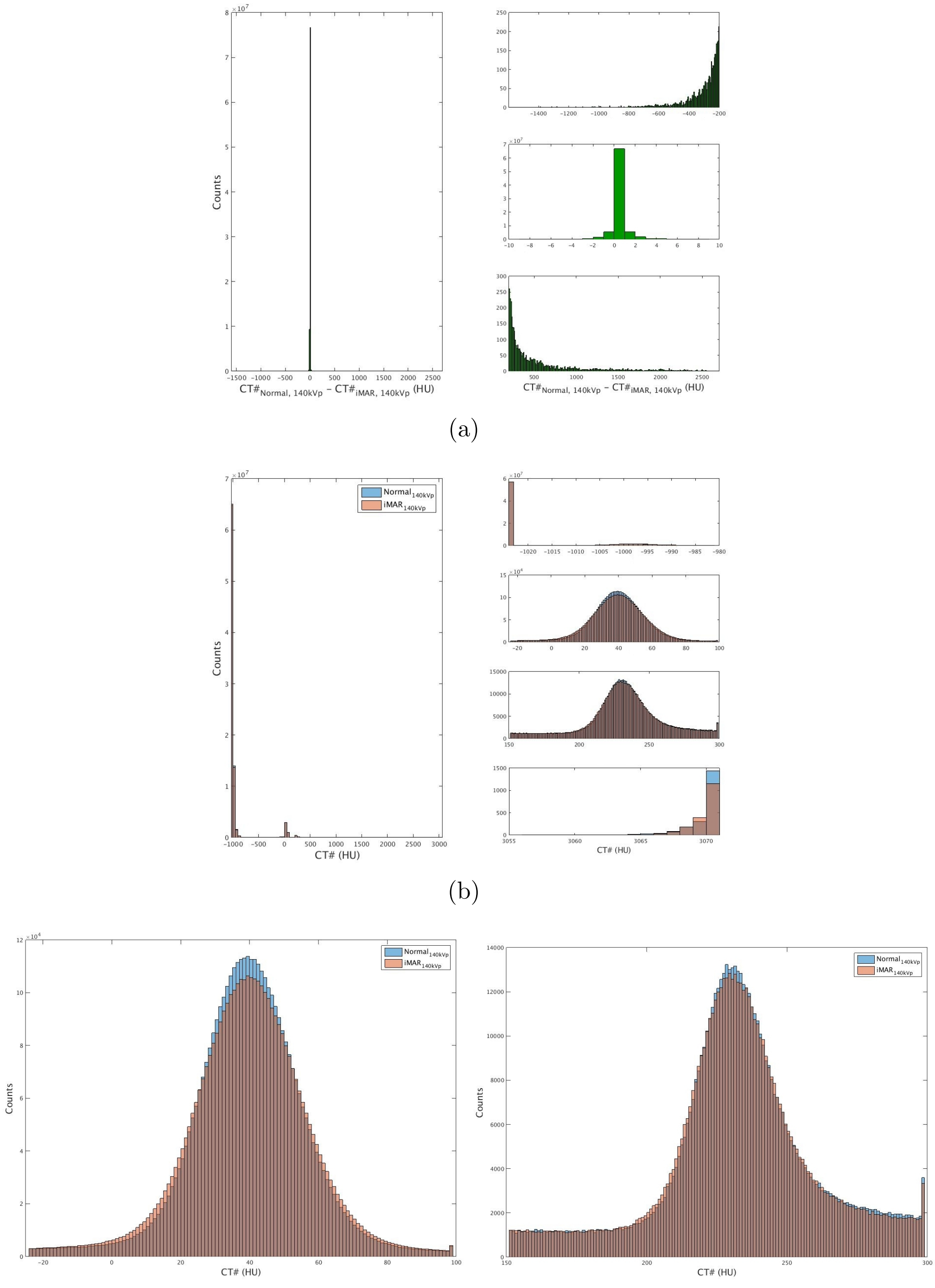

(a)

(b)

(c) (d)

Figure A.8: Gray level histogram of the difference between the acquisitions with and without iMAR (a), histograms of each CT (b), with two major peaks (c, d) for 140 kVp.

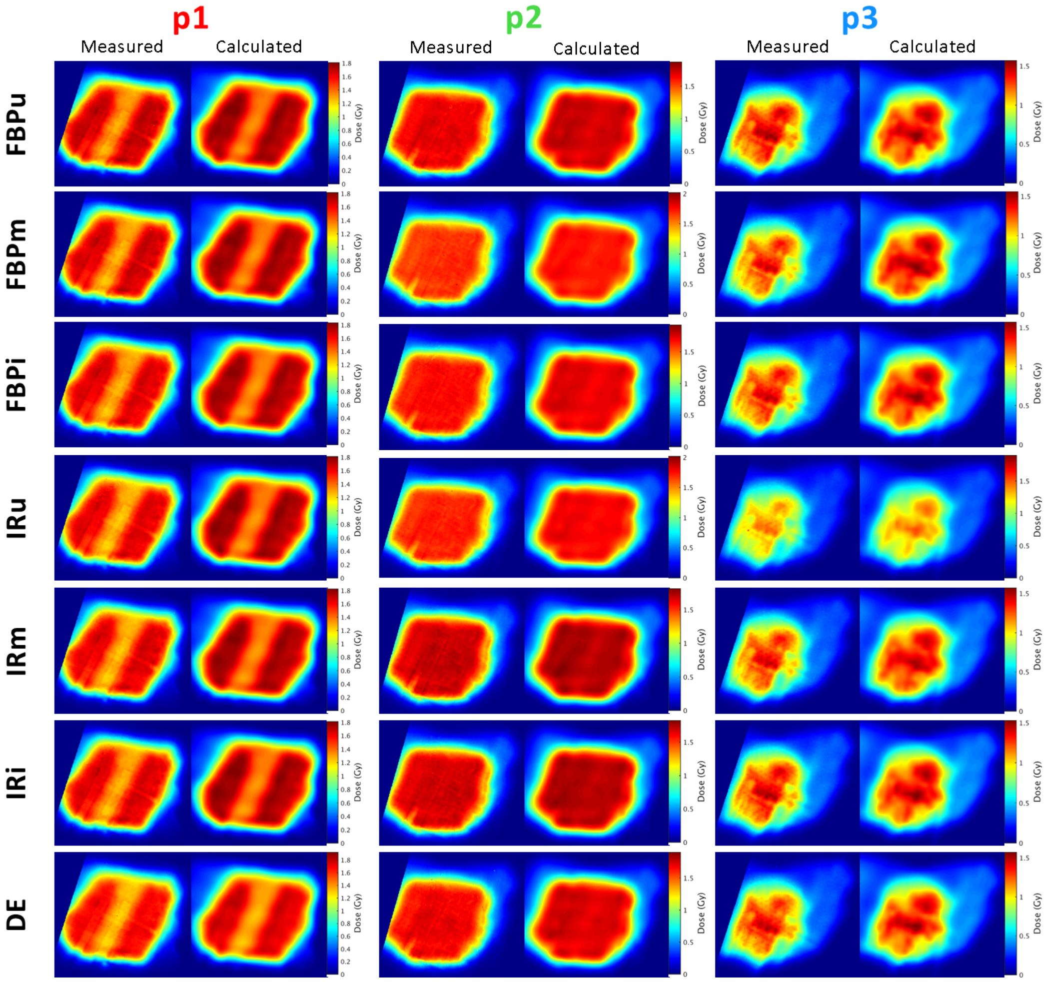

Figure A.9: Dose distributions (measured and calculated) obtained in the 4-fields IMPT plan for each approach and each plane.

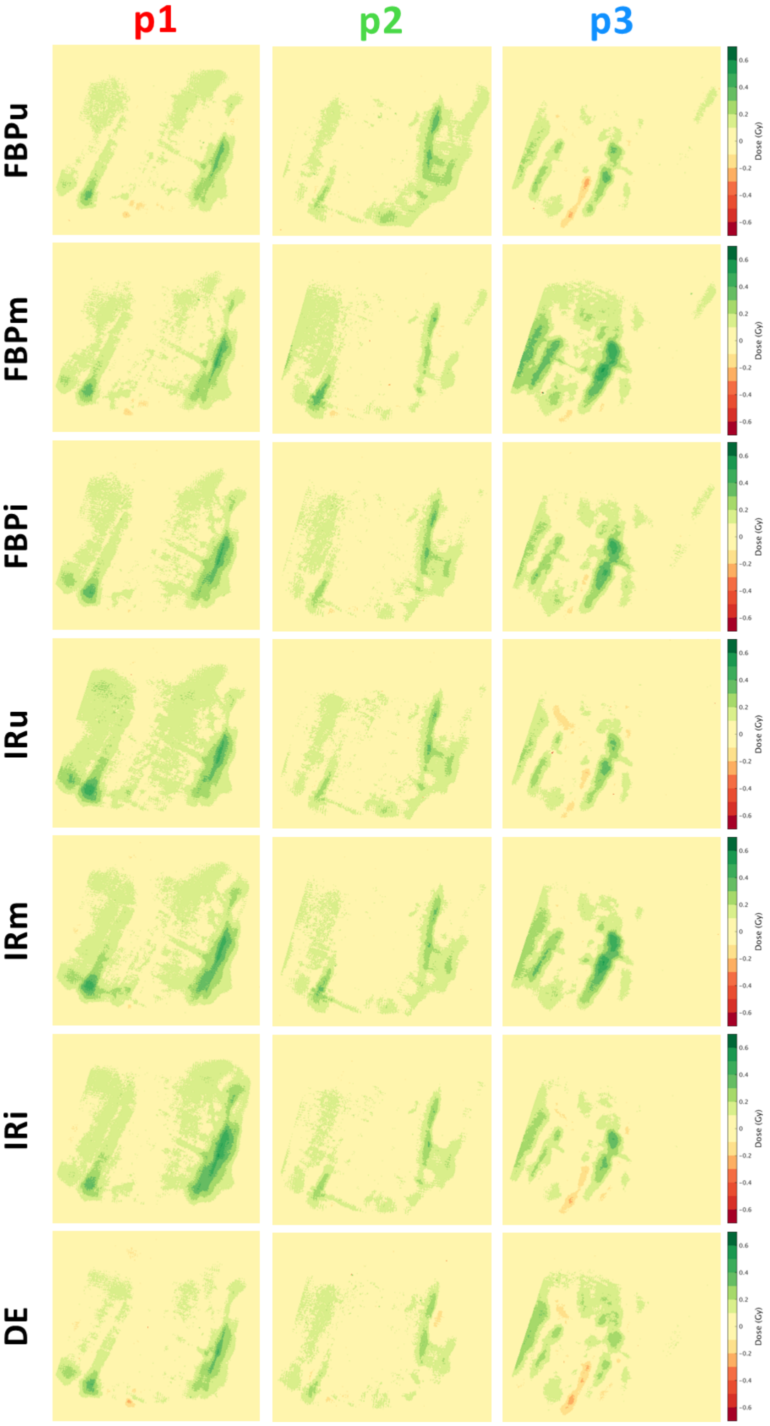

Figure A.10: Dose differences (calculated-measured) obtained in the 4-fields IMPT plan for each approach and each plane.

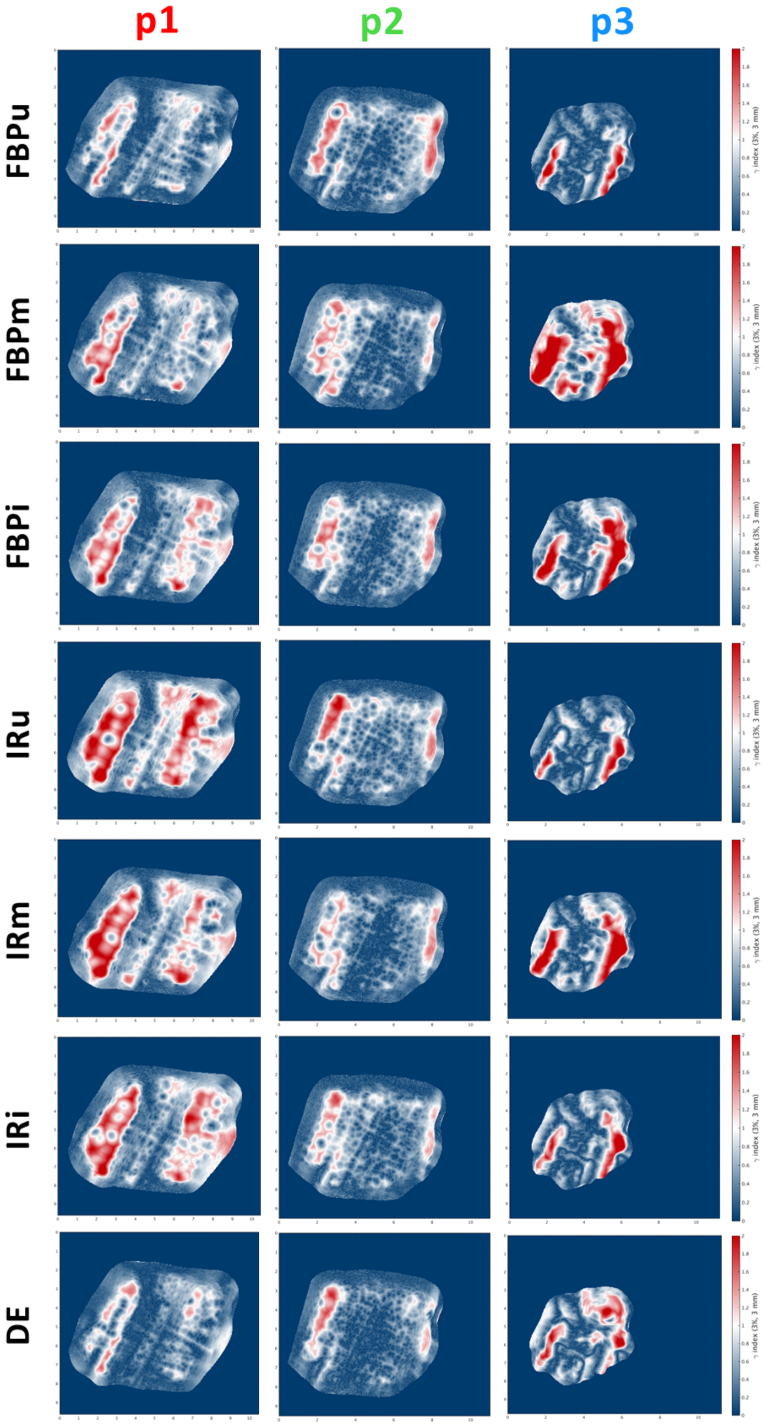

Figure A.11: Gamma maps 3%/3mm on the 50% isodose obtained in the 4-fields IMPT plan for each approach and each plane.

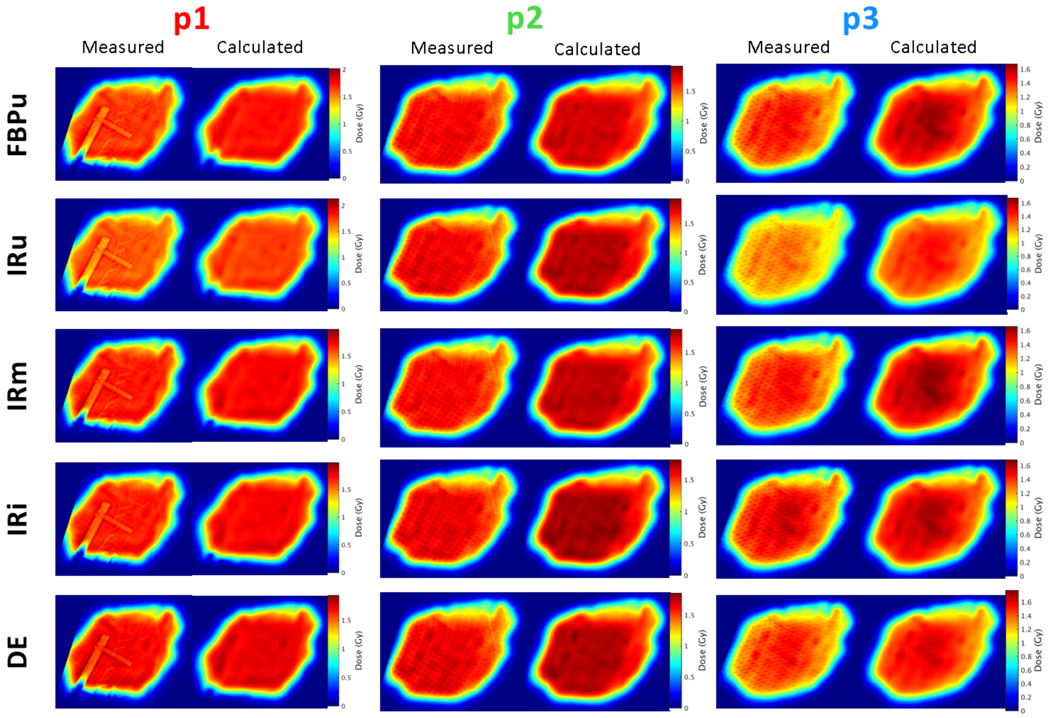

Figure A.12: Dose distributions (measured and calculated) obtained in the 1-field SFUD plan for each approach and each plane.

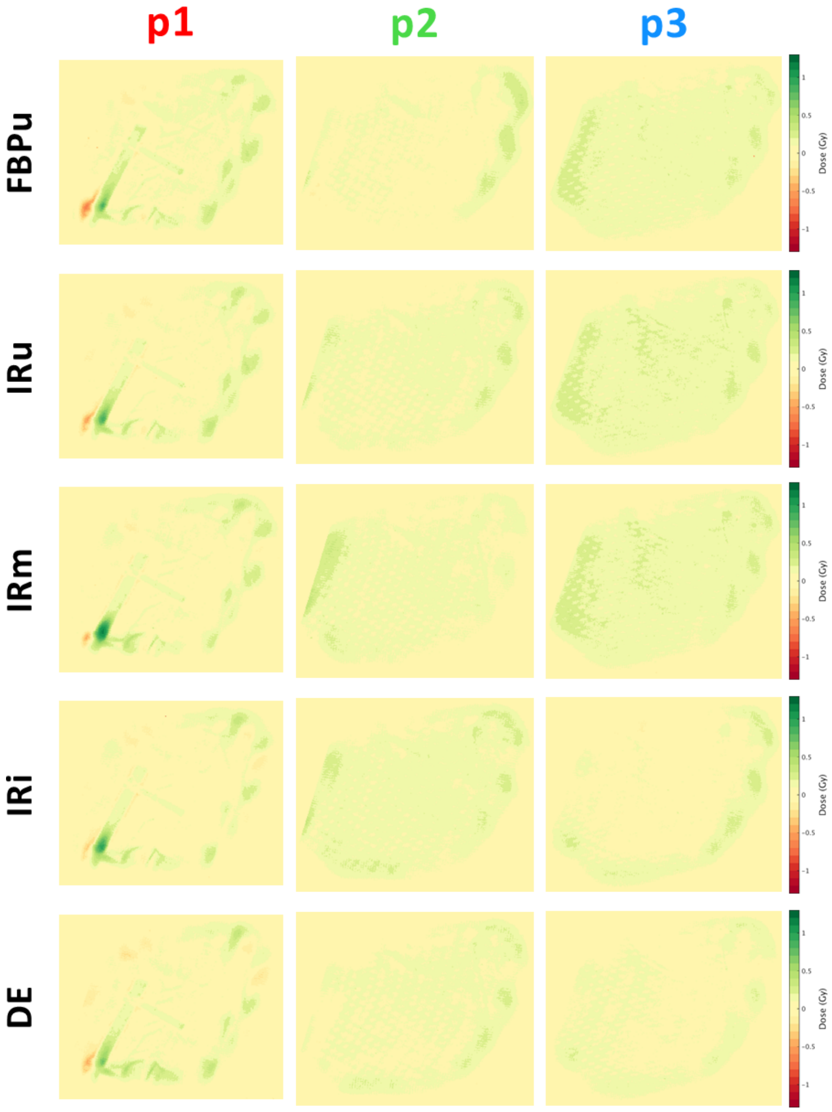

Figure A.13: Dose differences (calculated-measured) obtained in the 1-field SFUD plan for each approach and each plane.

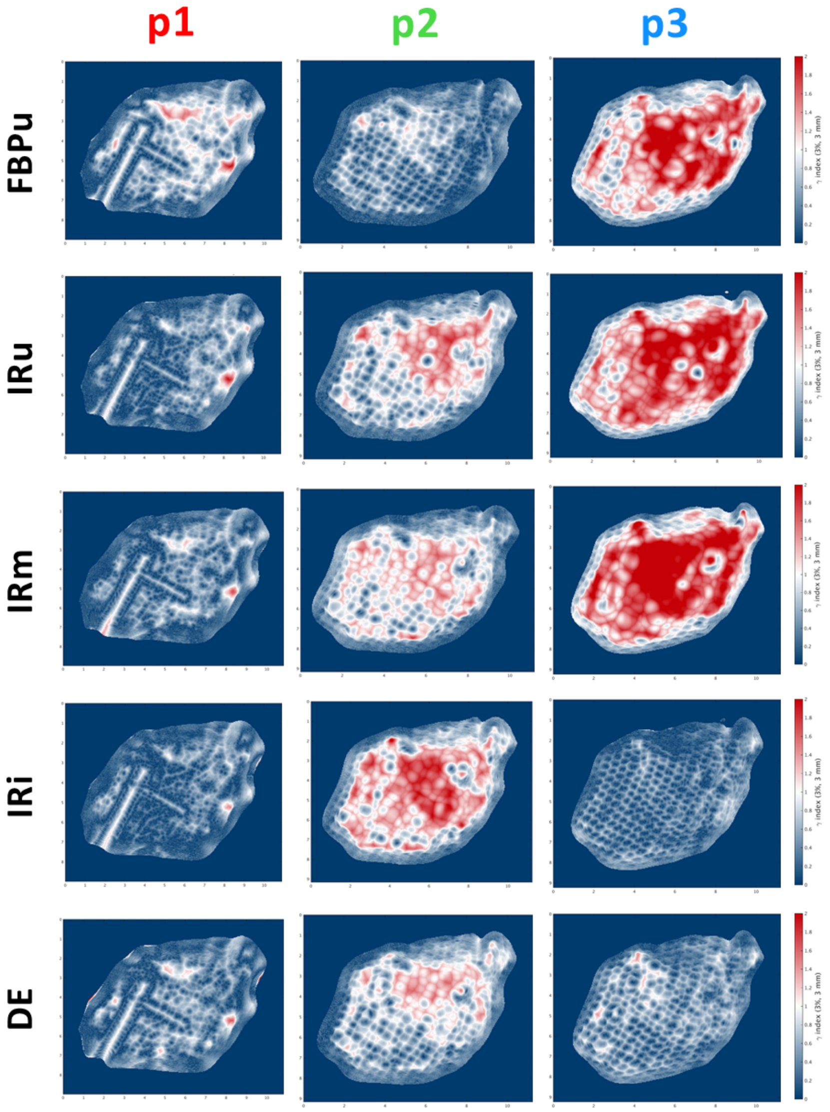

Figure A.14: Gamma maps 3%/3mm on the 50% isodose obtained in the 1-field SFUD plan for each approach and each plane.

Bibliography

[Albertini et al, 2010] Albertini F, Gaignat S, Bosshardt M and Lomax AJ (2009) *"Planning and Optimizing Treatment Plans for Actively Scanned Proton Therapy."* - Biomedical Mathematics Promising Directions in Imaging, Therapy Planning, and Inverse Problems ed Y Censor, M Jiang and G Wang (Madison, WI: Medical Physics Publishing) pp 1–18

[Albertini et al, 2011] Albertini F, Casiraghi M, Lorentini S, Rombi B and Lomax A (2011) *"Experimental verification of IMPT treatment plans in an anthropomorphic phantom in the presence of delivery uncertainties."* - Phys Med Biol; 56:4415–4431, doi:10.1088/0031-9155/56/14/012

[Alvarez and Macovski, 1976] Alvarez RE and Macovski A (1976) *"Energy-selective Reconstructions in X-ray Computerized Tomography."* - Physics in Medicine and Biology; 21(5):733–744, doi:10.1088/0031-9155/21/5/002

[Aran et al, 2014] Aran S, Besheli LD, Karcaaltincaba M, Gupta R, Flores EJ and Abujudeh HH (2014) *"Applications of Dual-Energy CT in Emergency Radiology."* - American Journal of Roentgenology; 202(4):W314-24, doi:10.2214/AJR.13.11682

[Axente et al, 2015] Axente M, Paidi A, Von Eyben R, Zeng C, Bani-Hashemi A, Krauss A and Hristov D (2015) *"Clinical evaluation of the iterative metal artifact reduction algorithm for CT simulation in radiotherapy."* - Med Phys; 42(3):1170-83, doi:10.1118/1.4906245

[Barrett and Keat, 2004] Barrett JF and Keat N (2004) *"Artifacts in CT: Recognition and Avoidance."* - RadioGraphics; 24:1679–1691

[Bazalova et al, 2008] Bazalova M, Carrier JF, Beaulieu L and Verhaegen F (2008) *"Dual-energy CT-based material extraction for tissue segmentation in Monte Carlo dose calculations."* - Phys Med Biol; 53:2439–2456, doi:10.1088/0031-9155/53/9/015

[Bethe, 1930] Bethe H (1930) *"Zur Theorie des Durchgangs schneller Korpuskularstrahlen durch Materie."* - Annalen der Physik; 397(3):325–400, doi:10.1002/andp.19303970303

[Birks, 1964] Birks JB (1964) *"Theory and Practice of Scintillation Counting."* - New York: Pergamon

[Bloch, 1933] Bloch F (1933) *"Bremsvermögen von Atomen mit mehreren Elektronen."* - F. Z. Physik; 81:363, doi:10.1007/BF01344553

[Boas and Fleischmann, 2012] Boas FE and Fleischmann D (2012) *"CT artifacts: Causes and reduction techniques."* - Imaging Med; 4(2):229-240

[Bolsi et al, 2008] Bolsi A, Lomax AJ, Pedroni E, Goitein G and Hug E (2008) *"Experiences at the Paul Scherrer Institute with a remote patient positioning procedure for high-throughput proton radiation therapy."* - Int J Radiat Oncol Biol Phys; 71(5):1581-90, doi:10.1016/j.ijrobp.2008.02.079

[Borca et al, 2013] Borca VC, Pasquino M, Russo G, Grosso P, Cante D, Sciacero P, Girelli G, La Porta MR and Tofani S (2013) *"Dosimetric characterization and use of GAFCHROMIC EBT3 film for IMRT dose verification."* - J Appl Clin Med Phys; 14(2):4111, doi:10.1120/jacmp.v14i2.4111

[Bourque et al, 2014] Bourque AE, Carrier JF and Bouchard H (2014) *"A stoichiometric calibration method for dual energy computed tomography."* - Phys Med Biol; 59:2059–2088, doi:10.1088/0031-9155/59/8/2059

[Brody et al, 1981] Brody WR, Butt G, Hall A and Macovski A (1981) *"A method for selective tissue and bone visualization using dual energy scanned projection radiography."* - Medical Physics; 8(3):353-357, doi:10.1118/1.594957

[Bula et al, 2013] Bula C, Meer D and Pedroni E (2013) *"A system for the delivery of proton therapy by pencil beam scanning of a predeterminable volume within a patient."* - WO Patent, App. PCT/EP2013/056,732

[Bushberg and Boone, 2011] Bushberg JT and Boone JM (2011) *"The essential physics of medical imaging."* - Lippincott Williams & Wilkins

[Chen et al, 1979] Chen GT, Singh RP, Castro JR, Lyman JT and Quivey JM (1979) *"Treatment planning for heavy ion radiotherapy."* - Int J Radiat Oncol Biol Phys; 5(10):1809-19, doi:10.1016/0360-3016(79)90564-9

[Cormode et al, 2010] Cormode DP, Roessl E, Thran A, Skajaa T, Gordon RE, Schlomka JP, Fuster V, Fisher EA, Mulder WJ, Proksa R and Fayad ZA (2010) *"Atherosclerotic plaque composition: analysis with multicolor CT and targeted gold nanoparticles."* - Radiology; 256(3):774-82, doi:10.1148/radiol.10092473

[Dalrymple et al, 1966] Dalrymple GV, Lindsay IR, Hall JD, Mitchell JC, Ghidoni JJ, Kundel HL and Morgan IL (1966) *"The Relative Biological Effectiveness of 138-Mev Protons as Compared to Cobalt-60 Gamma Radiation."* - Radiation Research; 28(2):489-506, doi:10.2307/3572211

[Deasy et al, 1997] Deasy JO, Shepard D and Mackie TR (1997) *"Distal Edge Tracking: A Proposed Delivery Method for Conformal Proton Therapy Using Intensity Modulation."* - Proceedings XIIth ICCR. Madison, WI:Medical Physics Publishing, 406-9

[Dehm and Reinsberger, 2012] Dehm C and Reinsberger H (2012) *"STRATON X-ray Tube - Siemens developed the STRATON X-ray tube for high-performance CT scanning in extreme operating conditions."* - `https://health.siemens.com/ct_applications/somatomsessions/index.php/straton-x-ray-tube/`

[DeLaney and Kooy, 2008] DeLaney TF and Kooy HM (2008) *"Proton and charged particle radiotherapy."* - Lippincott Williams and Wilkins

[DeLaney et al, 2009] DeLaney TF, Liebsch NJ, Pedlow FX, Adams J, Dean S, Yeap BY, McManus P, Rosenberg AE, Nielsen GP, Harmon DC, Spiro IJ, Raskin KA, Suit HD, Yoon SS and Hornicek FJ (2009) *"Phase II study of high-dose photon/proton radiotherapy in the management of spine sarcomas."* - Int J Radiat Oncol Biol Phys; 74(3):732-9, doi:10.1016/j.ijrobp.2008.08.058

[Dietlicher et al, 2014] Dietlicher I, Casiraghi M, Ares C, Bolsi A, Weber DC, Lomax AJ and Albertini F (2014) *"The effect of surgical titanium rods on proton therapy delivered for cervical bone tumors: experimental validation using an anthropomorphic phantom."* - Phys Med Biol; 59(23):7181-94, doi:10.1088/0031-9155/59/23/7181

[Elliott and Slakey, 2014] Elliott MJ and Slakey JB (2014) *"CT Provides Precise Size Assessment of Implanted Titanium Alloy Pedicle Screws."* - Clin Orthop Relat Res; 472(5):1605–1609, doi:10.1007/s11999-014-3494-0

[Farace, 2014] Farace P (2014) *"Experimental verification of ion stopping power prediction from dual energy CT data in tissue surrogates."* - Phys Med Biol; 59(1):83-96, doi:10.1088/0031-9155/59/1/83

[Fattori et al, 2015] Fattori G, Riboldi M, Pella A, Peroni M, Cerveri P, Desplanques M, Fontana G, Tagaste B, Valvo F, Orecchia R and Baroni G (2015) *"Image guided particle therapy in CNAO room 2: Implementation and clinical validation."* - Physica Medica, European Journal of Medical Physics; 31(2):9-15, doi:10.1016/j.ejmp.2014.10.075

[Fiorini et al, 2014] Fiorini F, Kirby D, Thompson J, Green S, Parker DJ, Jones B and Hill MA (2014) *"Under-response correction for EBT3 films in the presence of proton spread out Bragg peaks."* - Phys Med; 30(4):454-61, doi:10.1016/j.ejmp.2013.12.006

[Goiten, 2008] Goiten M (2008) *"Radiation Oncology: A Physicist's Eye View."* - Springer

[Goodhead, 1990] Goodhead DT *"Radiation effects in living cells."* - Canadian Journal of Physics; 68(9):872-886, doi:10.1139/p90-125

[Goodsitt et al, 2011] Goodsitt MM, Christodoulou EG and Larson SC (2011) *"Accuracies of the synthesized monochromatic CT numbers and effective atomic numbers obtained with a rapid kVp switching dual energy CT scanner."* - Med Phys; 38(4):2222, doi:10.1118/1.3567509

[Grant and Raupach, 2012] Grant K and Raupach R (2012) *"SAFIRE: Sinogram Affirmed Iterative Reconstruction."* - `http://www.usa.siemens.com/healthcare`

[Hansen et al, 2015] Hansen DC, Seco J, Sorensen TS, Petersen JB, Wildberger JE, Verhaegen F and Landry G (2015) *"A simulation study on proton computed tomography (CT) stopping power accuracy using dual energy CT scans as benchmark."* - Acta Oncol; 54(9):1638-42, doi:10.3109/0284186X.2015.1061212

[Hoggarth et al, 2013] Hoggarth MA, Luce J, Syeda F, Bray TS, Block A, Nagda S and Roeske JC (2013) *"Dual energy imaging using a clinical on-board imaging system."* - Phys Med Biol; 58(12):4331-40, doi:10.1088/0031-9155/58/12/4331

[Hounsfield, 1973] Hounsfield GN (1973) *"Computerized transverse axial scanning (tomography): Part 1. Description of system."* - The British Journal of Radiology, 46(552):1016–1022, doi:10.1259/0007-1285-46-552-1016

[Hsieh, 2009] Hsieh J (2009) *"Computed Tomography, Second Edition: Principles, Design, Artifacts, and Recent Advances."* - doi:10.1117/3.817303

[Hudobivnik et al, 2016] Hudobivnik N, Schwarz F, Johnson T, Agolli L, Dedes G, Tessonnier T, Verhaegen F, Thieke C, Belka C, Sommers W, Parodi K and Landry G (2016) *"Comparison of proton therapy treatment planning for head tumors with a pencil beam algorithm on dual and single energy CT images."* - Med Phys; 43:495, doi:10.1118/1.4939106

[Hünemohr et al, 2013] Hünemohr N, Krauss B, Dinkel J, Gillmann C, Ackermann B, Jakel O and Greilich S (2013) *"Ion range estimation by using dual energy computed tomography."* - Z Med Phys; 23(4):300-13, doi:10.1016/j.zemedi.2013.03.001

[Hünemohr et al, 2014a] Hünemohr N, Krauss B, Tremmel C, Ackermann B, Jäkel O and Greilich S (2014) *"Experimental verification of ion stopping power prediction from dual energy CT data in tissue surrogates."* - Phys Med Biol; 59(1):83-96, doi:10.1088/0031-9155/59/1/83

[Hünemohr et al, 2014b] Hünemohr N, Paganetti H, Greilich S, Jäkel O, Seco J (2014) *"Tissue decomposition from dual energy CT data for MC based dose calculation in particle therapy."* - Med Phys.; 41(6):061714. doi:10.1118/1.4875976.

[Huo et al, 2014] Huo J, Zhu X, Dong Y, Yuan Z, Wang P, Wang X, Wang G, Hu XH and Feng Y (2014) *"Feasibility Study of Dual Energy Radiographic Imaging for Target Localization in Radiotherapy for Lung Tumors."* - PLoS One; 9(9):e108823, doi:10.1371/journal.pone.0108823

[ICRU, 1979] ICRU (1979) *"Quantitative Concepts and Dosimetry in Radiobiology (Report 30)."* - Journal of the ICRU

[ICRU, 1993] ICRU (1993) *"Stopping Powers and Ranges for Protons and Alpha Particles (Report 49)."* - Journal of the ICRU

[ICRU, 1993] ICRU (1993) *"Prescribing, Recording and Reporting Photon Beam Therapy (Report 50)."* - Journal of the ICRU

[ICRU, 1999] ICRU (1999) *"Prescribing, Recording and Reporting Photon Beam Therapy (Report 62)."* - Journal of the ICRU

[ICRU, 2004] ICRU (2004) *"Prescribing, Recording, and Reporting Electron Beam Therapy (Report 71)."* - Journal of the ICRU

[ICRU, 2005] ICRU (2005) *"Stopping of ions heavier than helium (Report 73)."* - Journal of the ICRU

[ICRU, 2007] ICRU (2007) *"Prescribing, Recording, and Reporting Proton-Beam Therapy (ICRU Report 78)."* - Journal of the ICRU

[Janni, 1982] Janni JF (1982) *"Proton Range-Energy Tables, 1 keV-10 GeV, Energy Loss, Range, Path Length, Time-of-Flight, Straggling, Multiple Scattering, and Nuclear Interaction Probability. Part I. For 63 Compounds."* - Atomic Data and Nuclear Data Tables; 27:147, doi:10.1016/0092-640X(82)90004-3

[Johns, 1983] Johns HE (1983) *"The Physics of Radiology."* - Charles River Media

[Johnson et al, 2007] Johnson TR, Krauss B, Sedlmair M, Grasruck M, Bruder H, Morhard D, Fink C, Weckbach S, Lenhard M, Schmidt B, Flohr T, Reiser MF and Becker CR (2007) *"Material differentiation by dual energy CT: initial experience."* - Eur Radiol; 17(6):1510-7, doi:10.1007/s00330-006-0517-6

[Johnson, 2012] Johnson TR (2012) *"Dual-Energy CT: General Principles."* - AJR Am J Roentgenol; 199(5 Suppl):S3-8, doi:10.2214/AJR.12.9116

[Johnson et al, 2011] Johnson T, Fink C, Schönberg SO, Reiser MF (2011) *"Dual Energy CT in Clinical Practice."* - Springer

[Kachelrieß and Krauss, 2015] Kachelrieß M and Krauss A (2015) *"Iterative Metal Artifact Reduction (iMAR): Technical Principles and Clinical Results in Radiation Therapy."* - `http://www.usa.siemens.com/healthcare`

[Kanai et al, 1980] Kanai T, Kawachi K, Kumamoto Y, Ogawa H, Yamada T, Matsuzawa H and Inada T (1980) *"Spot scanning system for proton radiotherapy."* - Med Phys; 7(4):365-9, doi:10.1118/1.594693

[Kappler et al, 2011] Kappler S, Hölzer S, Kraft E, Stierstorfer K and Flohr T (2011) *"Quantum-counting CT in the regime of countrate paralysis: introduction of the pile-up trigger method."* - Proc SPIE; 7961:79,610T

[Kittel, 1967] Kittel C (1967) *"Elementary statistical physics."* - Wiley

[Koehler et al, 1975] Koehler AM, Schneider RJ and Sisterson JM (1975) *"Range modulators for protons and heavy ions."* - Nuclear Instruments and Methods; 131(3):437-440, doi:10.1016/0029-554X(75)90430-9

[Koehler et al, 1977] Koehler AM, Schneider RJ and Sisterson JM (1977) *"Flattening of proton dose distributions for large-field radiotherapy."* - Med Phys; 4(4):297-301, doi:10.1118/1.594317

[Kohl, 2005] Kohl G (2005) *"The Evolution and State-of-the-Art Principles of Multislice Computed Tomography."* - Proceeding of the American Thoracic Society; 2(6):470-476, doi:10.1513/pats.200508-086DS

[Kortmann et al, 1994] Kortmann RD, Hess CF, Jany R, Meisner C and Bamberg M (1994) *"Reproducibility of field alignment in difficult patient positioning."* - Int J Radiat Oncol Biol Phys; 29(4):869-72, doi:10.1016/0360-3016(94)90578-9

[Landry et al, 2011] Landry G, Reniers B, Granton PV, van Rooijen B, Beaulieu L, Wildberger JE and Verhaegen F (2011) *"Extracting atomic numbers and electron densities from a dual source dual energy CT scanner: Experiments and a simulation model."* - Radiother Oncol; 100(3):375-9, doi:10.1016/j.radonc.2011.08.029

[Landry et al, 2015] Landry G, Gaudreault M, van Elmpt W, Wildberger JE and Verhaegen F (2015) *"Improved dose calculation accuracy for low energy brachytherapy by optimizing dual energy CT imaging protocols for noise reduction using sinogram affirmed iterative reconstruction."* - Z Med Phys; 26(1):75-87, doi:10.1016/j.zemedi.2015.09.001

[Landry et al, 2013] Landry G, Seco J, Gaudreault M and Verhaegen F *"Deriving effective atomic numbers from DECT based on a parameterization of the ratio of high and low linear attenuation coefficients."* - Phys Med Biol; 58:6851–6856, doi:10.1088/0031-9155/58/19/6851

[Lell et al, 2015] Lell MM, Wildberger JE, Alkadhi H, Damilakis J and Kachelriess M (2015) *"Evolution in Computed Tomography: The Battle for Speed and Dose."* - Invest Radiol; 50(9):629-44, doi:10.1097/RLI.0000000000000172

[Levin et al, 2005] Levin WP, Kooy H, Loeffler JS and DeLaney TF (2005) *"Proton beam therapy."* - Br J Cancer; 93(8):849-54, doi:10.1038/sj.bjc.6602754

[Li et al, 2013] Li H, Sahoo N, Poenisch F, Suzuki, K Li Y, Li X, Zhang X, Lee A, Gillin M and Zhu X (2013) *"Use of treatment log files in spot scanning proton therapy as part of patient-specific quality assurance."* - Med Phys; 40(2):021703, doi:10.1118/1.4773312

[Lomax, 1999] Lomax AJ (1999) *"Intensity modulation methods for proton radiotherapy."* - Physics in Medicine and Biology; 44(1):185–205

[Lomax et al, 2001] Lomax AJ, Boehringer T, Coray A, Egger E, Goitein G, Grossmann M, Juelke P, LinS, Pedroni E, Rohrer B, Roser W, Rossi B, Siegenthaler B, Stadelmann O, Stauble H, Vetter C and Wisser L (2001) *"Intensity modulated proton therapy: A clinical example."* - Medical Physics; 28(3):317-24, doi:10.1118/1.1350587

[Lomax et al, 2004] Lomax AJ, Böhringer T, Bolsi A, Coray D, Emert F, Goitein G, Jermann M, Lin S, Pedroni E, Rutz H, Stadelmann O, Timmermann B, Verwey J and Weber DC (2004) *"Treatment planning and verification of proton therapy using spot scanning: initial experiences."* - Medical Physics; 31(11):3150-7, doi:10.1118/1.1779371

[Lomax, 2008] Lomax AJ (2008) *"Intensity modulated proton therapy and its sensitivity to treatment uncertainties 2. The potential effects of inter-fraction and interfiled motion."* - Phys Med Biol; 53(4):1043-56, doi:10.1088/0031-9155/53/4/015

[Low et al, 1998] Low DA, Harms WB Mutic S and Purdy JA (1998) *"A technique for the quantitative evaluation of dose distributions."* - Med Phys; 25:656-61, doi:10.1118/1.598248

[McCollough et al, 2015] McCollough CH, Leng S, Yu L and Fletcher JG (2015) *"Dual- and Multi-Energy CT: Principles, Technical Approaches, and Clinical Applications."* - Radiology; 276(3):637-53, doi:10.1148/radiol.2015142631

[Meier et al, 2015] Meier G, Besson R, Nanz A, Safai S and Lomax AJ (2015) *“Independent dose calculations for commissioning, quality assurance and dose reconstruction of PBS proton therapy.”* - Phys Med Biol; 60(7):2819-36, doi:10.1088/0031-9155/60/7/2819

[Morsbach et al, 2013a] Morsbach F, Bickelhaupt S, Wanner GA, Krauss A, Schmidt B and Alkadhi H (2013) *“Reduction of metal artifacts from hip prostheses on CT images of the pelvis: value of iterative reconstructions.”* - Radiology; 268(1):237-44, doi:10.1148/radiol.13122089

[Morsbach et al, 2013b] Morsbach F, Wurnig M, Kunz DM, Krauss A, Schmidt B, Kollias SS and Alkadhi H (2013) *“Metal artefact reduction from dental hardware in carotid CT angiography using iterative reconstructions.”* - Eur Radiol; 23(10):2687-94, doi:10.1007/s00330-013-2885-z

[Mustafa and Jackson, 1983] Mustafa AA and Jackson DF (1983) *“The relation between x-ray CT numbers and charged particle stopping powers and its significance for radiotherapy treatment planning.”* - Phys Med Biol, 28(2):169-176, doi:10.1088/0031-9155/28/2/006

[Paganetti, 2011] Paganetti H (2011) *“Proton Therapy Physics.”* - CRC Press

[Pedroni et al, 1995] Pedroni E, Bacher R, Blattmann H, Böhringer T, Coray A, Lomax AJ, Lin S, Munkel G, Scheib S, Schneider U and Tourovsky A (1995) *“The 200-MeV proton therapy project at the Paul Scherrer Institute: Conceptual design and practical realization.”* - Med Phys; 22:37, doi:10.1118/1.597522

[Pedroni et al, 2004] Pedroni E, Bearpark R, Böhringer T, Coray A, Duppich J, Forss S, George D, Grossmann M, Goitein G, Hilbes C, Jermann M, Lin S, Lomax AJ, Negrazus M, Schippers M and Kotrle G (2004) *“The PSI Gantry 2: a second generation proton scanning gantry.”* - Zeitschrift für Medizinische Physik, doi:10.1078/0939-3889-00194

[Pedroni et al, 2011] Pedroni E, Meer D, Bula C, Safai S and Zenklusen S (2011) *“Pencil beam characteristics of the next-generation proton scanning gantry of PSI: design issues and initial commissioning results.”* - Eur Phys J Plus; 126:66, doi:10.1140/epjp/i2011-11066-0

[Perrin et al, 2015] Perrin RL, Peroni M, Bernatowicz K, Schaetti A, Knopf AK, Zakova M, Oxley D, Mayor A, Safai S, Parkel TC, Weber DC and Lomax T (2015) *“OC-0484: Rescanning measurements in a 4D anthropomorphic phantom for evaluation of motion-mitigated, PBS proton therapy.”* - Radiotherapy and Oncology; 115(1):S238-S239, doi:10.1016/S0167-8140(15)40480-3

[Petersilka et al, 2008] Petersilka M, Brudera H, Kraussa B, Stierstorfera K and Flohra TG (2008) *“Technical principles of dual source CT.”* - Eur J Radiol; 68(3):362-8, doi:10.1016/j.ejrad.2008.08.013

[Reinhardt et al, 2012] Reinhardt S, Hillbrand M, Wilkens JJ and Assmann W (2012) *"Comparison of Gafchromic EBT2 and EBT3 films for clinical photon and proton beams."* - Medical Physics; 39:5257, doi:10.1118/1.4737890

[Roentgen, 1896] Roentgen WC (1896) *"On a new kind of rays."* - Science; 3(59):227-31, doi:10.1126/science.3.59.227

[Rutherford et al, 1976] Rutherford RA, Pullan BR and Isherwood I (1976) *"Measurement of effective atomic number and electron density using an EMI scanner."* - Neuroradiology; 11(1):15-21, doi:10.1007/BF00327253

[Rutz et al, 2007] Rutz HP, Weber DC, Sugahara S, Timmermann B, Lomax AJ, Bolsi A, Pedroni E, Coray A, Jermann M and Goitein G (2007) *"Extracranial chordoma: outcome in patients treated with function-preserving surgery followed by spot-scanning proton beam irradiation."* - Int J Radiat Oncol Biol Phys; 67(2):512-20, doi:10.1016/j.ijrobp.2006.08.052

[Saito, 2012] Saito M (2012) *"Potential of dual-energy subtraction for converting CT numbers to electron density based on a single linear relationship."* - Med Phys; 39(4):2021-30, doi:10.1118/1.3694111

[Sakurai and Tuan, 1993] Sakurai JJ and Tuan SF (1993) *"Modern quantum mechanics, volume 2."* - Addison-Wesley Reading, Massachusetts

[Saur and Frengen, 2008] Saur S and Frengen J (2008) *"GafChromic EBT film dosimetry with flatbed CCD scanner: A novel background correction method and full dose uncertainty analysis."* - Medical Physics; 35:3094, doi:10.1118/1.2938522

[Scandurra et al, 2016] Scandurra D, Albertini F, van der Meer R, Meier G, Weber DC, Bolsi A and Lomax AJ (2016) *"Assessing the quality of proton PBS treatment delivery using machine log files: comprehensive analysis of clinical treatments delivered at PSI Gantry 2."* - Phys Med Biol; 61(3):1171-81, doi:10.1088/0031-9155/61/3/1171

[Schätti et al, 2014] Schätti A, Meer D and Lomax AJ (2014) *"First experimental results of motion mitigation by continuous line scanning of protons."* - Phys Med Biol; 59(19):5707-23, doi:10.1088/0031-9155/59/19/5707

[Schneider et al, 1996] Schneider U, Pedroni E and Lomax AJ (1996) *"The calibration of CT Hounsfield units for radiotherapy treatment planning."* - Physics in Medicine and Biology; 41(1):111, doi:10.1088/0031-9155/41/1/009

[Schneider et al, 2000] Schneider W, Bortfeld T and Schlegel W (2000) *"Correlation between CT numbers and tissue parameters needed for Monte Carlo simulations of clinical dose distributions."* - Physics in Medicine and Biology; 45:459–478, doi:10.1088/0031-9155/45/2/314

[Schulte, 2007] Schulte RW (2007) *"Strategies for Image-guided Proton Therapy of Cancer."* - European Oncological Disease; 1(2):116-8, doi:10.17925/EOH.2007.0.2.116

[Simons et al, 2014] Simons D, Kachelrieß M and Schlemmer HP (2014) *"Recent developments of dual-energy CT in oncology."* - European Society of Radiology; 24:930–939, doi:10.1007/s00330-013-3087-4

[Staab et al, 2011] Staab A, Rutz HP, Ares C, Timmermann B, Schneider R, Bolsi A, Albertini F, Lomax A, Goitein G and Hug E (2011) *"Spot-scanning-based proton therapy for extracranial chordoma."* - Int J Radiat Oncol Biol Phys; 81(4):e489-96, doi:10.1016/j.ijrobp.2011.02.018

[Tepper et al, 1977] Tepper J, Verhey L, Goitein M and Suit HD (1977) *"In vivo determinations of RBE in a high energy modulated proton beam using normal tissue reactions and fractionated dose schedules."* - Int J Radiat Oncol Biol Phys; 2(11-12):1115-22, doi:10.1016/0360-3016(77)90118-3

[Torrisi, 2000] Torrisi L (2000) *"Plastic scintillator investigations for relative dosimetry in proton-therapy."* - Nuclear Instruments and Methods in Physics Research, Section B, Beam Interactions with Materials and Atoms; 170(3-4):523-530, doi:10.1016/S0168-583X(00)00237-8

[Urano et al, 1980] Urano M, Goitein M, Verhey L, Mendiondo O, Suit HD and Koehler A (1980) *"Relative biological effectiveness of a high energy modulated proton beam using a spontaneous murine tumor in vivo."* - Int J Radiat Oncol Biol Phys; 6(9):1187-93, doi:10.1016/0360-3016(80)90172-8

[van Elmpt et al, 2016] van Elmpt W, Landry G, Das M and Verhaegen F (2016) *"Dual energy CT in radiotherapy: Current applications and future outlook."* - Radiother Oncol; 119(1):137-44, doi:10.1016/j.radonc.2016.02.026

[Verburg and Seco, 2013] Verburg JM and Seco J (2013) *"Dosimetric accuracy of proton therapy for chordoma patients with titanium implants."* - Med Phys; 40(7):071727, doi:10.1118/1.4810942

[Williams and Metcalfe, 2011] Williams M and Metcalfe P (2011) *"Radiochromic film dosimetry and its applications in radiotherapy."* - 4th SSD Summer School: Concepts and Trends in Medical Radiation Dosimetry (pp. 75-99). Wollongong: AIP

[Wilson, 1946] Wilson RR (1946) *"Radiological use of fast protons."* - Radiology; 47(5):487-91, doi:10.1148/47.5.487

[Wilting, 1999] Wilting JE (1999) *"Technical aspects of spiral CT."* - Medica Mundi, 43(1)

[Yang et al, 2010] Yang M, Virshup G, Clayton J, Zhu XR, Mohan R and Dong L (2010) *"Theoretical variance analysis of single- and dual-energy computed tomography methods for calculating proton stopping power ratios of biological tissues."* - Phys Med Biol; 55(5):1343-62, doi:10.1088/0031-9155/55/5/006

[Yang et al, 2012] Yang M, Zhu XR, Park PC, Titt U, Mohan R, Virshup G, Clayton GE and Dong L (2012) *"Comprehensive analysis of proton range uncertainties related to patient stopping-power-ratio estimation using the stoichiometric calibration."* - Phys Med Biol; 57(13):4095-115, doi:10.1088/0031-9155/57/13/4095

[Yang et al, 2013] Yang WJ, Yan FH, Liu B, Pang LF, Hou L, Zhang H, Pan ZL and Chen KM (2013) *"Sinogram-affirmed iterative (SAFIRE) reconstruction improve imaging quality on low-dose lung CT screening compared with traditional filtered back projection (FBP) reconstruction?."* - J Comput Assist Tomogr; 37(2):301-5, doi:10.1097/RCT.0b013e31827b8c66

[Yi, 2013] Yi BY (2013) *"Practical Considerations in Preparing an Institutional Procedure of Image Guided Radiation Therapy."* - Prog Med Phys; 24(4):205-212, doi:10.14316/pmp.2013.24.4.205

[Zargar et al, 2015] Zargar S, Phad V, Poola PK, Kohn R (2015) *"Role of filtering techniques in Computed Tomography (CT) image reconstruction."* - IJRET: International Journal of Research in Engineering and Technology; 4(12):2319-1163, doi:10.15623/ijret.2015.0424012

[Ziegler et al, 2008] Ziegler J, Biersack J and Ziegler M (2008) *"SRIM, the stopping and range of ions in matter."* - Nuclear Instruments and Methods in Physics Research Section B: Beam Interactions with Materials and Atoms, 268(11-12):1818-1823, doi:10.1016/j.nimb.2010.02.091

Acknowledgments

My first thought is for the entire CPT group of PSI. Thanks for taking me in and making me feel part of this great “family”. In particular, I would like to thank Dr. Marta Peroni and Dr. Alessandra Bolsi for being excellent supervisors and teaching me everything that I know about proton therapy. Thanks to your constant guidance and sound advices. This project would not be nearly as good without your help. I would like to thank all the friends from WBBA/WMSA who I spent all the lunches and breaks with, like Niels, Grischa, Miriam, Jonas, Carla, Ye, Fabian, Kinga, Jenny, Franciska and Martina. Thanks for always trying to convince me learning German and make me enjoy the Swiss weather (without success). Thanks to the first roommate that I have ever had, Franci, for welcoming me into your home and for treating me as friend from the very first moment that we met. Thanks to my roommates of Zurich, Eli, Vane, Stav and Marco, for the home’s atmosphere, the long discussions and for introducing me to the traditional Swiss food: avocado, date nuts and melon. To my lovely Greek friend Nada, thanks for your intense friendship, for your amazing spanakopita and, more than anything, for having made this experience so memorable.

I am particularly grateful to Prof. Maria Pia Morigi for the possibility to pursue this project and the helpful feedback received in the last months. Moreover, I would like to thank several people, especially Iaco, Cla, Pavo, Matte, Lisa and Ceci, whose friendships have helped me to overcome and smooth any kind of difficulty.

A very special thank you is for my parents and my brother, for encouraging me in all of my pursuits and inspiring me to follow my dreams. Thanks you for your support and wanting the best for me, always. Finally, a special though is for Luca. You have always been there, motivating me every day with your contagious optimism, never making me feel alone, no matter the miles. And above all, thank you for having completed together this first accomplishment in our life.